DIELECTRIC CHARGING IN CAPACITIVE RF MEMS SWITCHES WITH SILICON NITRIDE AND SILICON DIOXIDE

A Dissertation
Presented to
The Academic Faculty

by

Negar Tavassolian

In Partial Fulfillment
of the Requirements for the Degree
Doctor of Philosophy in the
School of Electrical and Computer Engineering

Georgia Institute of Technology

May 2011

DIELECTRIC CHARGING IN CAPACITIVE RF MEMS SWITCHES WITH SILICON NITRIDE AND SILICON DIOXIDE

Approved by:

Dr. John Papapolymerou, Advisor
Professor, School of Electrical and Computer Engineering
Georgia Institute of Technology

Dr. George Papaioannou
Professor, School of Physics
University of Athens (Greece)

Dr. Farrokh Ayazi
Professor, School of Electrical and Computer Engineering
Georgia Institute of Technology

Dr. John D. Cressler
Professor, School of Electrical and Computer Engineering
Georgia Institute of Technology

Dr. David C. Keezer
Professor, School of Electrical and Computer Engineering
Georgia Institute of Technology

Date Approved: December 03, 2011

“Let the beauty of what you love be what you do.”

Rumi (1207 - 1273 AD)
Persian poet and Sufi mystic

To my beloved mother,

Dr. Shirin Ebadi.

And

To my soul mate,

Dr. Behnood Gholami.

ACKNOWLEDGEMENTS

I owe my deepest gratitude and respect to my advisor, Professor John Papapolymerou, for his continuous support and encouragement of this work. Not only is he a knowledgeable and intelligent guide and teacher, but also a responsible and considerate human being. I have wondered more than once at his insight and professionalism. I especially thank him for his understanding, patience, and guidance during the ups and downs of my PhD studies. I will always be grateful for what I learned from him during the past years.

It has been a great honor and privilege for me to know and work with Professor George Papaioannou. He is an extremely knowledgeable professor who appreciates science for the sake of science, and makes every effort to help his students see the beauty in learning and education. His modest and friendly behavior raises every admiration and respect. He has generously shared with us his expertise and knowledge in physics, and I am indebted to him for giving me the opportunity to talk to him regularly and for reviewing my work under his intense time constraints. This work would by no means be possible without his interesting ideas, insights, and suggestions.

I am thankful to Professor Farrokh Ayazi, Professor John D. Cressler, and Professor David C. Keezer for taking time to serve on my dissertation committee, and for their useful comments and suggestions to improve this dissertation. I especially thank Professor Farrokh Ayazi for his insightful ideas, and for setting an example of hard work and constant effort to achieve perfection.

I would like to extend my most sincere thanks to my colleagues at MiRCTech research group for their collaboration and friendship. My special thanks go to the senior members of the group, for training me on the cleanroom and lab equipment: Dr. Benjamin Lacroix, Dr. Swapan Bhattacharya, Arnaud Amadjikpé, David Chung, Dr. Yuan Li, Dr. Bo Pan, Chad Patterson, and Richard Daigler.

I wish to thank the cleanroom staff at Georgia Tech for providing an efficient and pleasant environment to work in.

I am grateful to Professor Wassim M. Haddad, for kindly giving me his attention, time, and advice. I also thank him and his wife Lydia Haddad, for patiently listening to me and caring about my academic future.

I would like to thank my wonderful friends in Atlanta and elsewhere for their encouragements, and for making my graduate studies a memorable experience on the social front. Especially, I thank Dr. Laleh Najafizadeh, Marmar Mehrabadi, and Roozbeh Tabrizian for their genuine friendship and for many enjoyable conversations.

I am boundlessly grateful to my entire family for their love and never-ending support. I especially thank my father, Javad Tavassolian, my mother-in-law, Mahboobeh Najaf Khani, and my father-in-law, Abolfazl Gholami, for their attention and kindness, and my sweet sister, Nargess, for her admirably cheerful and positive character.

As for my mother, Dr. Shirin Ebadi, nothing I say or write can possibly express my heart-felt admiration, gratitude and love. She is the embodiment of integrity, wisdom, forgiveness and strength. I feel honored and fortunate to have been in her life

and to have observed the beauty of her thoughts, words, and actions. I also thank her for investing her time and energy on me, and for never stopping to believe in me.

Last but by no means least, my gratitude and love go to my husband and best friend, Dr. Behnood Gholami. He has a rare combination of intelligence, insight, dependability, and modesty. With his curious, clever, and selfless approach, he always finds ways to understand, help, and improve the lives of people who come to his life and I have been no exception to this. I thank him for helping me become a better person, both personally and professionally.

TABLE OF CONTENTS

LIST OF TABLES

LIST OF FIGURES

NOMENCLATURE

List of Symbols

Aº	Angestrom (10^{-10} m)
C	Celsius
ε_r	Permittivity
eV	Electron volt
f	Femto
G	Giga
H	Henry
Hz	Hertz
k	Kilo
K	Kelvin
m	Meter
M	Mega
μ	Micron

n	Nano
Ω	Ohm (Greek: Omega)
p	Pico
Pa	Pascal
ρ	Resistivity (Greek: Rho)
S	Siemens
sec	second
V	Volt
W	Watt

List of Abbreviations

A	Area
Al	Aluminum
Al_2O_3	Aluminum dioxide
AlN	Aluminum nitride
Au	Gold

b	Damping coefficient
C	Capacitance
Cr	Chromium
CPW	Coplanar waveguide
C-V	Capacitance-voltage
d (x,y)	Air gap distribution
dB	Decibel
dBm	Decibels referenced to one milliwatt
DC	Direct current
Δ	Deflection (Greek: delta)
h	Planck's constant (Greek: eta)
E	Electric field
E_A	Activation energy
F	Force
f	Frequency

f_0	Resonance frequency
FET	Field-effect transistor
g	Gap
g_o	Initial gap
GaAs	Gallium-arsenide
H	Thickness (also, t)
I	Current
IL	Insertion loss
j	Current density
k	Boltzmann's constant
κ	Spring constant (Greek: kappa)
k_{eff}	Effective spring constant
k_m	Meandered spring constant
$k_{n\text{-}m}$	Non-meandered spring constant
L	Length, Inductance

MEMS	Microelectromechanical systems
MIM	Metal-isulator-metal
N	Nitrogen
v	Poisson's ratio (Greek: nu)
P	Polarization
PECVD	Plasma-enhanced chemical vapor deposition
PF	Poole-Frenkel
Q	Total surface charge
RF	Radio frequency
RIE	Reactive ion etching
$\psi (x, y, z)$	Volume charge density
Si	Silicon
SiH_4	Silane
Si_3N_4	Silicon nitride
SiO_2	Silicon dioxide

τ	Time constant
t	Time
T	Temperature
tan δ	Loss tangent
TAT	Trap-Assisted Tunneling
Ti	Titanium
TSDC	Thermally stimulated depolarization current
V	Voltage
V_m	Bias voltage for minimum capacitance
V_{PI}	Pull-out voltage
V_{PO}	Pull-in voltage
w	Width (also, W)
XPS	X-ray photoelectron spectroscopy

SUMMARY

Capacitive radio frequency (RF) micro-electromechanical (MEMS) switches are among the most promising applications in MEMS systems. They have been introduced in the last 15-20 years as a practical alternative over traditional semiconductor switches. Low-cost RF MEMS switches are prime candidates for replacing the conventional GaAs Field Effect Transistors (FET) and pin diode switches in RF and microwave communication systems, mainly due to their low insertion loss, good isolation, linear characteristic and low power consumption. Unfortunately, their commercialization is currently hindered by reliability problems. The most important problem is charging of the dielectric, causing unpredictable device behavior. The charging of the dielectric has been found to be a complicated process and is currently under intense research. Developing a good analytical model that would describe accumulating of charges in the dielectric and their influence on the device behavior would be the main step to achieving more reliable switches.

This work intends to theoretically and experimentally investigate the dielectric charging effects of capacitive RF MEMS switches with silicon nitride and silicon dioxide as the dielectric layer. For the silicon nitride study, both MEMS switches and MIM capacitors were fabricated, and their charging behaviors were analyzed and compared. Several different dielectric stoichiometries, deposition temperatures, and thicknesses

were examined in order to understand the effects of each parameter on the charging mechanisms of the dielectric. The goal was to determine the most favorable deposition conditions to induce minimum dielectric charging in silicon nitride capacitive switches. The switches were measured over a wide temperature range and the temperature-dependent behavior of the dielectric was examined to characterize and study its charging behaviors. For the silicon dioxide MEMS switches, several different actuation mechanisms were systematically analyzed, and their effects on the dielectric charging of the switches were studied. A general model of distributed charge and air gap was adopted and further developed to better explain the charging behavior of MEMS switches. The goal was to provide a deeper insight into the trapping processes in dielectric materials and their corresponding time constants. This will in turn aid in better modeling of charging processes in capacitive RF MEMS switches.

CHAPTER 1

INTRODUCTION

1.1 Introduction to Capacitive RF MEMS Switches

Radio frequency (RF) micro-electromechanical (MEMS) switches are devices that induce a short circuit or an open circuit in an RF transmission line using mechanical movement. RF MEMS switches are specifically designed to operate at RF-to-millimeter-wave frequencies (0.1-100GHz). The required force to generate the mechanical movement of the switch can be attained through electrostatic, magnetostatic, piezoelectric, or thermal actuations. To date, electrostatic-type switches have been studied extensively, and wafer-scale manufacturing techniques and relatively high reliabilities have been demonstrated for these switches.

The physical structure of a typical capacitive RF MEMS switch is shown in Figure 1.1 [1]. It is comprised of a fixed bottom electrode, a top movable membrane and a thin dielectric layer between the two metal layers. It is designed for a very low capacitance between the top membrane and the bottom signal line in the up state. Once the required voltage is applied through the actuation electrode, the top membrane is deflected due to electrostatic forces and as it touches the bottom electrode, a larger metal-insulator-metal capacitor is formed. Figure 1.2 shows the equivalent circuit model for both airbridge and cantilever type RF MEMS capacitive switches. Both switches can be modeled with a simple parallel or series RLC electrical circuit.

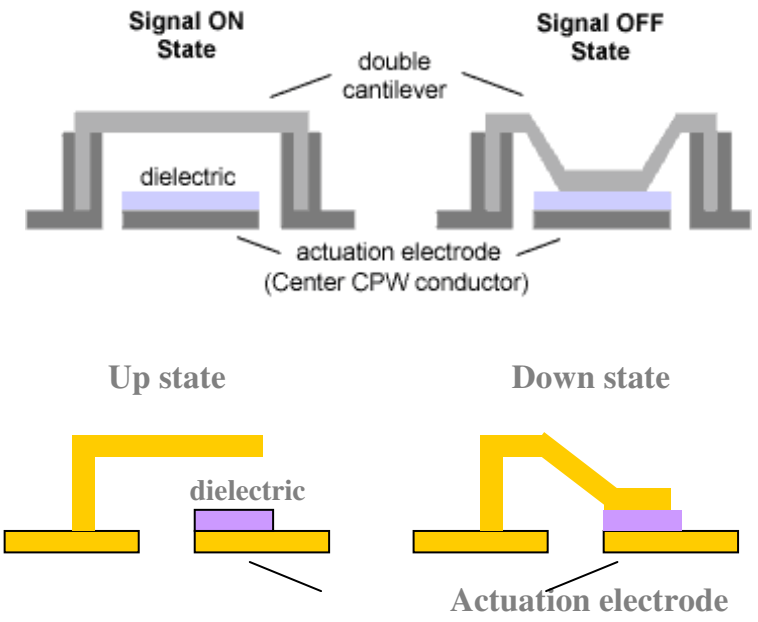

Figure 1.1. Structure of a typical capacitive RF MEMS shunt (top) and series (bottom) switch.

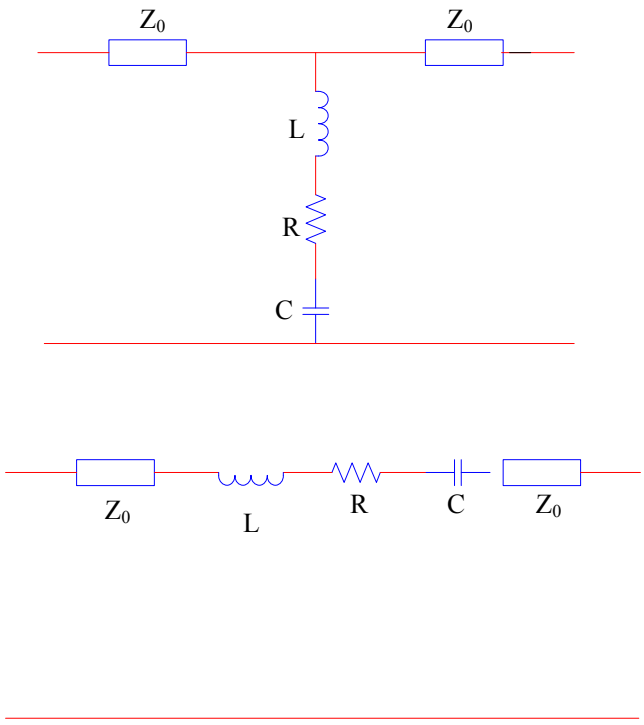

Figure 1.2. Equivalent circuit model for airbridge (top) and cantilever switches (bottom).

In MEMS capacitive switches, a thin dielectric layer is placed on top of the center conductor (Figure 1.1), so that the device essentially switches between two capacitance states. Typically a thickness of about 2000ºA to 3000ºA of silicon nitride or silicon dioxide is used. Once the electrode geometries and the dielectric material permittivity are known, the capacitance in the two states can be computed using parallel plate formulas. A side view of a MEMS switch in a coplanar waveguide (CPW) configuration is shown in Figure 1.3 [2]. The membrane in this case is an air-bridge between the ground electrodes, which are a natural component of any coplanar waveguide circuit and therefore no extra processing is required to incorporate them. The switch is designed so that the capacitance in the up state is small compared to the line capacitance, causing it to act as an open circuit. When a bias above the threshold voltage of the switch is applied between the center conductor and the ground, the switch is closed, introducing a shunt capacitor along the line (Figure 1.3). This on-state capacitance is designed to be an effective short circuit at RF frequencies, shorting the RF signal to ground.

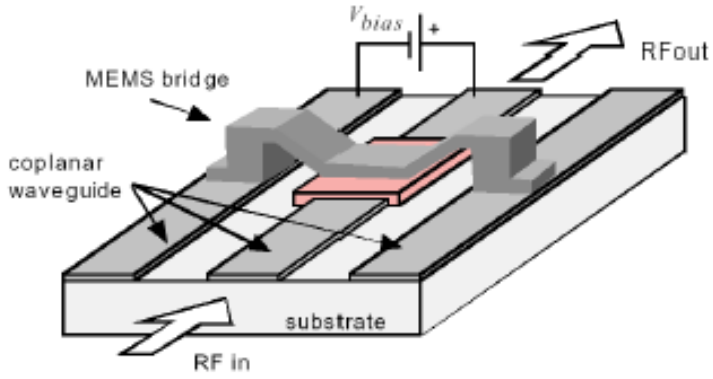

Figure 1.3. Coplanar waveguide (CPW) implementation of a capacitive RF MEMS switch [2].

For applications where the operation frequency is less than about 1 GHz, solid-state switches are still widely used. They are cheap, low loss, easy to integrate, and widely available. However, above a few gigahertz, their losses begin to increase and they become more difficult to integrate. This is where the advantages of MEMS switches become apparent. They are neither as fast nor as robust as their solid-state counter-parts, but they make up for it in electrical performance. The advantages of RF MEMS switches over pin diodes and FET switches are summarized below.

1. **Very Low Insertion Loss:** Both series and shunt RF MEMS switches have an insertion loss of 0.1 dB up to 40 GHz [2, 3].
2. **Very High Isolation:** RF MEMS switches have very low off-state capacitances (due to the airgap capacitance in the off-state), resulting in excellent isolation up to 80 GHz [2, 3].
3. **Near-Zero Power Consumption:** A typical electrostatic switch requires an actuation voltage of about 20-80 V, but does not consume any current. This leads to very low power dissipation (10-100 nJ per switching cycle) [3, 4]. Thus, MEMS switches seem to be excellent candidates for battery-operated or hand-held devices, as well as satellite and space systems, where low-power consumption is critical.
4. **Linearity:** MEMS switches have very low inter-modulation products because they don't have the intrinsic nonlinear transfer characteristics as compared with the traditional pin diodes or FET switches. Their performance is about 30 dB better than pin diodes or FET switches.
5. **Very Low Cost:** RF MEMS switches are fabricated using surface micromachining techniques. They can be built on quartz, pyrex, low-temperature co-fired ceramic

(LTCC), mechanical-grade high-resistivity silicon, GaAs substrates, or even flexible polymer substrates [5].

6. **Small Size:** RF MEMS devices have shown significant reduction in size and weight while maintaining high performance compared with the conventional technologies. The miniature size and reconfigurability of RF MEMS devices allows significant reduction of circuit-board size by combining several switching networks into one reconfigurable chip, thereby making RF MEMS technology favorable for multi-band hand-held devices.

However, RF MEMS switches have a number of problems as well. These are described below:

1. **Relatively Low Speed:** The switching speed of most MEMS switches is around 2-40 μsec (due to their mechanical movement). Certain communication and radar systems require much faster switches.
2. **High Actuation Voltage:** Most electrostatic MEMS switches require 20-80V for reliable operation. This will require a voltage up-converter when used in portable telecommunication systems. This adds to system complexity and cost.
3. **Power handling capability:** Most capacitive RF MEMS switches cannot handle more than 500 mW with high reliabilities [6]. Ohmic RF MEMS switches have been reported to have higher power handling capabilities, but DC contacts are prone to damage during hot switching, far more than capacitive contacts. Hot switching can cause stiction, increased contact resistance, or outright destruction [7].
4. **Reliability:** The reliability of mature capacitive RF MEMS switches is 1-100 billion cycles [8, 9]. However, many systems require switches with more cycles. Ohmic

(DC-contact) switches have been reported to achieve up to a trillion cycles in cold-switching conditions [10]. However, cold-switching is not practical in real world situations. Hot-switching is the more realistic testing method. It has been observed that hot switching operation can cause the switch lifetime to be several orders of magnitude lower than the cold-switching lifetime [11]. The predominant failure mechanisms of DC-contact switches are damaging, pitting, and hardening of the metal contact. Pitting and hardening occur when two metal electrodes hit each other repeatedly. This will significantly reduce the real contact area, resulting in a sharp increase of the contact resistance. Moreover, arcing between the cathode and the anode during hot switching operation presents a big reliability concern [11, 12]. Capacitive switches are designed to bypass the contact degradation problem in DC-contact switches. Since the switch is a variable capacitor, it cannot work for DC signal switching applications. The capacitive switch has its own reliability problem, which is charging of the dielectric. Charging failure is not permanent and switches can restore to their initial state after the trapped charges are discharged. In both DC-contact and capacitive switches, mechanical failure (metal fatigue or fracture) of well-designed cantilever or fixed-fixed beams has not been a limiting factor for the switch lifetime since the amount of deflection during switch actuation is relatively small compared to the beam size.

Another major concern in communication systems is the reliability of the switch for long-term applications. That is, whether the switch would fail if actuated in the down-state for several hours or days with RF power passing through the contact areas. This issue has not yet been addressed in RFMEMS switches.

5. **Packaging:** The most critical part of RF MEMS switches is the packaging technology used. It is the most expensive step and will ultimately determine the cost of the switch or switch network. MEMS switches need to be packaged in inert atmospheres (nitrogen, argon, etc.) and in very low humidity, resulting in hermetic or near-hermetic seals. There are a variety of packaging schemes, most accomplished at the wafer level. Wafer-level packaging is a relatively low-cost packaging method and enables the switch to be packaged while still in a clean, controlled environment (the cleanroom). Most MEMS switch packaging schemes involve either wafer-bonding or micro-encapsulation. In wafer-bonding, a lid wafer is fabricated and bonded to the MEMS substrate, enclosing each MEMS switch with a small cavity. In wafer-level microencapsulation, additional sacrificial and structural layers are added to the MEMS device to create a superstructure around the switch, which is then sealed by a liquid encapsulant or chemical vapor deposition [13].

   Packaging costs are currently high, and the packaging technique itself (high temperature bonding, etc.) may adversely affect the reliability of the MEMS switch. Recently however, hermetic wafer-caps have been developed by several companies and labs showing great promise to reduce the packaging cost in near future [14-16].

6. **Cost:** Although RF MEMS switches have low manufacturing costs, the cost of packaging is high and a high-voltage drive chip is also usually needed. It is therefore difficult to compete with a $0.30-0.60 single-pole double-throw 3-V pin diode or FET switch, tested, packaged, and delivered.

A comparison of a typical RF MEMS, PIN diode, and FET switching element is summarized in Table 1.1 [17].

Table 1.1.
Comparison of electrical performances of a typical RF MEMS, PIN diode, and FET switch.

Parameter	**RF MEMS**	**PIN Diode**	**FET**
Voltage (V)	20-80	+/- 3-5	3-5
Current (mA)	0	3-20	0
Power Consumption (mW)	0.05-0.1	5-100	0.05-0.1
Switching Time	1-300 μS	1-100 ns	1-100 ns
C_{up} (series) (fF)	1-6	40-80	70-140
R_s (series) (Ω)	0.5-2	2-4	4-6
Capacitance Ratio	40-500	10	N/A
Cutoff Frequency (THz)	20-80	1-4	0.5-2
Isolation (1-10GHz)	Very high	High	Medium
Isolation (10-40 GHz)	Very high	Medium	Low
Isolation (60-100 GHz)	High	Medium	None
Insertion Loss (1-100GHz) (dB)	0.05-0.2	0.3-1.2	0.4-2.5
Power Handing (W)	<1	<10	<10
3^{rd} Order Intercept (dBm)	+66-80	+27-45	+27-45

RF MEMS switches have been the most prevalent application of the RF MEMS technology in the past decade, simply because switching networks are used in almost every communication system. They have already been utilized with antennas, filters,

phase shifters, oscillators, multiplexers, and other traditional RF devices [18-20]. Their main applications are summarized below [2, 3]:

1. Radar Systems for Defense Applications (5-94 GHz): Phase shifters for satellite-based radars (20 billion cycles), missile systems (0.1-1 billion cycles), long-range radars (20- 200 billion cycles).
2. Automotive Radars: 24, 60, and 77 GHz (1-4 billion cycles and 10 years).
3. Satellite Communication Systems (12-35 GHz): Switching networks with 4x4 and 8x8 configurations and reconfigurable-Butler matrices for antenna applications (0.1 million cycles), switched filter banks (0.1-100 million cycles, depending on the application). Also, phase shifters for multi-beam satellite communication systems (1-20 billion cycles).
4. Wireless Communication Systems (0.8-6 GHz): Switched filter banks for portable nits (0.1-1 million cycles), switched filter banks for base stations (0.1-10 billion cycles), general SP2T to SP4T switches (0.1-10 billion cycles), transmit/receive switches (2-4 billion cycles and 5-20 μs switching time), and antenna diversity SP2T switches (10-100 million cycles).
5. Instrumentation Systems (0.01-50 GHz): These require high-performance switches, programmable attenuators, SPNT networks, and phase shifters capable of at least 20-40 billion cycles and 10 years of operation, especially in industrial test benches.

1.2 RF MEMS Switch Development

MEMS switches as we know them today were conceptualized in the late 1980s and early 1990s. The first published papers were entirely theoretical and pointed out

some of the design challenges and potential uses of MEMS devices [21]. MEMS switches in particular were of great interest to RF engineers for their potential ability to reduce the total area, power consumption, and cost of their devices. Early MEMS research was funded and performed by industry leaders looking for applications in a variety of areas, including optics, transportation, aerospace, robotics, chemical analysis systems, biotechnologies, and medical engineering. In time, it was expected that MEMS could be used for flat panel displays, optical switches, fiber optics, and integrated sensors. However, it was understood that many reliability issues would have to be solved before these advanced technologies were possible. Early MEMS switches were overwhelmed with electrical and mechanical issues, such as dielectric charging, substrate delamination, creep, and fatigue [22].

Prior to the new century, accurate numerical solvers were not available to MEMS designers. Research was largely performed by fabricating the devices, testing, and redesigning. This of course is a slow and expensive process. In December 1996, the Defense Advanced Research Projects Agency (DARPA) invested more than $17 million in government funding aimed at improving the computer-aided design technology for MEMS devices [23]. Several useful software programs have since been developed, including CoventorWare [24], IntelliSuite [25], and the COMSOL MEMS Module [26].

MEMS devices quickly surpassed the RF performance of their solid-state equivalents. Even early MEMS switches had an insertion loss of 0.15 dB at 20GHz, compared to an on-state insertion loss of approximately 1 dB for a typical GaAs-FET or PIN-diode switch at the same frequency [27].

Today, many of the devices predicted in the 1990s are commercially available. MEMS switches in particular can be purchased with insertion losses as low as 0.1 dB up to 50 GHz with the potential for operating more than 100 billion cycles. Ohmic switches with multi-watt power-handling capability have been reported [28].

1.3 Mechanical Design of Capacitive RF MEMS Switches

Equations for predicting the bending of cantilever and doubly-supported beams have been around for decades [29]. However, the scale and relative importance of the forces acting on the switches are significantly different from the macro-world we experience daily. Surface forces and viscous air damping dominate over inertial and gravitational forces. The switches are either fabricated using a fixed-fixed membrane or a floating cantilever (diving-board design) and are modeled as mechanical springs with an equivalent spring constant k [N/m]. The spring constant depends on the geometrical dimensions of the membrane or cantilever and on the Young's modulus of the material used (Au, Al, nitride, etc.) [30, 31] and is 5-40 N/m for most RF MEMS switch designs. The switches have very low mass, around 10^{-10}-10^{-11} kg and are therefore not sensitive to acceleration forces. The switches are suspended 1.5-4 μm above the transmission line.

The effective spring constant for a meandered line can be derived from (1.1) [32]:

$$k_m = \frac{Ew\left(\frac{t}{L_c}\right)^3}{1+\frac{L_s}{L_c}\left(\left(\frac{L_s}{L_c}\right)^2+12\frac{1+\nu}{1+\left(\frac{w}{t}\right)^2}\right)} \tag{1.1}$$

where E is the Young's Modulus of the membrane material, v is the poisson's ratio of the membrane, w is the width of the meander, L_s is the overall width of the spring, and L_c is the distance from the end of the spring to the start of the meander. These dimensions are illustrated in Figure 1.4.

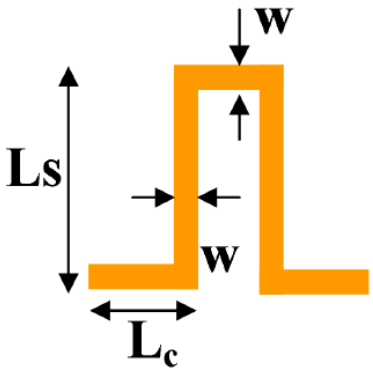

Figure 1.4. Illustration of dimensions for (1.1).

For a non-meandered spring, the spring constant is given by [33]:

$$k_{n-m} = \frac{32EWH^3}{L^3} \tag{1.2}$$

where E is the Young's Modulus, W is the width, H is the thickness, and L is the length of the actuation electrode.

The effective spring constant, k_{eff}, for the entire MEMS switch can be determined by combining the simple spring equations in a manner similar to capacitors. That is, springs in parallel add directly and springs in series add as the inverse of the sum of the reciprocals [34]. The spring constant of N such structures in series and parallel are k_{eff}/N and Nk_{eff} respectively.

The switches considered in this work are double-supported capacitive type. The inductive regions behave like springs and make it easier to deflect the beam. A spring

constant can be determined which evaluates the amount of force necessary to deflect the beam a given distance. Changing the shape or dimensions of the inductive region will increase or decrease the spring constant. The capacitive regions are responsible for creating an electrostatic force between the DC biased beam and the metal layer below it. This force is responsible for decreasing the "gap" between the metal layers. Changing the gap length, height, or the area of the capacitive region will increase or decrease the electrostatic force necessary to deflect the beam.

There are four popular inductive region configurations for double-supported capacitive switches [32], [34]. These designs, labeled 1-4, are shown in Figure 1.5.

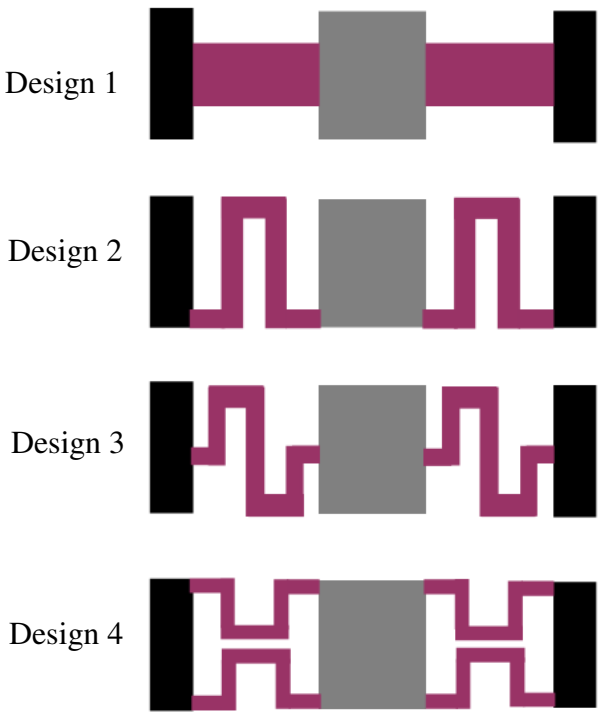

Figure 1.5. Four different MEMS switch geometries [34].

The effective spring constants for the four switch designs are thus given by [34]:

Design 1:

$$k_{eff} = \frac{32EWH^3}{L^3} \tag{1.3}$$

Design 2 has two meander springs in series with a non-meander spring. The effective constant is:

$$k_{eff} = \frac{k_m k_{n-m}}{k_m + 2k_{n-m}} \tag{1.4}$$

Design 3 has 4 meander springs in series with a non-meander spring. The effective constant is:

$$k_{eff} = \frac{k_m k_{n-m}}{k_m + 4k_{n-m}} \tag{1.5}$$

Design 4 has two meander springs in parallel and in series with another two parallel meander springs and a non-meander spring. The effective constant is:

$$k_{eff} = \frac{k_m k_{n-m}}{k_m + k_{n-m}} \tag{1.6}$$

where k_m and k_{n-m} are found from (1.1) and (1.2), respectively.

Two of the most important mechanical features of a MEMS switch are the pull-down voltage and deflection. In order to calculate the pull-down voltage, one must equate the force pulling down on the beam by the electrostatic force between the metal layers:

$$F_e = \frac{QE}{2} = \frac{CVE}{2} = \frac{CV^2}{2\left(g + \frac{t_d}{\varepsilon_r}\right)} = \frac{\varepsilon A V^2}{2\left(g + \frac{t_d}{\varepsilon_r}\right)^2} \tag{1.7}$$

where V, g, and C are the voltage, gap distance, and capacitance between the lower and upper electrodes, respectively, and A is the area of the electrode. The bottom electrode is often covered by a dielectric layer with a thickness of 100-200 nm and a relative dielectric constant (ε_r) between 3 and 8 [2]. As the switch is pulled down to the bottom electrode, the gap is reduced, and the pull-down force on the switch increases.

On the other hand, there is a pull-up force due to the spring constant of the switch. The equilibrium is achieved when both forces are the same:

$$F = \frac{\varepsilon A V^2}{2\left(g + \frac{t_d}{\varepsilon_r}\right)^2} = k\left(g - g_0\right) \tag{1.8}$$

where g_0 is the initial height of the bridge.

It has been well documented that for parallel plate electrostatic actuation, when the gap reduces to 2/3 of the original gap, the beam becomes unstable and experiences a "pull-in" effect [35]. That is, the MEMS switch does not deflect over the entire gap according to (1.7). Instead, when the gap reaches a certain threshold, namely 2/3 the original gap, the switch will snap down. Equating (1.7) and (1.8) where the gap is 2/3 of the original gap and solving for the pull down voltage results in:

$$V_P \cong \sqrt{\frac{8kg_0^3}{27\varepsilon A}} \tag{1.9}$$

The maximum deflection can also be calculated from the spring constant by the following equation [29]:

$$\delta = \frac{-F}{k} \tag{1.10}$$

where δ is the deflection, F is the force pushing down the spring, and k is the spring constant.

The applied voltage is typically 1.2-1.4 V_p so as to achieve fast operation of the switch. Once the switch is pulled down and the gap is reduced to 0 μm (dc-contact switches) and 0.3-0.5 μm (capacitive switches), the electrostatic voltage can be reduced to 0.4-0.7 V_p while still keeping the switch in the down-state position [2]. This is done so as to reduce the electric field in the dielectric and decrease the possibility of dielectric breakdown or charge injection into the dielectric.

MEMS switches also follow standard Newtonian's mechanics. The dynamic response of the switch is given by:

$$mg'' + bg' + k(g - g_0) = F_e \tag{1.11}$$

where m and b are the mass and damping coefficient of the membrane, and F_e is the electrical force given in (1.7). This is a second-order system with a resonant frequency

of $\omega_0 = \sqrt{k/m}$. A switch with a low mass and a spring constant of 5-30 N/m will have a resonant frequency of about 30-100 kHz.

The quality factor of the switch (Q) can be written in terms of the damping coefficient (b) as $Q = k/\omega_0 b$. The damping is limited by squeeze-film effects (removing of the air beneath the bridge or cantilever). For most designs, Q is between 0.2-5. A low Q value results in a slow switch. It is important to operate the switches around atmospheric pressures and to keep Q around 1 (squeeze-film damping is good). If the switch is operated in vacuum, the Q may be as high as 50-1,000 depending on the material of the membrane and the anchor design.

A simple equation has been derived in [36] for the switching time:

$$t = 3.67 \frac{V_p}{V_s \omega_0} \tag{1.12}$$

Simulations in [36] show that (1.12) is accurate to within 10% for Q>1 and V_S>1.3V_p. For a switch with w_0=50 kHz and V_S =1.3V_p, the switching time is 9 μs. Most MEMS switches have a switching/release time of 2-50 μs.

1.4 Electrical Design of Capacitive RF MEMS Switches

As shown in Figure 1.2, the capacitive switch behaves like a series (cantilever switch) or parallel (shunt or air-bridge type) RLC circuit. The springs exhibit an inductance, the actuation region exhibits a capacitance, and the metal beam exhibits a

resistance. In order to evaluate the RF characteristics of the switch, it is important to calculate the values of *R*, *L* and *C* since the resonant frequency of the switch is given by:

$$f = \frac{1}{2\pi\sqrt{LC}} \tag{1.13}$$

The *R*, *L* and *C* values can be calculated within an order of magnitude by using fundamental equations. The resistance can be calculated using [37].

$$R = \frac{\rho L}{HW} \tag{1.14}$$

where ρ is the resistivity of the metal beam, *L* is the length of the beam, *H* is the thickness, and *W* is the width of the beam. The capacitance can be calculated by:

$$C = \frac{\varepsilon A}{g} \tag{1.15}$$

where *A* is the effective contact area of the electrode, *g* is the thickness of the dielectric layer, and ε is the permittivity of the dielectric material.

There are several ways to get the value of the inductance. One way is to use (1.13). Another method is to fit the measured data to get the parameters (*R*, *L*, and *C*) using Agilent ADS simulation tools with a simple RLC circuit as shown in Figure 1.2.

In order to design RF MEMS capacitive switches for high frequency (> 50 GHz) applications, it is essential to design the switch with a very high resonant frequency.

CHAPTER 2

POLARIZATION/CHARGING MECHANISMS

2.1 Charging Effects in Capacitive RF MEMS Switches

The major reliability problem in capacitive RF MEMS switches is the stiction between the metal layer (top electrode) and the dielectric layer covering the bottom electrode. The main stiction force is believed to be due to charge build-up in the dielectric [38-50]. Depending on the polarity of the injected charge, this can cause the switch to either stick in the down-state position, or experience an increase in the pull-down voltage so that the MEMS switch is not usable anymore. The electric field can be as high as 3-5 MV/cm in the dielectric layer, which results in a Poole-Frenkel (PF) charge injection mechanism from the metal to the dielectric [51]. Charge injection has been reported to be exponential with voltage, and a reduction in the pull-down voltage by 6 V can result in a 10× increase in the lifetime of the MEMS switch [51]. This does not automatically lead to the design of low-spring constant, low-voltage switches (5-10 V) since these switches have a low restoring (pull-up) force. A pull-down voltage of 25-30 V may be the best compromise. Also, it is well known that silicon dioxide has a much lower trap density than silicon nitride and may result in less charging when used in RF MEMS capacitive switches. The penalty paid is a decrease in the down-state capacitance (or capacitance ratio) due to the lower dielectric constant of the oxide material.

In [38], Wibbeler et al. described the impact of dielectric charging on the actuation of electrostatic MEMS switches. Considering the simple device model in Figure 2.1, they demonstrated that the presence of a uniform charge distribution at the surface of

the dielectric layer shifts the symmetric C–V actuation characteristic as a whole along the voltage axis, as shown in Figure 2.2. The direction of this shift depends both on the sign of the trapped charges and on the way the voltage source is connected to the device, i.e., top or bottom electrode grounded and, respectively, bottom or top electrode biased.

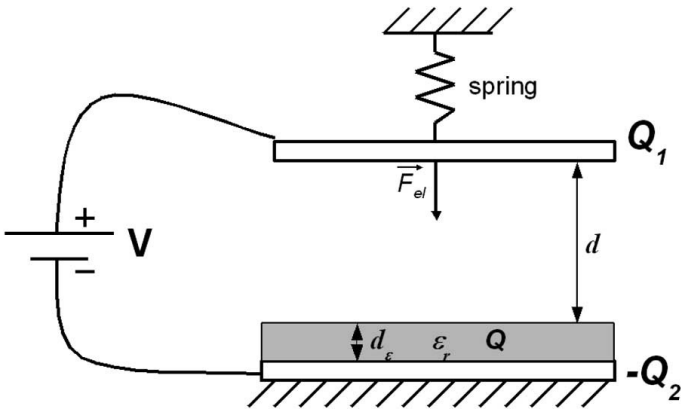

Figure 2.1. Electromechanical model of a MEMS switch used by Wibbeler et al. [38].

The voltage across the air gap (Figure 2.1) can be written in the simple form of:

$$V_{Actuation} = V_{airgap} = \frac{V - Q/C_2}{1 + C_1/C_2} \tag{2.1}$$

where C_1 is the (variable) capacitance of the airgap, C_2 is the (fixed) capacitance corresponding to the dielectric layer alone, and Q is the total stored charge on the surface of the dielectric (Figure 2.1):

$$Q = Q_1 - Q_2 \tag{2.2}$$

with Q_1 and $-Q_2$ being the stored charge on the top and bottom metal plates.

The electric force exerted on the top metal plate can be written in the form of:

$$F_{el}(d) = \frac{C_1(d)V_{airgap}^2}{2d} = \frac{C_1(d)C_2^2}{2d(C_1(d)+C_2)^2}\left(V - \frac{Q}{C_2}\right) \tag{2.3}$$

The C-V curve will thus shift by the amount of Q/C_2 along the voltage axis. Figure 2.2 shows the shift in the C-V curve for a positive surface charge Q>0.

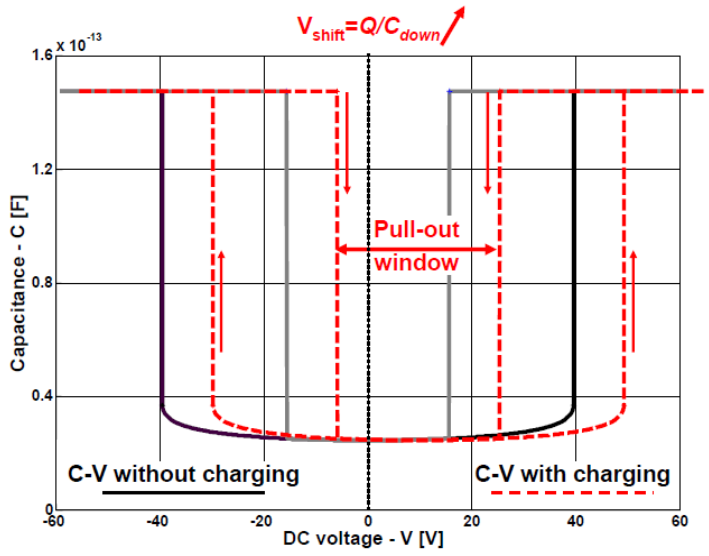

Figure 2.2. Shift of the C–V curve with a uniform surface charge [44].

When the surface charge Q is so large that the pull-out voltage crosses the zero line (Figure 2.3), the device will fail due to charge-induced stiction. This effect cannot be explained with the behavior described above and is believed to be due to the difference in speed between the electronic actuation signal and the mechanical response of the switch. If the actuation voltage decreases to 0 V fast enough compared to the resonance frequency of the device, as in normal operation, the switch will have no time to move back up completely before the negative curve is crossed. This means that the device is

still down when the voltage has returned to 0 V. The negative or positive (depending on the polarity of the surface charge stored in the dielectric) pull-out voltage that has crossed the zero line is now responsible for this sticking behavior of the bridge [44, 45].

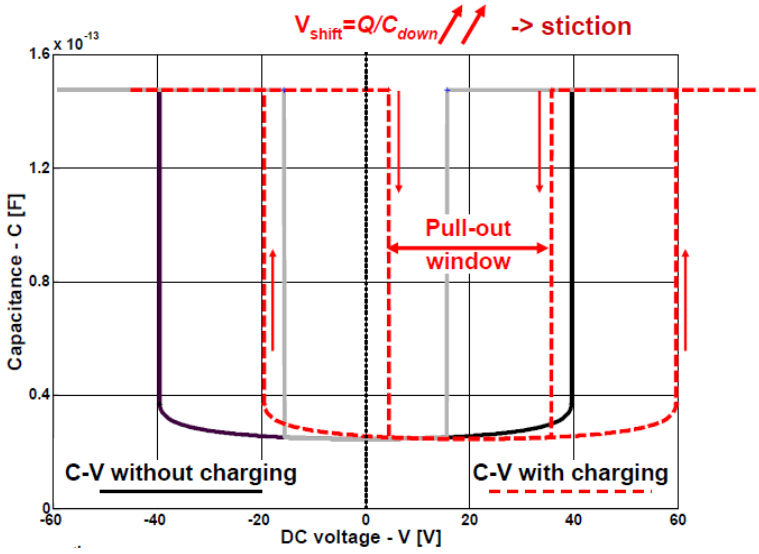

Figure 2.3. Shift of the C–V curve with a uniform surface charge [44]. The surface charge is so large that the pull-out window crosses the zero line.

There have been several attempts to minimize the stress on the dielectric layer, and thus the resulting built-in charges. One way is to lower the actuation voltage of the switch as explained earlier. Various complex actuation schemes have also been proposed, such as shaped actuation pulses [51] and bipolar actuation voltages [52]. These techniques tend to keep the total dielectric charge close to zero, thus keeping the C–V characteristics more centered on the bias origin at 0 V, preserving the normal actuation of the switches. However, switches tested under such actuation mechanisms exhibit a narrowing of their pull-out windows, as shown in Figure 2.4, among other phenomena. This will in time lead to vanishing of their pullout voltages and an irreversible stiction [39], [44], [46], [53]. Figure 2.4 also shows an upward shift in the C-V curve, which is

the result of an increase in the up-state capacitance. This increase can be attributed to a non-zero variance of the charge, although the total amount of dielectric charge is kept close to zero.

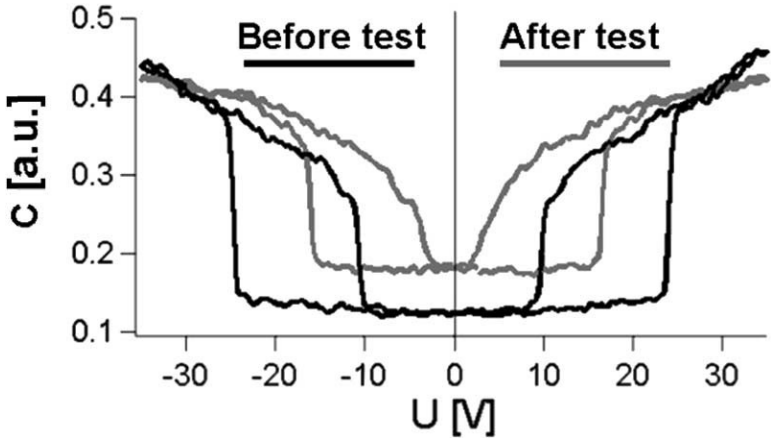

Figure 2.4. Measured fast C–V characteristic before and after 20 million cycles of bipolar actuation at ±35 V under a 1-bar N_2 atmosphere at 25°C with 50% duty cycle for an Al-based switch using SiN_x as dielectric material [53].

To better understand the effects of charging under zero total dielectric charge and non-zero variance, we consider the setup sketched in Figure 2.5. A fixed metal plate is covered with a dielectric layer split in two parts with equal areas. The two dielectric islands have uniform fixed surface charges of opposite signs (+/-Q). A movable metal plate is fastened with a spring above the dielectric layer. A DC voltage source is applied across the two plates. The +/-Q charges shift the force-voltage characteristics by +/-V_{shift}, which are opposite quantities for the 2 dielectric islands. It is interesting to observe that although the net dielectric charge is zero, the resulting electrostatic force F_{el} is not zero, even at 0 applied voltage.

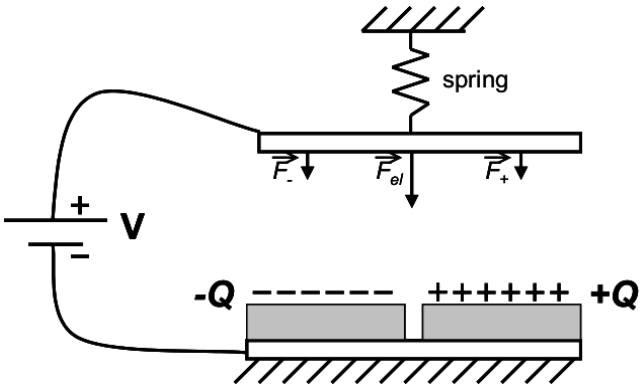

Figure 2.5. Charging of the dielectric with zero mean and non-zero variance [54].

The increase of the up-state capacitance can be explained using the 2D+ model proposed in [54] (Figure 2.6). Assuming a uniform air gap and a volume charge density in the dielectric with non-zero mean and variance values $\Psi(x,y,z)$, the electric force inserted on the top metal plate can be written as:

$$F_{el}(d) = \frac{C_1(d)C_2^2}{2d\left(C_1(d)+C_2\right)^2}\left\{\left(V - Q_{eq}/C_2\right)^2 + \frac{Area^2}{C_2^2}\sigma^2(\psi_{eq})\right\} \tag{2.4}$$

where $\Psi_{eq}(x,y)$ is the equivalent surface charge distribution on the dielectric, $\sigma^2(\Psi_{eq})$ is the variance of the equivalent surface charge distribution, and Q_{eq} is the total charge stored in the dielectric (Q_{eq} = *Area x mean of* $\Psi_{eq}(x,y)$).

Q_{eq} will therefore cause a voltage offset (x-shift in the F_{el} vs. V curve) equal to Q_{eq}/C_2, and $\sigma^2(\Psi eq)$ will cause a force offset (y-shift in the F_{el} vs. V curve).

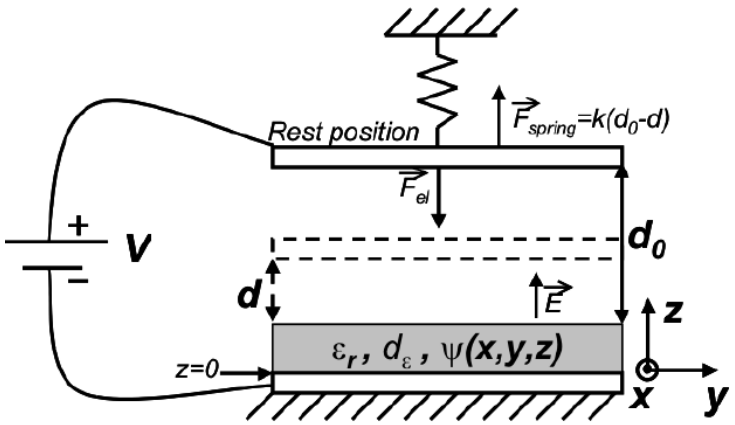

Figure 2.6. Model of an RF MEMS switch with distributed charging [54].

2.2 Polarization Mechanisms in Dielectrics

The interaction of microwaves with dielectric materials causes a net polarization of the substance. Several mechanisms are responsible for this occurrence, namely: electronic, ionic, molecular (dipole), and interfacial (space-charge) polarizations [55-57]. Applying an electric field to each of these mechanisms in a normal state will cause a charge displacement resulting in a polarization in the direction of the field. Figure 2.7 shows this effect on each mechanism. For a given material, the sum of the contributions from each mechanism determines the net polarization, *P*, of the dielectric material. A brief overview of each polarization mechanism is given below.

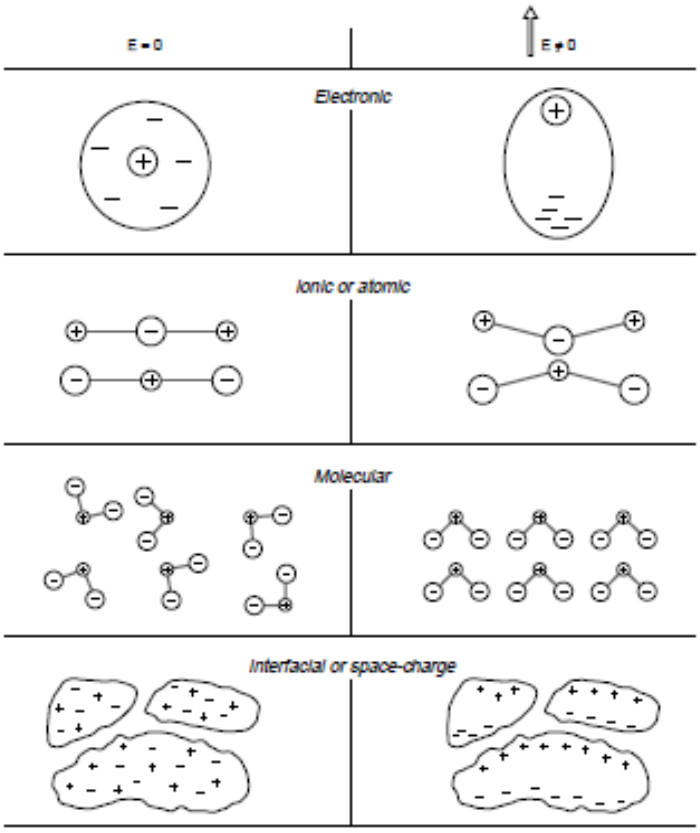

Figure 2.7. Polarization Mechanisms in Dielectrics [55].

1. Electronic Polarization

For a dielectric material in a normal state, electrons are bound to their parent atoms and are fixed in their equilibrium positions. Electronic polarization occurs upon applying an electric field, under which the electrons are shifted from equilibrium with respect to the positive nuclei in the direction of the field. In this state the atom acts as a temporary induced dipole. This mechanism occurs in all materials and is the fastest polarization mechanism in dielectrics. The response time is about 10^{-15} seconds.

2. Ionic (atomic) polarization

Ionic (atomic) polarization occurs in materials containing permanent ionic dipoles. It differs from the electronic mechanism in that it occurs due to the relative motion of the atoms instead of a shift of the electron clouds surrounding the atoms. Under an applied field, a separation of charges is caused which yields a displacement of the cations and anions in crystals relative to their equilibrium positions. Specifically, cations are attracted toward the negative electrode and anions are attracted toward the positive electrode. Response time for this mechanism can take 10^{-14}-10^{-12} seconds.

The other polarization mechanisms [58], [59], which are responsible for the "dielectric charging" effects, are characterized by a time constant that may be as low as 10^{-12} seconds or as large as years, so that no relaxation could be observed under the conditions of observation. These mechanisms are called slow and may occur through a number of processes involving either microscopic or macroscopic charge displacement. The slow polarization mechanisms are described below:

3. Molecular (dipolar) polarization

Molecular or dipolar polarization occurs in materials containing permanent molecular dipoles. Molecules are randomly oriented in the normal state in a material so that there is no net charge present. When an external electric field is applied to the dielectric, it aligns the permanent dipoles parallel to the field. Relaxation time for this mechanism depends on the frictional resistance of the medium and can take between 10^{-12} seconds to several days. The dipolar polarization of inorganic crystals may be caused by structural properties of the crystal lattice or it may be due to lattice imperfection or doping, for example in impurity vacancy dipole systems. In MEMS switches, this

polarization leads to surface charges which have opposite polarity to those of the polarizing electrodes (hetero-charges).

4. Interfacial (Space Charge) polarization

Interfacial polarization occurs in heterogeneous materials containing free charges (ions, electrons). Mobile charge carriers in a heterogeneous material are accelerated by an applied electric field until they are impeded by and pile up at physical barriers. This charge build up determines the polarization of the material. Grain/phase boundaries and free surfaces are common barriers. The time required for this mechanism can vary from milliseconds to years.

Space charge polarization can be of two different origins: intrinsic and extrinsic. Polarization of intrinsic origin occurs due to redistribution of pre-existing charge carriers in the presence of an electric field and leads to hetero-charges (charges which have the opposite polarity of the polarizing electrodes). On the other hand, when a dielectric is submitted to high electric fields, excess electronic or ionic charge carriers are injected into the dielectric from the electrodes. This polarization is of an extrinsic origin and leads to homo-charges (charges with the same polarity as the polarizing electrodes). Both of these mechanisms cause the material to be spatially non-neutral. Space charge polarization is a much more complex phenomenon than the dipolar polarization.

The polarization resulting from the above mechanisms is strongly influenced by frequency. The individual polarization mechanisms have varied dependencies on the frequency of the applied electric field. In general the larger the masses involved, the slower the response upon application or removal of a field and consequently the

relaxation frequency is lower. For example, electronic and ionic polarization mechanisms undergo resonance in the optical and far infrared wavelengths respectively.

In two cases (electronic and ionic polarizations), the electric field will try to change the distance between the charges involved. In response, there is a restoring force that is approximately proportional to the separation distance of the dipole charges. We have, in mechanical terms, an oscillator. The characteristic property of any such oscillating system is the phenomena of resonance at a specific frequency [60].

In the case of dipolar polarization, there is no direct mechanical force that "pulls" the dipoles back to random orientation. Instead we have many statistical events that respond in their average results to the driving forces of electrical fields. In other words, if a driving force is present, there is an equilibrium state with an (average) net dipole moment. If the driving force were to disappear suddenly, the assembly of dipoles would assume a new equilibrium state (random distribution of the dipoles) within some characteristic time called relaxation time. The process knows no resonance phenomena, and is characterized by its relaxation time instead of a resonance frequency. We thus have to consider two basic situations: Dipole relaxation and dipole resonance. Every polarization mechanism in dielectric materials will fit into one of these two cases.

Figure 2.8 shows the real and imaginary parts of the permittivity of a dielectric material over a wide frequency range [60, 61]. The frequency axis is on a logarithmic scale. If the frequency is very large, no mechanical system would be able to follow. We thus expect that at very large frequencies all polarization mechanisms will "die out", i.e. there is no response to an extremely high frequency field. This means that the dielectric constant ε' will approach 1 for $f \rightarrow \infty$.

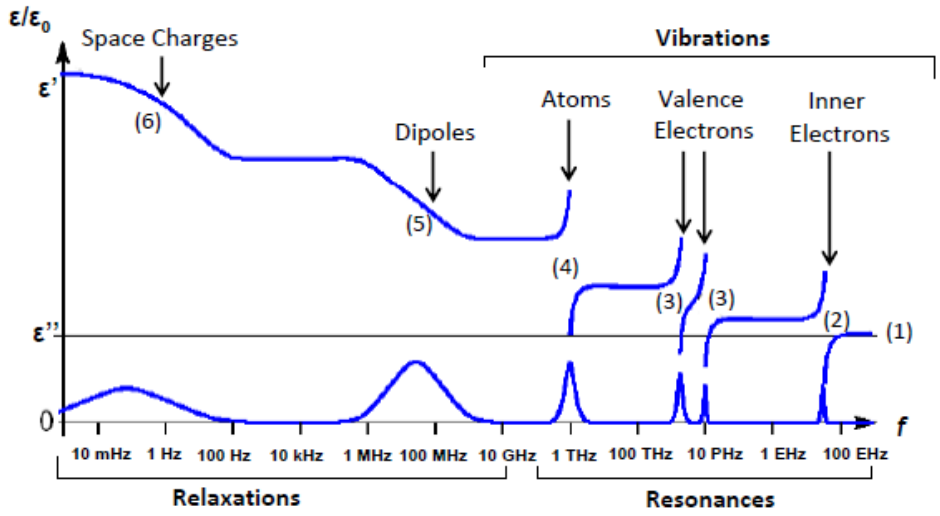

Figure 2.8. A dielectric permittivity spectrum over a wide range of frequencies [60, 61].

Figure 2.9 shows the time response of different polarization types under a step-function electric field [62].

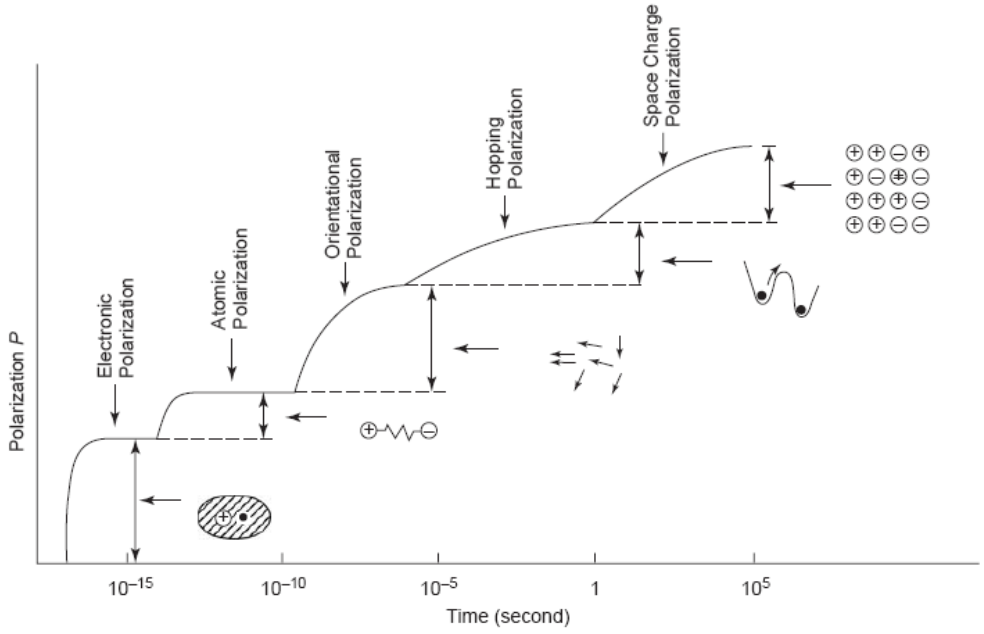

Figure 2.9. Variation of different types of polarization with time under a step-function electric field.

2.3 Charging/Discharging Processes in Capacitive RF MEMS Switches

In the case of MEMS switches, different charging mechanisms are present in the actuated and un-actuated states (Figure 2.10). In the un-actuated position, "contact-less" charging mechanisms are dominant. These consist of dipolar (P_D) and intrinsic space charge (resulting from redistribution of pre-existing and/or field generated charge carriers, $P_{SC\text{-i}}$) polarizations. Since both of these mechanisms lead to surface charges which have opposite polarity to those of the polarizing electrodes (hetero-charges), the total polarization of the dielectric can be written as:

$$P = P_D + P_{SC-i} \tag{2.5}$$

In the actuated position, extrinsic space charge polarization ($P_{SC\text{-e}}$) is also present ("contacted" charging). Unlike dipolar and intrinsic space charge polarizations, extrinsic space charge polarization leads to homo-charges. The total polarization can thus be written as [63]:

$$P = P_D + P_{SC-i} - P_{SC-e} \tag{2.6}$$

Equivalently, the total dielectric charge can be written as [63]:

$$\sigma = \sigma_D + \sigma_{SC-i} - \sigma_{SC-e} \tag{2.7}$$

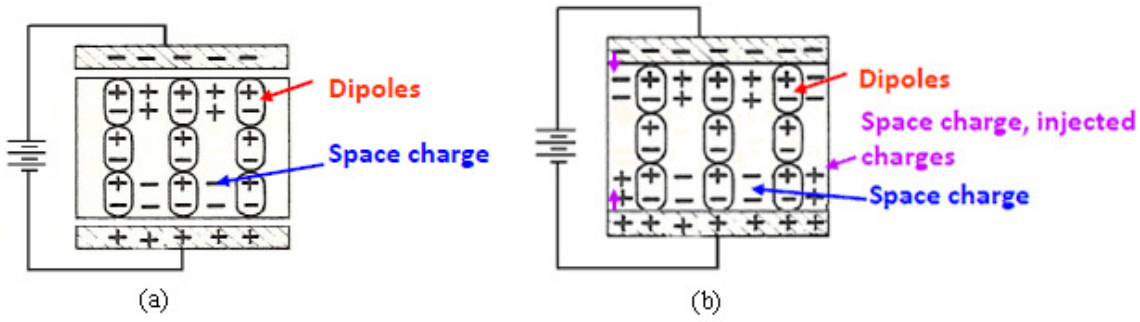

Figure 2.10. Charging mechanisms in MEMS switches (a) un-actuated position (b) actuated position.

The discharge process in MEMS capacitive switches in the off-state is different than the one investigated in MIM (metal-insulator-metal) capacitors. In MIM capacitors, the discharge currents are strongly affected by: (1) the partial dissipation of excess charges by space-independent intrinsic conductivity that passes unnoticed in the external circuit, and (2) the incomplete release of the image charges induced at the electrodes due to their partial neutralization by the excess charges, and (3) the dependence of the diffusion released current on the blocking character of the electrodes. In MEMS switches, the discharge occurs when the bridge is no longer in contact with the dielectric. This means that the discharge has to take place through the dielectric through a redistribution of dipoles' orientation and the diffusion and drift of injected charges under the presence of local electric fields. Therefore, discharging processes in real MEMS switches constitute a complex mechanism.

As for the charging process, as seen in Figure 2.10 (b), when the top membrane contacts the dielectric in a MEMS switch, charge can be injected either from the movable electrode onto the surface of the dielectric, or from the stationary electrode into the bulk of the dielectric. Although charge injection from the bottom electrode is similar in MIM

capacitors and MEMS switches, charge injection from the top electrode can be rather different due to non-ideal contact between the top electrode and the dielectric in MEMS switches.

It has been shown the charge injected from the movable electrode increases the magnitude of the pull-in voltage, whereas the charge injected from the stationary electrode decreases the magnitude of the pull-in voltage. The shift in the pull-in voltage is found to be [64]:

$$\Delta V = \left(h_T Q_T - h_B Q_B\right) \Big/ \varepsilon_0 \varepsilon_r \tag{2.8}$$

where h_T is the dielectric thickness, Q_T is the sheet density of surface charge, Q_B is the equivalent sheet density of bulk charge situated at a height h_B above the stationary electrode, and ε_r is the relative dielectric constant. The top and bottom injected charges can be modeled as:

$$Q_T = Q_{T0}\left[1 - \exp\left(-t_{ON} \Big/ \tau_{CT}\right)\right] \exp\left(-t_{OFF} \Big/ \tau_{DT}\right) \tag{2.9}$$

$$Q_B = Q_{B0}\left[1 - \exp\left(-t_{ON} \Big/ \tau_{CB}\right)\right] \exp\left(-t_{OFF} \Big/ \tau_{DB}\right) \tag{2.10}$$

where T and B denote top and bottom, respectively. Q_0 is the steady-state charge. τ_C and τ_D are charging and discharging time constants, respectively. t_{ON} and t_{OFF} are on and off times of the switch, respectively.

Since the surface charge and bulk charge have compensating effects in (2.8), it is not easy to separate their effect by examining the shift in the pull-in voltage. However, they can be separated by analyzing the recovery of the pull-in voltage after stress. Upon removing the applied voltage, the membrane springs back to its suspended position and bulk charging can readily discharge through the stationary electrode, whereas surface charge must discharge either vertically across the entire thickness of the dielectric or laterally across the entire surface of the dielectric. It has been shown that bulk charge discharges in seconds or minutes, whereas surface charge discharges in hours or days [64]. Therefore, surface charging can be quantified by analyzing the pull-in voltage shift after allowing sufficient time (usually ~20 minutes) for the bulk charge to discharge but before any significant amount of surface charge discharges [65]. Figure 2.11 describes the charging and discharging processes in a MEMS switch.

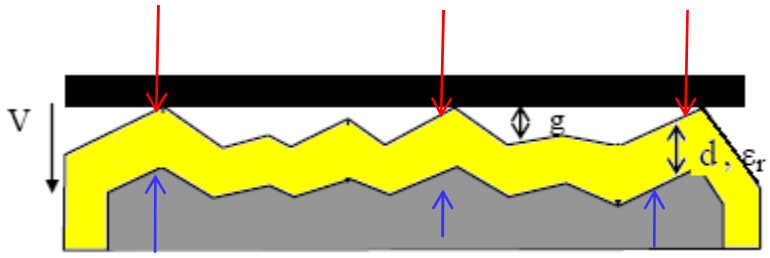

(a)

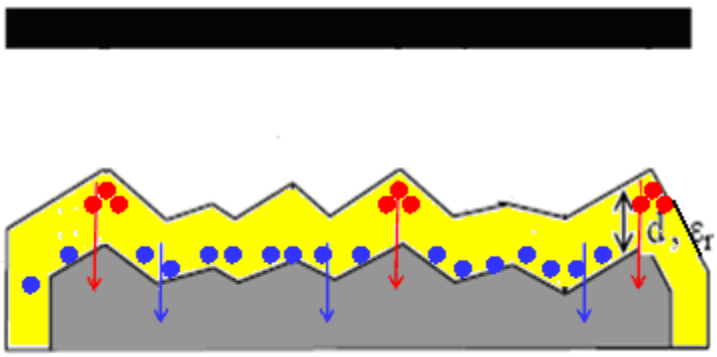

(b)

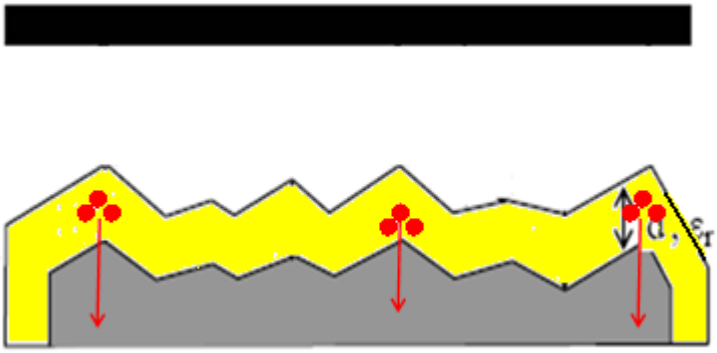

(c)

Figure 2.11. (a) In the down state, charges can be injected either from the asperities of the top (movable) electrode onto the surface of the dielectric, or from the bottom (stationary) electrode into the bulk of the dielectric. (b) Once the applied voltage is removed, the top electrode moves back to its suspended position and the bulk charge readily discharges through the stationary electrode, whereas the surface charge must discharge either vertically across the entire thickness of the dielectric or laterally across the entire surface of the dielectric. (c) After sufficient time (about 20 minutes) all the bulk charge dissipates, but the surface charge remains.

For silicon dioxide switches with an aluminum membrane and chromium/gold bottom electrode [64], it was shown that charge injection from Al into the top of SiO_2 has a higher threshold voltage, faster charging time, and slower discharging time than charge injection from Cr/Au into the bottom of SiO_2 ($\tau_{CT} << \tau_{CB}$, and $\tau_{DT} >> \tau_{DB}$). The higher threshold voltage is attributed to non-ideal contact geometry and surface contamination. The faster charging time is attributed to the exponential voltage dependence [51]. The slower discharging time is attributed to diffusion across SiO_2 as described in Figure 2.11. Top charging saturates at a lower density than the lower electrode ($Q_T << Q_B$). This also can be due to the less than 100% contact area.

It was also found that bulk charging dominates in dry air, while surface charging increases linearly with increasing humidity [66]. In reality, due to the surface roughness of either electrode, surface charge can concentrate around asperities. Such concentration can prevent further charging unless the injected charge is dispersed. In this case, surface conduction can enhance surface charging by allowing the charge to migrate along the surface for a short distance (less than half of the distance between asperities). Following the same rationale, it was proposed that humidity affects surface charging through enhanced surface conduction, which allows for more charge to be injected onto the surface [65]. Moreover, under a typical operating field in the order of MV/cm, switches made of (sputtered) silicon dioxide were shown to be much less susceptible to surface charging than switches made of (PECVD) silicon nitride. Since surface charge discharges very slowly and is detrimental to the lifetime of switches, it is critical to package switches in <1% relative humidity [66].

Finally, charging has been shown to increase with stress time and voltage, but to be independent of switching frequency as long as the switching cycle is much shorter than charging/discharging time constants. This result is true for both unipolar and bipolar charging [52]. The (bottom-injected) steady-state charge density is found to be exponentially dependant on the control voltage and is modeled as:

$$Q^J = Q_0^J \exp\left(V \Big/ V_0^J \right) \tag{2.11}$$

where Q^J is the steady-state charge density for the *Jth* trap, V is the control voltage, and Q^0 and V^0 are fitting parameters.

Therefore, for RF MEMS capacitive switches whose lifetime is limited by dielectric charging, the number of operating cycles is not a universal figure of merit. Duty factor and peak voltage are critical acceleration factors. Therefore, control waveforms with high peak voltage, high duty factor, and low frequency can be used to accelerate failure. On the other hand, control waveforms of low peak voltage, high frequency, and low duty factor may delay failure and result in improved lifetimes. In general, peak voltage, frequency, and duty factor must be specified to allow fair comparison of switch lifetimes.

2.4 Dielectric Materials for Capacitive MEMS Switches

In RF MEMS capacitive switches, a high dielectric constant is favorable for the dielectric material so that a high C_{ON}/C_{OFF} ratio could be achieved. The dielectric should also exhibit low RF losses ($\tan\delta \rightarrow 0$). Several dielectric materials have been investigated so far for use in capacitive MEMS switches. The charging mechanisms in each dielectric will depend mainly on the material structure. Figure 2.12 shows a list of these materials and their corresponding dielectric constants [63], [67-69].

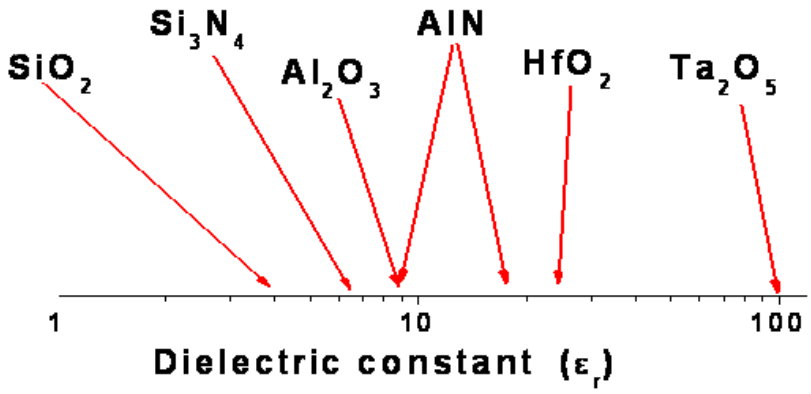

Figure 2.12. List of proposed dielectric materials and their corresponding dielectric constants.

SiO_2 and Si_3N_4 are the most important dielectrics used in modern silicon-based electronic devices. However, the corresponding knowledge gained over five decades of intensive investigation has not yet been effectively applied to MEMS switches. The reason behind this is that in MEMS switches, the dielectric film is deposited on rough metal surfaces and at low temperatures (≤300°C). Therefore, the film surface morphology is affected by the substrate, and the low deposition temperature leads to significant deviation from stoichiometry. The latter allows us to describe silicon dioxide and silicon nitride as SiO_x and and SiN_y with $x<2$ and $y<1.33$. Although these materials consist of covalent bonds, in sub-stoichiometric silicon dioxide the E'_δ defect gives rise to the formation of dipoles by trapping holes [70]. Such effect is also seen in silicon nitride.

Aluminum dioxide (Al_2O_3) has a highly ionic nature [71] and exhibits ionic, dipolar, and space charge polarizations. Crystalline Al_2O_3 (Sapphire) has been shown to exhibit very low charging [63]. Aluminum nitride (AlN) piezoelectric thin film is very popular in RF MEMS micro-machined resonators and filters. Its advantages arise from its high resistivity and piezoelectric coefficient (which is the largest among nitrides), as well as the possibility to be deposited at low temperatures (as low as 500°C) and patterned using conventional photolithographic techniques. AlN consists mainly of ionic bonds and exhibits ionic and space charge polarizations [72]. Theoretical results have indicated that nitride semiconductors possess a large spontaneous polarization [73], associated with which are electrostatic charge densities analogous to those produced by piezoelectric polarization fields. AlN has recently been introduced in MEMS switches [74, 75], and initial reliability tests have proved that under low pull-in bias or certain polarity, the device degradation may be extremely low. Assessment of MIM capacitors with

crystalline AlN dielectric has indicated that this behavior has to be attributed to the presence of a spontaneous polarization arising from dislocations that may induce a surface charge of the order of 6.6×10^{-7} C/cm^2, which is much smaller than the theoretically predicted spontaneous polarization [75].

Hafnium dioxide (HfO_2) and Tantalum Pentoxide (Ta_2O_5) consist mostly of ionic bonds as well [76, 77] and show high levels of charging. Taking all these into account, we can conclude that the charging mechanisms taking place in insulating films used in MEMS capacitive switches can be summarized in Table 2.1.

Table 2.1.
Charging Mechanisms in Insulating Films.

Material	Ionic	Dipolar	Space Charge
SiO_2	-	(X)	X
Si_3N_4	-	(X)	X
Al_2O_3	X	X	X
AlN	X	X	X
HfO_2	X	X	X
Ta_2O_5	X	X	X

(X) Due to deviation from stoichiometry

Silicon dioxide (SiO_2) and silicon nitride (Si_3N_4) are the most well-known materials for MEMS applications and will be investigated in this work.

2.5 Methods Currently in Use to Characterize Charging

The dielectric film used in MEMS switches is usually low-temperature deposited silicon nitride or silicon dioxide, containing a high density (10^{18} /cm^3) of traps associated with dangling bonds [39], [40]. These traps are amphoteric in nature, so they can be negatively or positively charged. Under high electric fields, charges can get injected into

the dielectric and become trapped in the bonds. Further, due to the insulating nature of the silicon dioxide or silicon nitride films, the recovery time can take anywhere between a few seconds to several days or even months.

Developing a good analytical model that would describe accumulating of charges in the dielectric and their influence on the device behavior is the main step to achieving more reliable switches. Presently, available models assume that dielectric charging arises from charges distributed throughout the dielectric material [41], the presence of charges at the dielectric interface [78] and areas under compressive or tensile stress [79], as well as injection of charges from the suspended bridge during the on-state [54, 80].

So far the lifetime of MEMS switches, hence the process of dielectric charging has been investigated by recording the shifts of pull-in and pull-out voltages [42, 51] and RF transmission characteristics [8] as a function of electrical stress conditions. Complementary assessment methods, such as recording the transient current in permanently on switches and MIM (metal-insulator-metal) capacitors [81-85], recording the transient response of the on-state capacitance in MEMS switches [86, 87], and the employment of both MIM capacitors and MEMS switches [88], [89] were subsequently introduced. Electrostatic and adhesion forces have been studied as well [50]. Finally, a process arising from contact-less charging and related to the dielectric intrinsic polarization processes was reported [90, 91]. These studies, specifically monitoring the C-V (capacitance–voltage) characteristics in MEMS switches [38], [43-45], [54], [86, 87], [92] and I-V (current–voltage) characteristics in MIM capacitors [52], [81], [85], [93, 94] have led to an increasing level of physical understanding. For example, qualitative and quantitative models were developed to explain charging in MEMS

switches, charging and discharging current time constants were determined, and the activation energies of thermally activated charging mechanisms were calculated [86], [88]. Material quality was found to have strong effects on discharging current [85] and depolarization current [95].

It was also acknowledged that in thick dielectrics, the main electronic processes that lead to dielectric charging are: (1) the Trap-Assisted-Tunneling (TAT) of electrons from the electrode to unoccupied defect or trap states in the dielectric close to the electrode-dielectric interface (contributing to the transient current), and (2) the time-dependent component of Poole-Frenkel (PF) movement of trapped electrons from the defect levels to the conduction band of the dielectric (contributing to both transient and steady-state currents) [96]. Therefore, at any given time, the total current in the dielectric can be written as the sum of the TAT and PF currents:

$$j(t) = j_{TAT}(t) + j_{TPF}(t) \tag{2.12}$$

In spite of all these research efforts, several issues remain yet to be solved. For example, the exact mechanisms for the transfer and trapping of charge are not known, although the effects are measureable. Specifically, the mechanisms responsible for charge injection during the switch pull-down state which are responsible for dielectric charging have not been entirely understood.

The current work tries to address these issues in silicon nitride and silicon dioxide MEMS switches. Chapter 3 discusses dielectric charging effects in capacitive MEMS switches with silicon nitride. The effects of changing the deposition temperature, dielectric thickness, and stoichiometry of the PECVD silicon nitride film are examined in

detail. Both MEMS switches and MIM capacitors are fabricated, and their charging behaviors are analyzed and compared. Several tools are employed to characterize the silicon nitride films. The main objective of this work is to get a better understanding of the effects of stoichiometry on the charging of PECVD silicon nitride films. This insight can then be employed to diminish dielectric charging effects in MEMS capacitive switches with silicon nitride.

Chapter 4 discusses dielectric charging effects in MEMS capacitive switches with silicon dioxide. The effects of employing different activation mechanisms and varying the amount of electric stress are examined. Finally, the effects of applying a "constant" long-time electric stress on the switch are studied. A general model of distributed charge and air gap is adopted and further developed to better explain the charging behavior of MEMS switches. The main objective of this part is to provide a deeper insight into the trapping processes in dielectric materials and their corresponding time constants.

The thesis is concluded in Chapter 5. In this chapter, the contributions of this work are summarized and possible directions for future work are discussed. A list of publications to date is provided in Chapter 6.

CHAPTER 3

DIELECTRIC CHARGING IN CAPACITIVE RF MEMS SWITCHES WITH SILICON NITRIDE

3.1 The Effect of Deposition Temperature

This part of our work investigates the charging mechanisms of silicon nitride films used in capacitive RF MEMS switches in order to identify the most dominant one. We studied silicon nitride films deposited at two different temperatures. The charging investigation of the switches was based on observing the dependence of the capacitance-voltage (C-V) characteristic on both the bias sweep width and temperature. The latter is used to determine the Trap-Assisted-Tunneling (TAT) activation energy of the Poole-Frenkel (PF) potential barrier in order to understand its relation to the dielectric material stoichiometry. We then studied MIM capacitors with silicon nitride films as their dielectric and compared their charging mechanisms with the MEMS switches. The charging study on the MIM capacitors was done by measuring the TSDC (thermally stimulated depolarization current) spectra. In addition, we obtained detailed information on the stoichiometry of silicon nitride films using XPS and stress measurements. A relationship between the deposition temperature and the silicon nitride stoichiometry was derived for the first time. Consistent measurement results provided new insight into the charging mechanisms of silicon nitride and its dependence on the deposition temperature of the material [97, 98].

3.1.1 Theoretical Background: Charging Mechanisms

In principle, TAT is determined by the spatial and energetic distribution of trap states, the offset between the Fermi energy of the electrode and the conduction band of the dielectric, and the lower limit of the tunneling relaxation times. The temperature dependence of TAT is controlled primarily by the energy distribution of the traps, and the frequency dependence is controlled by their spatial distribution. Traps distributed uniformly in both energy and space result in an essentially temperature-independent mechanism. The step-response currents for the tunneling mechanism exhibit an inverse dependence on sample thickness, which becomes nonlinear at high applied electric fields, and the detailed behavior is very sensitive to the trap distribution assumed. For a particular trap distribution, it is possible to have a polarity-dependent irreversible step response [86, 87], [89], [96].

An expression was derived in [86], [96] for the time-dependent current, assuming that TAT is the only operating mechanism:

$$j_{TAT}(t) = q \int_{x=0}^{\infty} \int_{E=-\infty}^{-qFx} N^{ff}(x, E+qFx) \cdot (f_{\infty} - f_0) \cdot \frac{e^{-t/\tau}}{\tau} \cdot \frac{x}{L} dE \cdot dx \tag{3.1}$$

where the current flows in the x direction, L is the sample thickness, N^{ff} is the field free trap distribution, E is the energy, F is the electric field intensity, f_{∞} and f_0 are the Fermi functions defined as

$$f_{\infty}(E) = \{1 + \exp[(E - E_F)/kT]\}^{-1} \tag{3.2}$$

$$f_0(E) = \{1 + \exp[(E + qFx - E_F)/kT]\}^{-1} \tag{3.3}$$

and $\tau = \tau_0 e^{2K_0 x}$, and $K_0 = \frac{\sqrt{2m|E|}}{h}$, where m, $\hbar$, k, T, and E_F are the electronic mass, Planck's constant, Boltzmann's constant, temperature, and Fermi energy of the metal electrode respectively. Therefore, according to (3.1), the electron tunneling efficiency is determined by the distribution of states in the gap of the dielectric material, the distance from the interface, and the intensity of the electric field.

The PF mechanism is driven by the electric field, which reduces the barrier height on one side of the trap, thereby increasing the probability of the electron escaping from the trap. As the electric field increases, the potential barrier decreases on the right side of the trap, making it easier for the electron to vacate the trap by thermal emission and enter the quasi-conduction band of the host material. A first-order model for the current due to the PF effect assumes that each trapping center is independent of the other centers, i.e., the potentials do not overlap. This assumption is valid only if the impurity density is low. Although in amorphous materials the impurities density is usually not very low, this model is generally used for the purpose of simplicity. This procedure implicitly assumes just an effective potential barrier Φ_{PF}.

The transient component of PF conduction was derived in [86], [96], assuming that a certain fraction of the trapped electrons is lost to Poole-Frenkel emission (thermal emission of electrons from the trap states to the conduction band of the dielectric [89]). The Poole-Frenkel current density is given by a simple drift equation $q\mu F\rho$, where μ and ρ are the electronic mobility in the dielectric and carrier density (per unit area of the

dielectric) that participate in the Poole-Frenkel process, respectively. Since there is a distribution of trap states, the transient component of Poole-Frenkel current density (arising from charge redistribution) was defined as

$$j_{TPF}(t) = q\mu F \int_{x=0}^{\infty} \int_{E=-\infty}^{-qFx} \exp\left\{-\frac{q}{kT}\left(E - \sqrt{\frac{qF}{\pi\varepsilon_{opt}}}\right)\right\} \cdot n(x,E,t) \cdot dE \cdot dx \tag{3.4}$$

where ε_{opt} is the high-frequency dielectric constant, and n is the density of trapped electrons at a depth E from the conduction band. Here, it must be pointed out that at any given time, the PF process alters the trapped distribution of electrons, which in turn alters the TAT process at subsequent times. Furthermore, materials with higher dielectric constants will be less sensitive to the field-induced trap barrier lowering inherent in the PF effect.

3.1.2 RF MEMS Switches

Figure 3.1 shows the capacitance-voltage (C-V) characteristic of the silicon nitride MEMS switches used in this part. C-V characteristics directly characterize the up and down state capacitances, indicating the insertion loss and isolation characteristics of the RF MEMS switch. Initially, under a positive swing of control voltage, the switch pulls in at V_{PI}^{+}=10 *V*. The control voltage is then gradually decreased, causing the switch to pull out at V_{PO}^{+}=4 *V*. During a negative swing of the control voltage, $V_{PI}^{-} \approx V_{PI}^{+}$ and $V_{PO}^{-} \approx V_{PO}^{+}$. Thus another loop is formed at the left side of the zero axis that mirrors the right loop. The symmetry of the two loops about *V*=0 indicates little charging to begin with.

The minimum of the capacitance-voltage characteristic (Figure 3.1) occurs when the electrostatic force is at its lowest value. The bias value for the minimum capacitance (V_m) is proportional to the charge stored in the dielectric and/or on the dielectric surface:

$$V_m = -\frac{\sigma \cdot d}{\varepsilon_r \varepsilon_0} \tag{3.5}$$

where d is the dielectric film thickness. Assuming the presence of a background charge of σ_0 introduced during fabrication and/or handling, the total stored charge in the dielectric will be determined by the charge injected from the contacting electrode (j_{TAT}), and the charge transported from the dielectric surface (j_{TPF}). The charge polarity will be determined by the polarity of the contacting electrode. The total stored charge can be written as:

$$\sigma = \sigma_0 + \int_0^{t_0} \left[j_{TAT}(t) + j_{TPF}(t) \right] \cdot dt \tag{3.6}$$

where the switch is placed in the pull-down state at $t=0$, and the charge is measured at $t=t_0$.

Taking these into account, it is evident that the charging mechanism can be determined by monitoring the shift of V_m with either temperature or the bias voltage in the pull-down state.

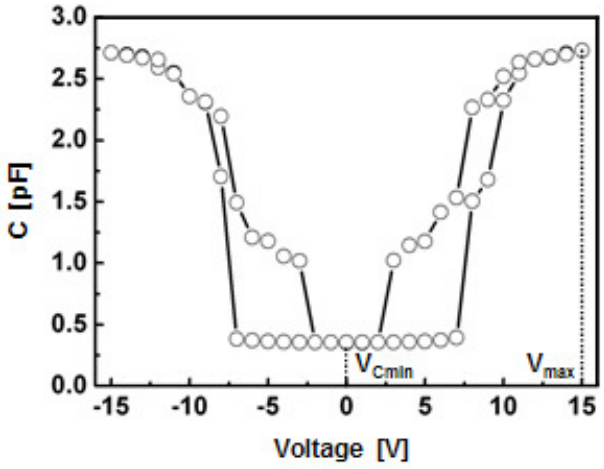

Figure 3.1. The capacitance-voltage characteristic of the capacitive RF MEMS switch with silicon nitride as its dielectric layer.

3.1.3 Experimental Analysis

The switches utilized in the present experiment were fabricated with a standard photolithographic process on high resistivity silicon wafers (ρ>10kΩ-cm). The dielectric film is silicon nitride deposited using plasma enhanced chemical vapor deposition (PECVD) method at 100°C to 300°C in 100°C increments. The stoichiometry of the dielectric film was determined using X-Ray Photoelectron Spectroscopy (XPS) and its internal stress using both profilometry and 3D laser methods. The dielectric film is 200 nm thick in all cases. This thickness is generally chosen as a regular dielectric thickness for RF MEMS switches. The beam is an evaporated titanium-gold seed layer electroplated to a thickness of 2 μm. Under no applied force, the beam is suspended about 2 μm above the dielectric. The sacrificial layer was removed with photo-resist stripper and the switches were dried using a CO_2 critical point dryer. The detailed recipe for MEMS switch fabrication is given in Appendix A. Figure 3.2 shows the top view of the capacitive RF MEMS switch used in this work.

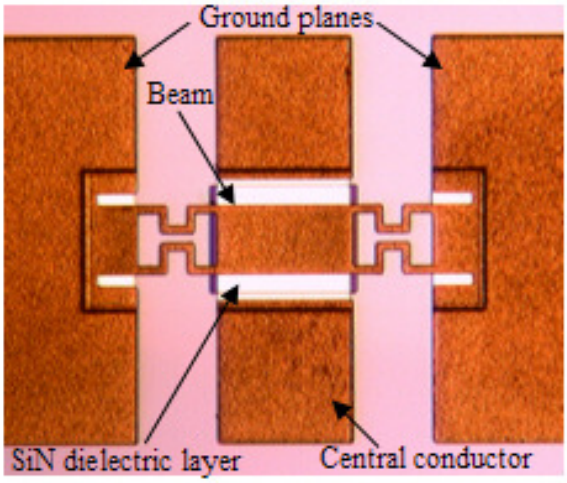

Figure 3.2. Top view of the capacitive RF MEMS switch used in this study.

Capacitance-voltage (C-V) characteristics of the RF MEMS switches were assessed. The capacitance was monitored with a Boonton 72B capacitance meter while sweeping the voltage in 0.5 V steps in the temperature range of 300K to 450K. This temperature range was selected taking into account the charge kinetics as revealed from previous measurements [99]. The sweep rate for the C-V measurements was fast enough (224 mV/s) to prevent charging of the switches during each assessment.

MIM capacitors were fabricated in an analogous way to the MEMS switches (the deposition method for each layer and the thickness of each layer was kept exactly the same for MEMS switches and MIM capacitors). Their charging mechanisms were then compared with the MEMS switches to gain a better understanding of dielectric charging in silicon nitride dielectric films. The silicon nitride is deposited using the PECVD method at 100°C to 300°C in 50°C increments. The dielectric film is 200 nm thick in all cases. The dielectric surface roughness was measured with a Tencor P15 surface profiler and found to be less than 2 nm when deposited on an evaporated thin film. The top view of an MIM capacitor used in this work is shown in Figure 3.3. Table 3 lists the different

MIM layer structures. MIM capacitors with both symmetrical and asymmetrical metallic contacts were fabricated to examine the effect of metallic contacts.

The charging process in MIM capacitors was investigated by measuring the TSDC spectra. This also allows the calculation of stored charge. TSDC is a non-isothermal method used to characterize charging in MIM capacitors. Depolarization processes are monitored while varying the temperature. At low temperatures, any dipolar or space charge motions are hindered and charging or discharging currents of the ordinary dielectric capacitor are recorded. At higher temperatures however, dipolar and space charge motions can occur. The corresponding polarization/depolarization currents dominate.

The TSDC spectra were measured with a Keithley 6487 voltage source pico-ampere meter in the temperature range of 200K to 500K. The capacitive and leakage currents were suppressed in the measurement path with well-guarded probes and probe station. Therefore the measurement range for transient currents was in the pico-ampere level. A constant electric field of 1 MV/cm was applied to all samples. Finally, the heating rate was β=2.5 K/min.

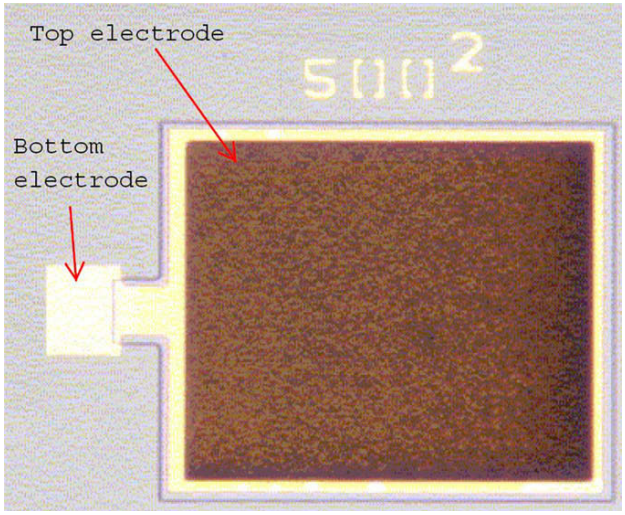

Figure 3.3. Top view of an MIM capacitor. Top and bottom contacts are indicated.

Table 3.1.
MIM Layer Structure.

Layer	**Symmetric**	**Asymmetric**
Au	200 nm	200 nm
Ti	20 nm	20 nm
Si_3N_4	200 nm (100°C to 300°C)	200 nm (100°C to 300°C)
Ti	20 nm	-
Au	200 nm	200 nm
Ti	20 nm	20 nm
SiO_2 (optional)	3 µm	3 µm
Si	500 µm	500 µm

3.1.4 Silicon Nitride Characterization and MIM Capacitors Discussion

Figure 3.4 and Figure 3.5 show the dependence of the silicon nitride film stoichiometry and stress on the deposition temperature. The increase of the deposition temperature clearly causes the nitrogen content to increase. It is known that low-temperature silicon nitride is non-homogeneous, consisting of amorphous silicon clusters [100, 101] among areas with various compositions of silicon nitride. We therefore conclude that by increasing the deposition temperature the average band gap of the film also increases.

On the other hand, the increase of temperature leads to an increase in the stress, beginning from compressive stress for films deposited at 100°C to tensile when the deposition was performed at 300°C. The change of stress is expected to affect the material electrical properties [102]. This can be observed in the calculated stored charge. The stored charge is calculated by integrating the TSDC (thermally stimulated depolarization current) spectra obtained from MIM capacitors over the whole temperature range.

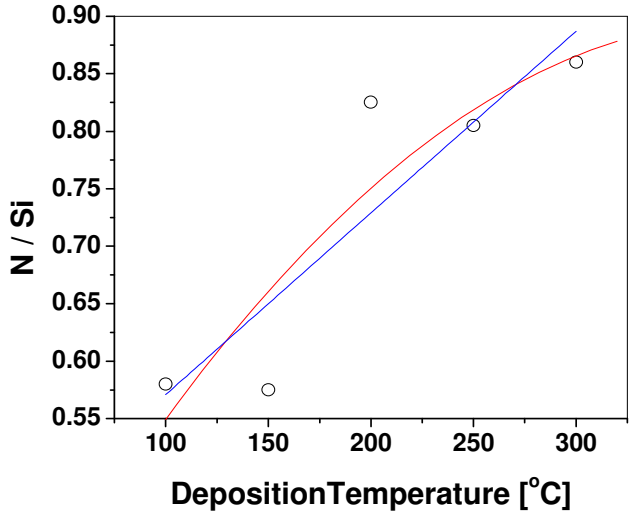

Figure 3.4. N/Si ratio for 200 nm silicon nitride on high resistivity silicon. The straight line was drawn to show the stoichiometry trend.

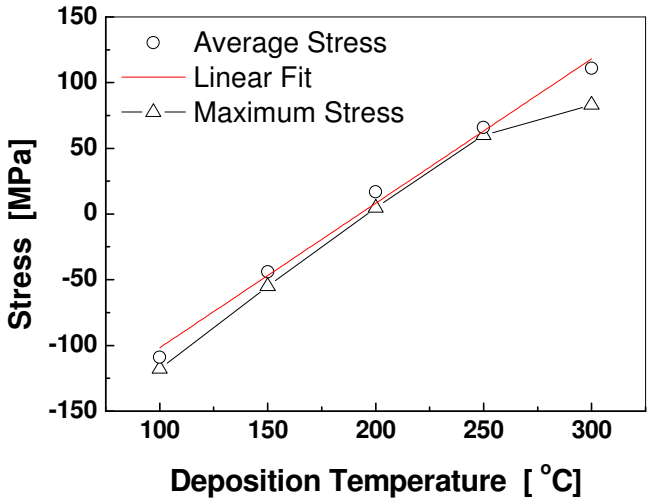

Figure 3.5. Film stress for 200 nm silicon nitride deposited on silicon. The linear fit was performed to show the average stress trend.

In insulators, the time and temperature dependence of polarization and depolarization processes, in the case of dipolar polarization, are determined by the

competition between the orienting action of the electric field and the randomizing action of thermal motion. The depolarization process in a MIM capacitor will induce a short circuit discharge current transient (DCT) that is given by

$$I_{dis}(t) = -\frac{dP(t)}{dt} = \frac{P(t)}{\tau} \tag{3.7}$$

Moreover, the current density produced by the progressive decrease in polarization in the course of the TSDC experiment, where time and temperature are simultaneously varied, is approximated by

$$J_D(T) = \frac{P_S(T_P)}{\eta_0}.\exp(-\frac{E_A}{kT}).\exp[-\frac{1}{\beta\tau_0}.\frac{kT^2}{E_A}.\exp(-\frac{E_A}{kT})] \tag{3.8}$$

where β is the heating rate (K/sec), E_A is the depolarization mechanism activation energy, $P_S(T_P)$ is the equilibrium polarization at the polarizing temperature T_P, and τ_0 is the corresponding infinite temperature relaxation time.

In the case of space charge polarization induced by charge injection, the processes leading to thermally stimulated depolarization currents are far more complex because several mechanisms, such as the counteracting action of diffusion, the loss of migrating carriers due to recombination, the blocking effect of the electrode-dielectric interfaces, the charge trapping, and the influence of local electric fields can be involved simultaneously. Under these circumstances the TSDC spectra show the characteristic properties of distributed processes, such as extension over a wide temperature range. In addition, only a part of the space charge decay is monitored in the MIM capacitors' current as a consequence of the partial dissipation of excess charges by space-independent intrinsic conductivity, the incomplete release of the image charges induced

at the electrodes, and the dependence of the diffusion released current on the blocking character of the electrodes [103].

The method proposed by C. Bucci and R. Fieschi [63] was used throughout our work to measure the TSDC spectra in MIM capacitors. This is explained in Figure 3.6. First, the dielectric is heated to a high temperature of T_P (usually 500K). At this temperature, a polarizing electric field (E_P) is applied to the dielectric for time duration of t_p ($t_P >> \tau$ (T_P) so that the dipoles would polarize to "saturation"). Then the dielectric is cooled to a temperature of T_0 (usually 200K) and the electric field is removed. At this point, the dielectric is heated at a constant rate (up to 500K) and the depolarization currents are monitored.

Figure 3.7 shows this setup for an MIM capacitor. When the switch is in position "A", an electric field (E_P) is applied. When the switch is moved to position "B", the depolarization currents are collected.

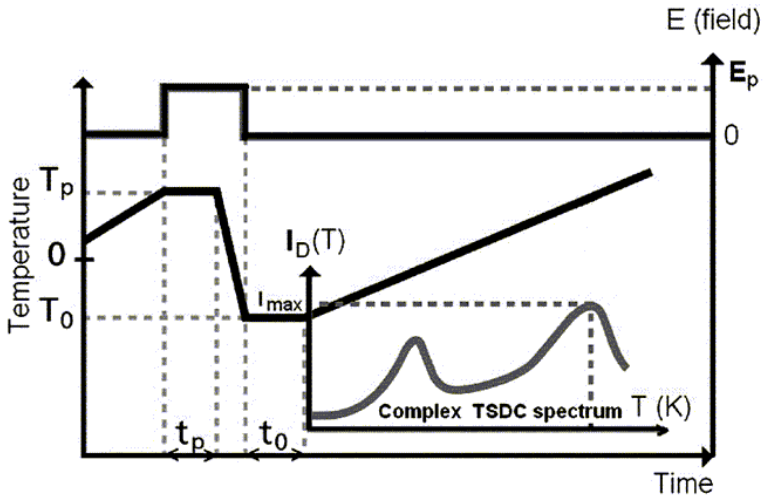

Figure 3.6. C. Bucci and R. Fieschi method for measuring the TSDC spectra in MIM capacitors.

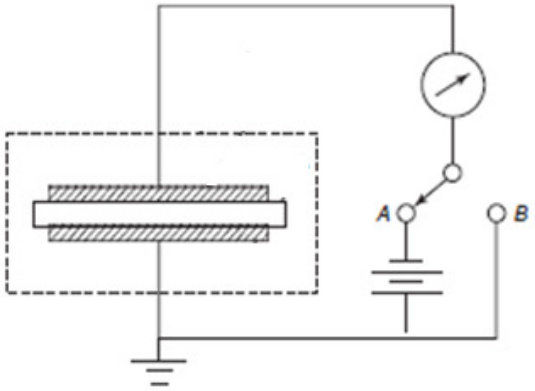

Figure 3.7. TSDC measurements for an MIM capacitor.

The TSDC spectra for the MIM capacitors with silicon nitride deposited at three different temperatures are shown in Figure 3.8. The application of (3.8) allows partial analysis of the spectrum at temperatures above 300K. At lower temperatures, the spectrum cannot be analyzed, and this behavior has to be attributed to charging induced by injected charges.

The TSDC spectra show that in the low-temperature region, below 300K, the depolarization current is larger (due to a larger amount of stored charge) when the silicon nitride film deposition temperature increases. In the high-temperature range, above 300K, the TSDC current increases as the temperature is increased, with a practically constant activation energy of about 0.22 eV, independent of the film deposition temperature. The TSDC current above room temperature can be described by

$$I_{TSDC} = I_1 + I_0 . \exp(-\frac{E_A}{kT}) \tag{3.9}$$

As suggested earlier, the TSDC spectrum allows the calculation of stored charge as follows

$$\sigma = \frac{1}{\beta A}\int_{T_1}^{T_2} I_{TSDC}(T)dT \tag{3.10}$$

where A is the capacitor area. This integration can be performed since temperature is varying linearly with time as

$$T(t) = T_0 + \beta.t \tag{3.11}$$

Therefore, integrating the currents in the temperature domain would provide a result proportional to the result of integrating in time domain.

The dependence of stored charge on silicon nitride film deposition temperature is presented in Figure 3.9. In this Figure, the integration of (3.10) is performed from 200K to 500K for all materials. It is seen that the stored charge increases with the deposition temperature. This increasing trend is in good agreement with previously reported results [104]. The increase of stored charge can be related to the increase of material nitrogen content and hence the band gap. Here, we should point out that presently there is no report on the dependence of silicon nitride charge trap properties on the material stoichiometry and band gap.

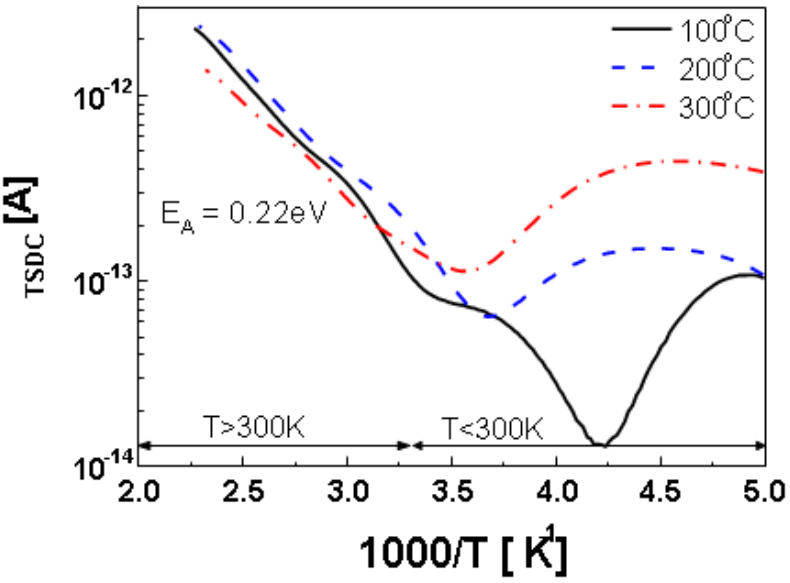

Figure 3.8. Dependence of TSDC spectra on the silicon nitride film deposition temperature.

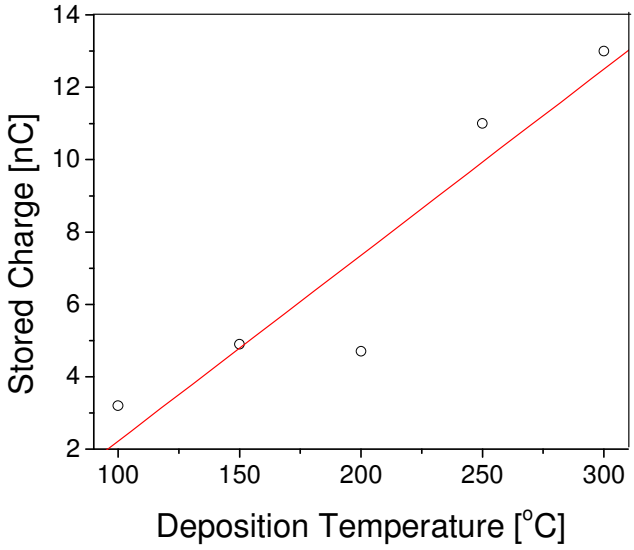

Figure 3.9. Dependence of stored charge on the silicon nitride film deposition temperature.

3.1.5 RF MEMS Results and Discussion

Figure 3.10 shows the dependence of the bias voltage at which the minimum capacitance occurs (V_m) on the maximum amplitude of the applied bias (V_{max}) for the capacitance-voltage characteristic measurements. The data was obtained at 300K (Figure 3.10a) and 340K (Figure 3.10b) from a switch with 200 nm silicon nitride film deposited at 250°C. The pull-in voltage was about 10 V. The switches were unpackaged and the measurement was performed at 25% humidity conditions.

To determine the charging mechanism and simplify the analysis, we assumed that the Poole-Frenkel effect is dominant [105]. Then, (3.5) and (3.6) result in

$$V_m = V_{\max} \cdot \exp\left(\frac{B\sqrt{V_{\max}} - \Phi_{PF}}{kT}\right) + V_0 \tag{3.12}$$

where B, V_{max}, Φ_{PF}, are fitting parameters and V_0 is the voltage corresponding to σ_0. The pre-exponential parameter V_{max} corresponds to a maximum variation of bias shift due to charge trapping in thermally activated traps and is expected to relate to the trap concentration through an equation analogous to (3.5). Such a behavior is expected in disordered materials with a continuous distribution of defects [106].

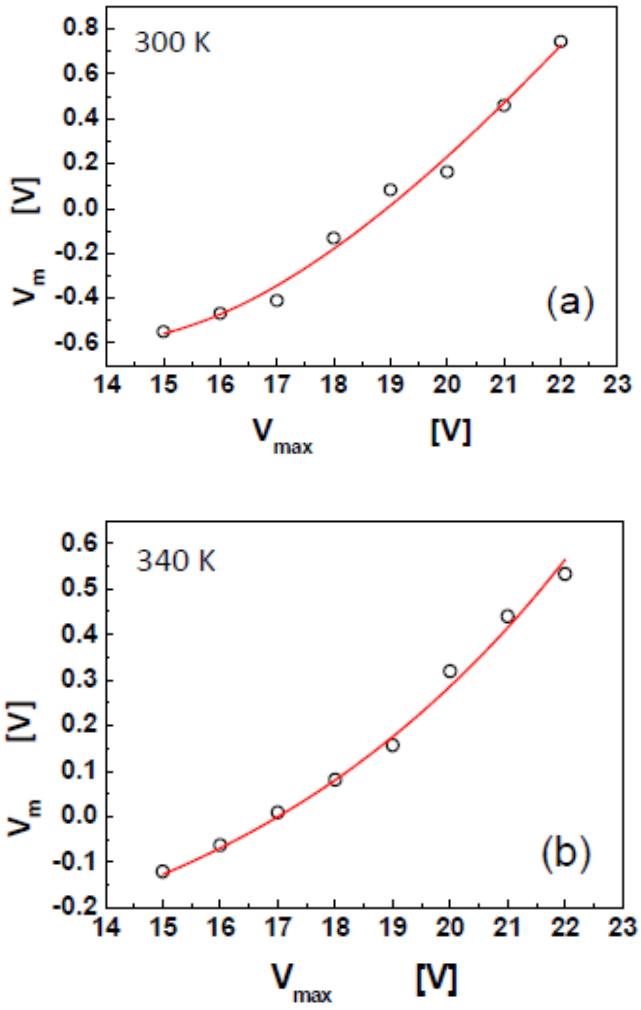

Figure 3.10. Dependence of the bias voltage at which the minimum capacitance occurs (V_m) on the maximum amplitude of the applied bias (V_{max}) for (a) 300K and (b) 340K.

The apparent excellent fit in Figure 3.10 requires further investigation since it is well known that the conductivity of thin metal–semiconductor–metal structures containing hydrogenated amorphous silicon alloys can be affected by the current stressing conditions [107]. This phenomenon is attributed to the formation of a meta-stable defect band through which carriers can move by hopping between charged states in a manner similar to the Poole-Frenkel effect, the driving force for defect creation being

the energy released during hole-electron recombination in the bulk of the device. For a small number of defects, a classical PF behavior is observed over many orders of current. In the case of disordered materials, including those with carriers hopping between neutral defect states in band tails, the charging process is expected to deviate from the Poole-Frenkel effect and is better represented by (3.6), while macroscopically being better described by (3.12).

The main reason for observing a bigger change at 300K compared to 340K in Figure 3.10 is that trapping/de-trapping kinetics increase with temperature. The characteristic time constant is given by the Arrhenius law

$$\tau(t) = \tau_0 . \exp\left(\frac{E_A}{kT}\right) \tag{3.13}$$

where τ_0 is the time constant at infinite temperature. This relationship clearly indicates that during the off time, which is determined by the C-V curve measurement process and not the temperature, the de-trapped charge is larger when experiments take place at higher temperatures. This will lead to a smaller change in V_m excursion at higher temperatures.

The temperature dependence of V_m at V_{max}=15V is presented in Figure 3.11 for switches where the 200 nm silicon nitride film has been deposited at 150°C and 250°C. In both figures, the fitting using (3.12) indicates thermally activated mechanisms (the derived activation energy values represent the numerator of the exponent):

$$V_m = V_0 + V_1 . \exp(-\frac{E_A}{kT}) \tag{3.14}$$

The activation energy is higher in the 150°C silicon nitride, which shows a smaller V_m change over temperature. This observed difference may be attributed to a change of Φ_{PF} due to different material electrical properties. Taking into account that both the silicon nitride stoichiometry and its hydrogen content are affected by the deposition conditions, the former was determined from XPS assessment, which showed that in the 150°C silicon nitride the stoichiometry is N/Si≅ 0.57, while the stoichiometry is N/Si≅0.80 in the 250°C one. This clearly shows that the silicon content is larger in the low-temperature material, which leads to the conclusion that the band gap is larger in the 250°C silicon nitride than in the 150°C one. Taking into account the expected formation of meta-stable defect bands [107-109] during high electric field stresses and the dependence of material band gap on the deposition method, it becomes clear that the activation energy is related to the dielectric film band gap. This conclusion, although seeming to support the results obtained from the Poole-Frenkel effect and the low charging reported in low temperature silicon nitride MIM capacitors [110], requires further and in depth investigation for better understanding the charging process in MEMS capacitive switches.

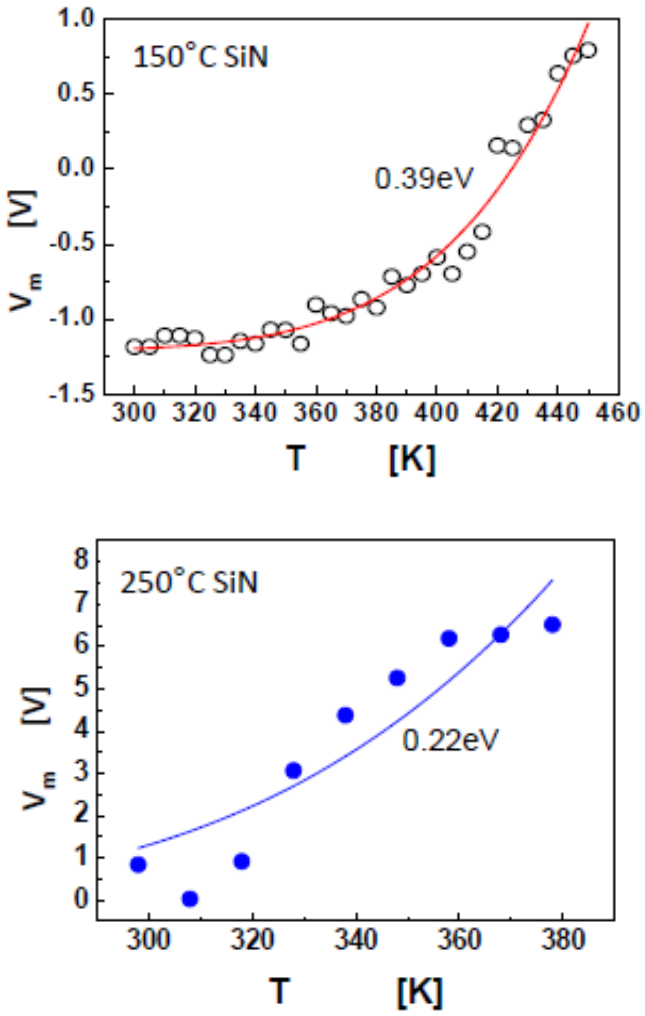

Figure 3.11. Temperature dependence of V_m in switches. The silicon nitride film was deposited at (a) 150°C and (b) 250°C.

Finally, it is seen that under the same conditions, the 250°C silicon nitride material suffers more from dielectric charging effects than the 150°C material. This is understood from calculating the integral of the TSDC spectra over temperature for the MIM capacitors, and from observing the shift of the V_m values with temperature for the MEMS switches. Different activation energies were obtained for the MEMS switches

with 150°C and 250°C silicon nitride materials. This difference (Figure 3.11) may be attributed to different materials' band gaps and band potential fluctuations.

Since to the best of our knowledge there is currently no clear information on the dependence of these parameters on silicon nitride deposition conditions, this is the first work on understanding these properties of silicon nitride.

3.1.6 The Effect of Humidity

This results presented here were obtained in atmosphere with 25% humidity conditions. Although recent experiments have demonstrated that dielectric charging can be aggravated by humidity [66], the way it affects dielectric charging has not yet been fully clarified. Recently, the effect of humidity on dielectric charging was investigated with the Kelvin force microscopy method [111]. It was demonstrated that injected charge distribution is narrower in dry nitrogen ambient and wider in normal atmosphere. It was also found that the decay time constant (which depends on the insulator bulk properties since the charges are collected by the bottom electrode) increases by almost four orders of magnitude in nitrogen ambient. Finally, it must be pointed out that no lateral diffusion was observed in any of these experiments.

Regarding the present work, it is clear that the experimental results in MIM capacitors are not affected by humidity. In the case of MEMS switches, although humidity is expected to affect dielectric charging, it is still not possible to correlate the effect of humidity with the results that arise from different stoichiometry and deposition conditions.

3.1.7 Summary

In this section, the mechanisms responsible for dielectric charging of capacitive RF MEMS switches were investigated. The investigation included films of silicon nitride deposited under different substrate temperature conditions. The stoichiometry of each silicon nitride film was carefully determined by XPS measurements. Stress values were also measured for all films, using both profilometry (2D) and laser (3D) methods. These measurements allowed for obtaining a direct relationship between the deposition temperature and material properties (i.e., stress and stoichiometry). It was seen that lower-temperature silicon nitride has less stress and is richer in the silicon component, which results in an increase of the average band-gap with temperature increase.

Both RF MEMS switches and MIM capacitors were fabricated using the characterized silicon nitride films. Their charging processes were monitored and compared to gain a better understanding of the mechanisms responsible for charging in the silicon nitride films. The comparison of the V_m plots obtained from RF MEMS measurements clearly indicated that the lower-temperature PECVD silicon nitride is less prone to dielectric charging than the higher-temperature one. TSDC spectra of the MIM capacitors and the calculated stored charge showed consistent results with the MEMS switches.

Different activation energies were obtained for the 150°C and 250°C silicon nitride MEMS switches. This difference (Figure 3.11) may be attributed to different materials' band gaps and band potential fluctuations. Finally, it was seen that charging in silicon nitride is caused by the formation of a meta-stable defect band where carriers can

move by hopping between charged states in a manner similar to the PF effect. The formation of this band seems to contribute to the dielectric charging of silicon nitride.

3.2 The Effect of Dielectric Film Thickness

To better understand and compare the charging mechanisms in silicon nitride films deposited at different temperatures, we also changed the thickness of the dielectric layer in MIM capacitors and MEMS switches with silicon nitride deposited at 150°C and 250°C. The thickness was changed from 100 nm to 600 nm in increments of 100 nm.

3.2.1 The Effect of Film Thickness in MIM Capacitors

Figure 3.12 shows the TSDC spectra for MIM capacitors with three different thicknesses of silicon nitride deposited at 150°C. A higher value for the TSDC current is observed in thicker dielectrics. The fitting of (3.9) to the experimental data of the 600 nm MIM capacitor above room temperature (300K) reveals activation energy of 0.24 eV. I_1 and I_0 current levels were both found to have a value 3.1×10^{-13} A. The activation energy is seen to be the same for all samples independent of the dielectric thickness.

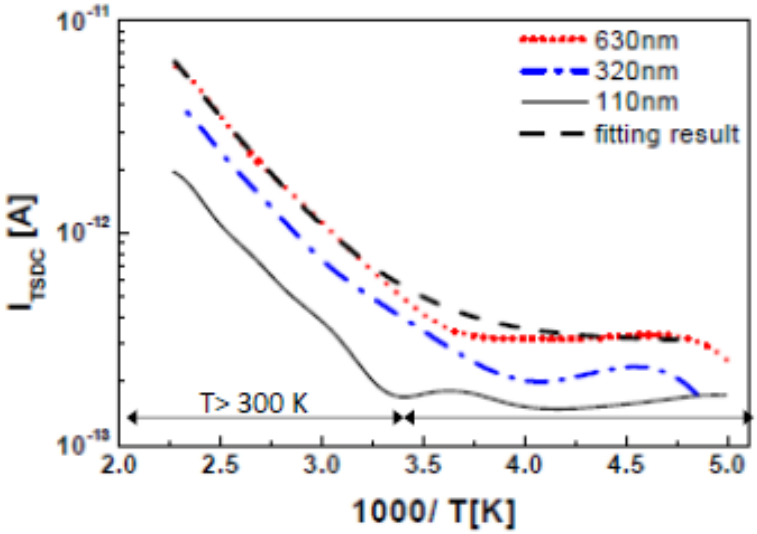

Figure 3.12. Dependence of TSDC spectra on dielectric film thickness for MIM capacitors with silicon nitride deposited at 150°C.

As described in (3.10), the stored charge can be calculated by integrating the TSDC spectra over temperature. Substituting (3.9) for I_{TSDC} in (3.10), we obtain:

$$\sigma = \sigma_1 + \sigma_0 . \exp(-\frac{E_A}{kT}) \tag{3.15}$$

where E_A is the TSDC current envelope activation energy. Figure 3.13 shows the stored charge versus temperature for an MIM capacitor with silicon nitride deposited at 150°C. The dielectric thickness is 200 nm. Two mechanisms are detected. The first one occurs at high temperatures (T>330K) with an activation energy of about 0.24 eV. This activation energy is the same as the one discussed before for the TSDC spectra above 300K (Figure 3.12). The second mechanism is seen at low temperatures (T<330K) with an activation energy of about 0.10 eV.

Similar activation energies were found for MIM capacitors of all thicknesses (although the value of stored charge at each temperature is higher for thicker dielectrics,

as expected from the TSDC spectra in Figure 3.12). This indicates that the main trapping mechanisms have the same origin. This common behavior, which is independent of the dielectric film thickness, leads us to the conclusion that it can be included in the modeling tools of dielectric charging.

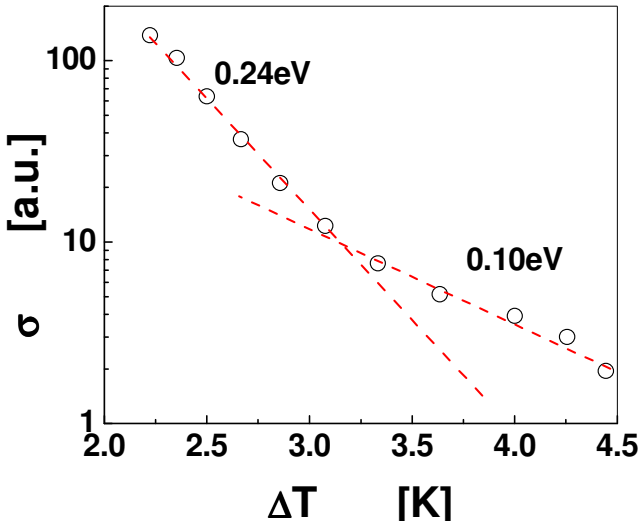

Figure 3.13. Dependence of the stored charge on the TSDC measurement temperature. The silicon nitride was deposited at 150°C and is 200 nm thick.

Figure 3.14 shows the calculated stored charge in the MIM structures for different thicknesses of silicon nitride. Both 150°C and 250°C MIM capacitors are shown in this Figure. The stored charge was calculated using (3.10), by integrating the TSDC spectra from 200K to 500K.

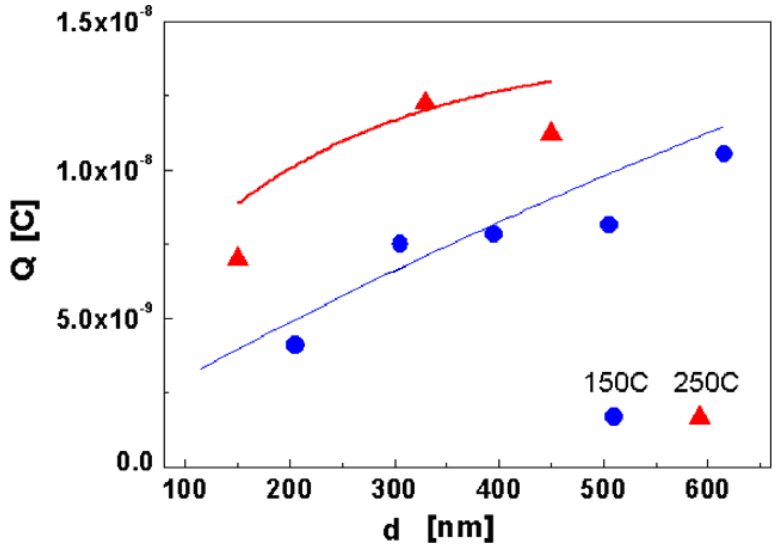

Figure 3.14. Dependence of the stored charge on dielectric film thickness for 150°C (circles) and 250°C (triangles) silicon nitride.

Figure 3.14 shows that for both 150°C and 250°C materials, the stored charge increases with the dielectric film thickness. The stored charge is larger in the high-temperature (250°C) material than in the low-temperature (150°C) one for each specific thickness. Furthermore, the charge increases almost linearly with thickness for the 150°C silicon nitride whereas for the 250°C material, the linear dependence is not as clear [104], [112]. This result indicates that for the lower temperature material, the distribution of charges across the dielectric film is more pronounced; whereas for the higher temperature material, charges seem to be more confined to the dielectric surface.

3.2.2 The Effect of Film Thickness in MEMS Switches

We also fabricated RF MEMS switches with two different thicknesses (200 nm and 430 nm) of PECVD silicon nitride deposited at 150°C to see the effect of dielectric film thickness on the charging of the switches. C-V measurements were performed with

an increment of 0.5 V as described before. Figure 3.15 shows the voltage minimum (V_m) shift versus temperature for the 200 nm and 430 nm thick cases. It can be seen that there is a larger variation of V_m in the 430 nm case than in the 200 nm case. This shows a larger charging effect in thicker dielectrics, which is consistent with the results obtained from MIM capacitors. The voltage minimum shifts for the 200 nm and 400 nm cases were fitted using (3.14).

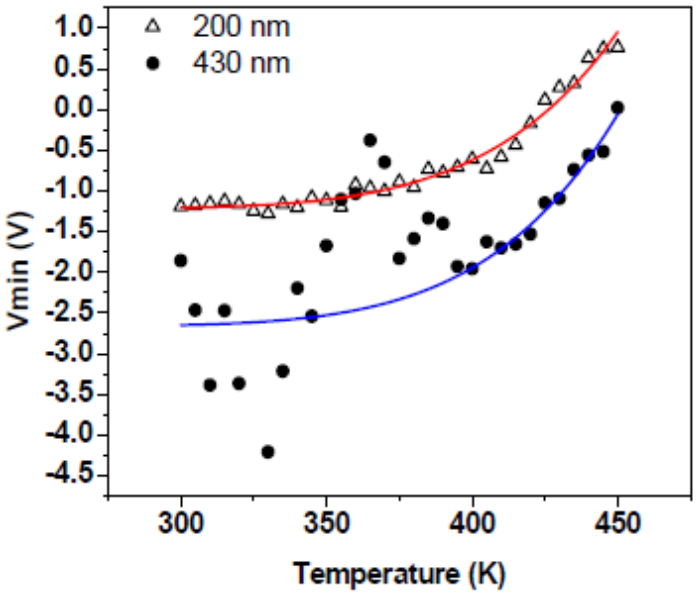

Figure 3.15. Temperature dependence of V_m in switches with 150°C silicon nitride.

Figure 3.16 shows the Arrhenius plot of the shifts in V_m (ΔV_m) (obtained from Figure 3.15) in a logarithmic scale versus the inverse of temperature.

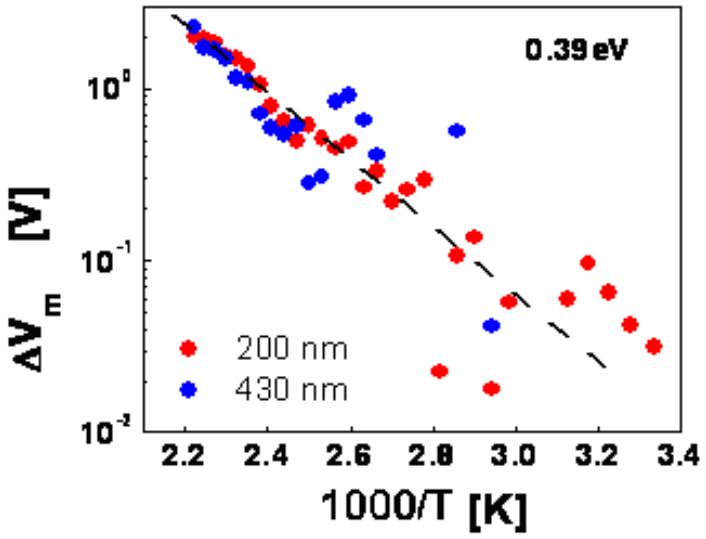

Figure 3.16. Arrhenius plot of ΔV_m in 150°C silicon nitride switches.

Activation energy of 0.39 eV was obtained for both dielectric thicknesses of Figure 3.16 above room temperature (300K). This is consistent with the result reported earlier in Figure 3.11 (a). However, this value is larger than the one determined from TSDC experiments (Figure 3.12 and Figure 3.13). This difference has to be attributed to the fact that in MEMS switches, the collection of injected charge is achieved only through the CPW line. This obviously delays charge collection from the dielectric and leads to larger activation energies through additional trapping mechanisms [112].

Finally, charge kinetics was investigated through the "off-state" transient response of the switch capacitance. When a voltage step from on-state to zero is applied to the switch and the switch is driven to the off-state, its capacitance is determined by the remaining dielectric polarization which gives rise to a parasitic voltage, termed V_p in [38]. Then the off-state capacitance will be determined by the electrostatic force that in

turn will depend on the non-uniform distribution of charges in the dielectric. This electrostatic force will decrease monotonously with time since both the space charge and dipolar polarization will decay with time. The off-state capacitance will vary with time along with the dielectric polarization.

It has been shown that the "off-state" capacitance transients of a switch follow the stretched exponential relaxation law [80]. According to this, the capacitance decay may be written as

$$C(t) = C_{\infty} + \Delta C_0 \exp\left[-\left(\frac{t}{\tau(T)}\right)^{\gamma}\right] \tag{3.16}$$

where C_{∞} is the steady-state capacitance and ΔC_0 is the transient amplitude. The transient component of the capacitance is much smaller than the steady-state one and is written as

$$\Delta C(t) = \Delta C_0 \exp\left[-\left(\frac{t}{\tau(T)}\right)^{\gamma}\right] \tag{3.17}$$

where τ is the relaxation process time constant and γ is the exponent stretch factor ($0 \leq \gamma \leq 1$).

As stated before, the process time constant τ is thermally activated in silicon nitride, and is described by

$$\tau(T) = \tau_0 . \exp\left(\frac{E_A}{kT}\right) \tag{3.18}$$

where E_A is the activation energy and τ_0^{-1} is the escape frequency.

The time constant variation with temperature in the range of 290K-450K with 5K increments in shown in Figure 3.17. The switch dielectric is a 200 nm thick silicon nitride film deposited at 150°C. For each measurement, a bias step of V_{PI} or -V_{PI} to 0 V is applied to the switch and the capacitance transient is recorded every 1 second for a total duration of 200 seconds. The on-state bias voltage is applied for 5 seconds to avoid excess charging. The device is allowed to relax for two hours after each transient measurement.

Figure 3.17 shows the Arrhenius plot for both positive and negative on-state bias voltages. The temperature dependence of τ reveals that the process time constant does not depend on the polarity of the charging/polarization bias [80]. Moreover, the Arrhenius plot reveals the presence of two thermally activated mechanisms with activation energies of 0.45eV at high temperatures and 0.54eV at lower temperatures. Here, it must be pointed out that the higher activation energy at lower temperatures arises from a large dispersion of time constant values.

Comparing Figure 3.17 with the ΔV_m plot in Figure 3.16, it is seen that the activation energies of bias for capacitance minimum (0.39 eV) and the high-temperature region relaxation time (0.45 eV) do not differ significantly and may probably arise from the same charge trapping or dipole orientation mechanisms. Moreover, in the low-temperature region, where the activation energy changes, more dispersion in the ΔV_m plot is seen as well.

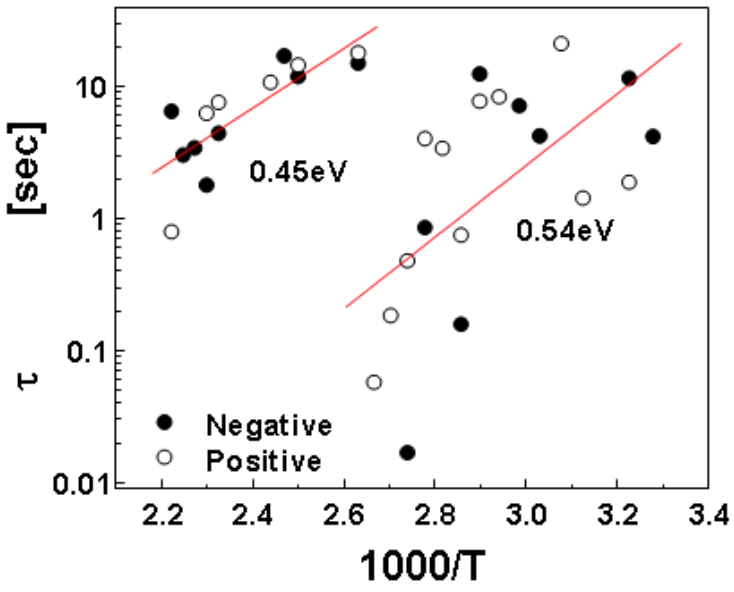

Figure 3.17. Arrhenius plot of the time constant for the pull-up capacitance transients. The switch dielectric is silicon nitride deposited at 150°C.

3.2.3 Summary

In this section, the dependence of charging mechanisms on the dielectric film thickness was investigated. The study was performed by employing RF MEMS capacitive switches with 200 nm and 430 nm thick silicon nitride layers deposited at 150°C. MIM capacitors were also fabricated with 100 nm to 600 nm thick silicon nitride deposited at 150°C and 250°C. Both MIM capacitors and MEMS switches showed higher charging effects in thicker dielectrics. At each specific dielectric thickness, the calculated stored charge was higher for the 250°C silicon nitride than for the 150°C material.

Moreover, the TSDC spectra above room temperature exhibited a certain activation energy that was independent of the dielectric film thickness. In the case of MEMS switches with 200 nm and 430 nm thick silicon nitride layers, the activation

energy obtained for the Arrhenius plots of ΔV_m was also independent of the dielectric thickness. These results suggest that we could include this behavior in modeling tools.

Finally, the calculated stored charge in MIM capacitors with 150°C and 250°C silicon nitride deposited at different thicknesses (Figure 3.14) revealed that charges accumulate near the film surfaces in the case of the high-temperature (250°C) material. On the other hand, charges distribute across the material volume in the case of the low-temperature (150°C) material. These results indicated that the decrease of deposition temperature increases the distribution of charges across the dielectric film, potentially increasing charge leakage across the film.

3.3 The Effect of Dielectric Film Leakage

This part focuses on PECVD silicon nitride films deposited at the same temperature but with different nitrogen to silicon concentration ratios, and tries to determine the dependence of dielectric charging on the silicon content hence the dielectric material conductivity. The goal is to address the uncertainty of whether the implementation of a leaky dielectric would reduce the charging effects in capacitive MEMS switches. Both RF MEMS switches and MIM capacitors with silicon nitride films deposited at 150ºC and 250ºC are considered for this study.

3.3.1 Silicon Nitride Characterization

The dielectric film used in this part is PECVD silicon nitride deposited at 150ºC and 250ºC. For each temperature, the silane flow was changed in order to modify the dielectric material conductivity. The original gas flows for the PECVD SiN_x deposition

are shown in Table 3.2. These flows have been used so far (sections 3.1 and 3.2), and yield $[NH_3]/[SiH_4]$ ratio of 4%. For this study, silane flows of 100ccm, 200cc, 400ccm, and 600ccm are used. The corresponding $[NH_3]/[SiH_4]$ ratios are given in Table 3.3. Table 3.3 also shows the stoichiometry of the films resulted from XPS measurements. The dielectric is 200 nm thick in all cases.

Table 3.2.
Original gas flows for PECVD silicon nitride deposition.

Gas	Flow (ccm)
SiH_4	200
NH_3	8
He	560
N_2	150

Table 3.3.
Stoichiometry of SiN_x films deposited at two different temperatures with different gas flow ratios.

Temperature		**150°C**	**250°C**
Silane Flow (ccm)	$[NH_3]/[SiH_4]$	N/Si	N/Si
100	8%	0.98	1.04
200	4%	0.64	0.8
400	2%	0.41	0.57
600	1.33%	0.33	0.47

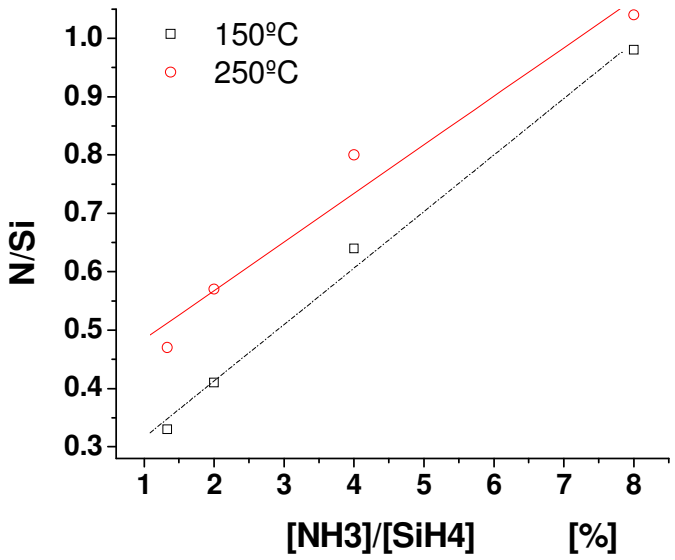

Figure 3.18. N/Si ratio for 200 nm silicon nitride on high resistivity silicon. The films are deposited at 150ºC and 250ºC with different gas flow ratios. The straight lines are drawn to show the stoichiometry trend.

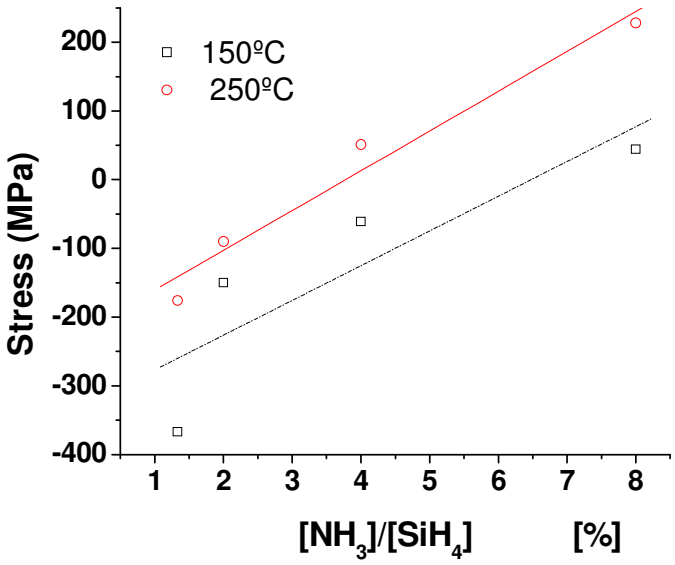

Figure 3.19. Film stress for 200 nm silicon nitride deposited on silicon with different gas flow ratios. The linear fit was performed to show the average stress trend.

The dependence of the silicon nitride film stoichiometry on gas flow ratios is better shown in Figure 3.18. The nitrogen content of the 250ºC silicon nitride is higher than the 150ºC material for all flow ratios, and at each temperature, the increase of $[NH_3]/[SiH_4]$ ratio causes the nitrogen content to increase. The stoichiometries of the 150ºC and 250ºC films seem to converge as the $[NH_3]/[SiH_4]$ ratio increases.

Figure 3.19 shows the dependence of silicon nitride film stress on gas flow ratios for 150ºC and 250ºC deposition temperatures. It is seen that the stress value increases with an increase of the nitrogen content. The stress is compressive for low nitrogen content films, and becomes tensile as the nitrogen content increases for both 150ºC and 250ºC deposition temperatures.

3.3.2 MIM Capacitors Results and Discussion

The electrical properties of the dielectric films in MIM capacitors were assessed using the thermally stimulated depolarization current (TSDC) method and current-voltage (I-V) characteristic measurements. Figure 3.20 shows the I-V characteristics for the 150ºC silicon nitride material. Two different gas flow ratios are shown: $[NH_3]/[SiH_4]=1.33\%$ and $[NH_3]/[SiH_4]=2\%$. It is clearly seen that by decreasing the nitrogen content the leakage current increases, being in agreement with the results presented in [113]. The I-V characteristics of the samples with $[NH_3]/[SiH_4]=4\%$ and $[NH_3]/[SiH_4]=8\%$ are masked by the displacement currents. The I-V characteristics for the 250ºC silicon nitride material follow the same trend.

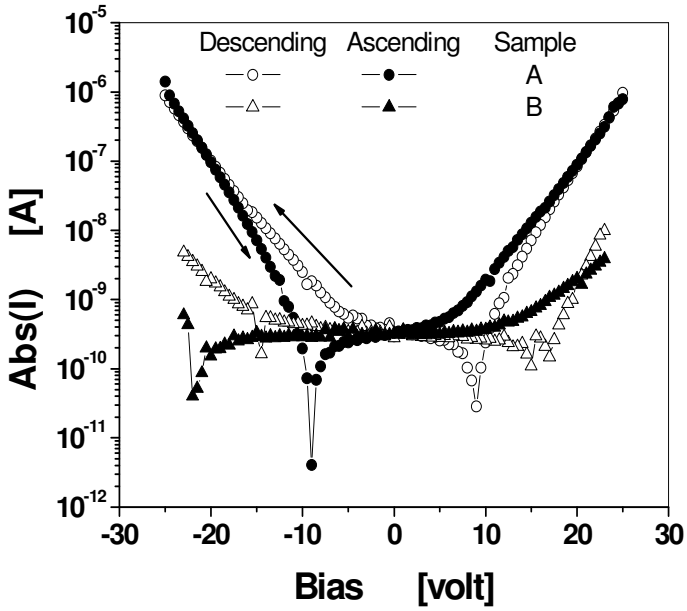

Figure 3.20. Effect of material composition on I-V characteristic. The dielectric is PEVCD silicon nitride deposited at 150ºC.

Here it must be pointed out that the measured leakage current falls to zero at bias levels for which the depolarization current becomes equal to the injected current $\left(J_{depolarization} = J_{injection}\right)$, which is determined by the voltage sweeping rate, the total charging time, charge trapping centers characteristics, and trapped charge distribution. For this reason the bias at which the measured current becomes zero has the same polarity as the starting one. Moreover, the bias at which the measured current is zero is found to decrease with decreasing the nitrogen content. This behavior is attributed to an increase of the leakage current due to the formation of nanoclusters [101, 114, 115] and traps which allow charge transport through conductive percolation tunneling paths and hopping through defect states [116]. Therefore, in order to achieve the null condition, the

applied electric field must decrease in order to significantly reduce the injected current and give rise to the $J_{depolarization} = J_{injection}$ condition.

An insight to the distribution of defects in the dielectric film as well as the variation of their distribution with modifying the deposition conditions can be obtained using the TSDC method. The TSDC spectra for the 150ºC silicon nitride material for three different $[NH_3]/[SiH_4]$ flow ratios of 1.33% (sample A), 2% (sample B), and 4% (sample C) are shown in the inset of Figure 3.21. The TSDC spectra were found to depend strongly on the film composition and showed discrete components at low temperatures. A closer view of the TSDC spectra reveals that in the case of sample A ($[NH_3]/[SiH_4]$=1.33%), the current level at high temperatures is almost two orders of magnitude larger than those of the samples B ($[NH_3]/[SiH_4]$=2%) and C ($[NH_3]/[SiH_4]$=4%), indicating a significantly larger stored charge. The overall behavior of the TSDC spectra can be summarized as follows:

1. The concentration of defects decreases with decreasing the silicon content.

2. In the low temperature range, below 330K, the activation energy is practically equal (~0.20eV) for all samples revealing the same nature of defects.

3. The increase of silicon content introduces new defects with deeper concentrations and larger activation energies (~0.83eV for sample A), which is manifested at higher temperatures and corresponds to larger time constants at room temperature [79], as well as it seems to modify the structure of shallower defects (T<330K for sample A).

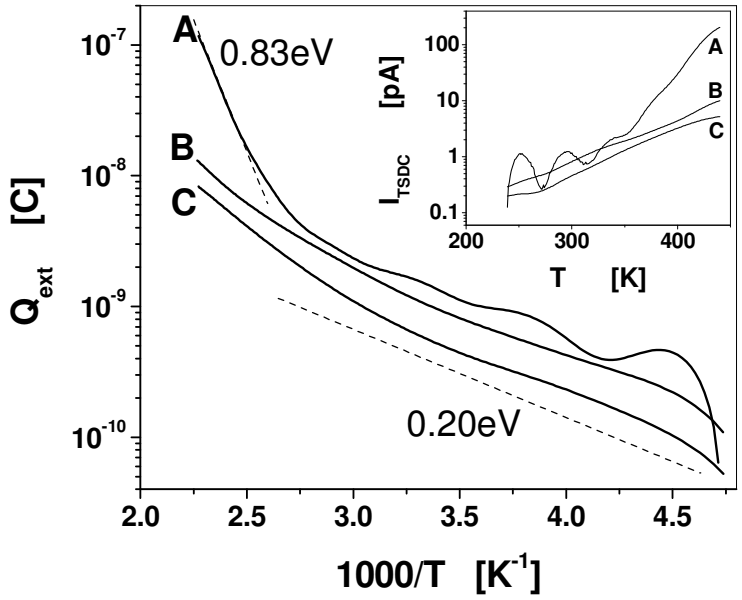

Figure 3.21. Temperature dependence of stored charge (measured in the external circuit) for the 150ºC silicon nitride MIM capacitors. The straight line was drawn to show the trend of Arrhenius plots. The inset shows the TSDC spectra. Samples A, B, and C, correspond to $[NH_3]/[SiH_4]$ flow ratios of 1.33%, 2% and 4% respectively.

This becomes obvious in the plot of the temperature dependence of Q_{ext}, which is calculated as mentioned before in (3.10) by integrating the TSDC spectra over temperature (Figure 3.21). Here it must be pointed out that this behavior reveals that charge transport takes place through conductive percolation and charge trapping [101, 114-116]. Finally, the continuous nature of the TSDC spectra at higher temperatures with a thermally activated envelope indicates a fractal distribution of the charge trapping process [103].

The same trend is obtained for the 250ºC silicon nitride material and with $[NH_3]/[SiH_4]$ flow ratios of 1.33%, 2%, 4%, and 8% (Figure 3.22).

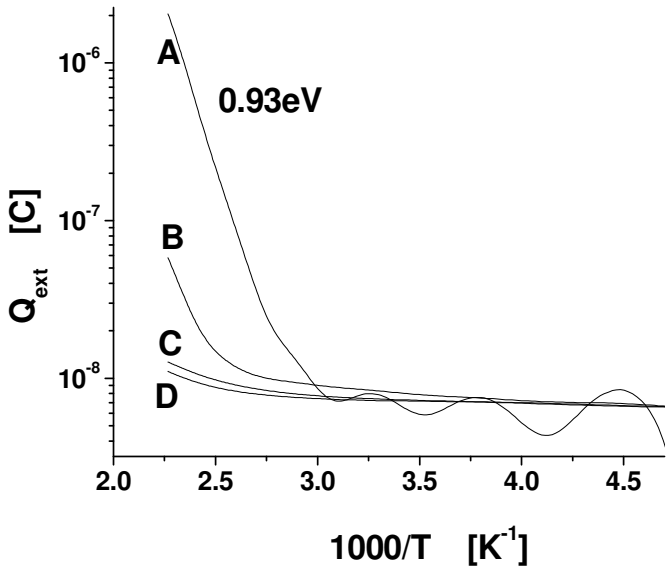

Figure 3.22. Temperature dependence of stored charge (measured in the external circuit) for the 250ºC silicon nitride MIM capacitors. The straight line was drawn to show the trend of Arrhenius plots. Samples A, B, C, and D correspond to $[NH_3]/[SiH_4]$ flow ratios of 1.33%, 2%, 4%, and 8% respectively.

The dependence of the total stored charge on silane flow is shown in Figure 3.23. The total charge is calculated for all materials using (3.10) by integrating the TSDC spectra from 200K to 500K. The total charge stored in the 250ºC silicon nitride is higher than the 150ºC one for all flow ratios. The stored charges in the 250ºC and 150ºC materials seem to have their closest values for silane flow of 200 ccm ($[NH_3]/[SiH_4]$=4%).

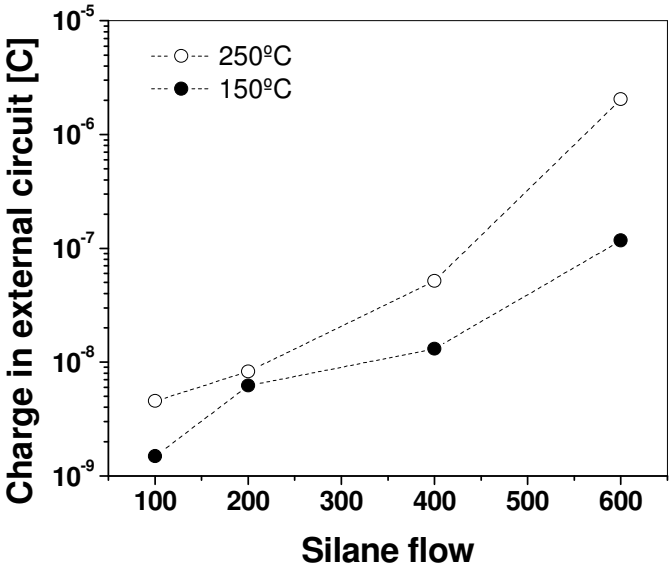

Figure 3.23. Dependence of the stored charge measured in the external circuit on silane flow for the 150ºC and 250ºC silicon nitride material.

3.3.3 MEMS Switches Results and Discussion

The charging in MEMS switches with non-flat metal plates and dielectric layers of uniform thicknesses can be monitored through the shift of bias for minimum capacitance (V_m). Figure 3.24 shows the temperature dependence of V_m for 150ºC silicon nitride MEMS switches. $[NH_3]/[SiH_4]$ flow ratios of 1.33%, 2%, and 4% are shown in Figure 3.24.

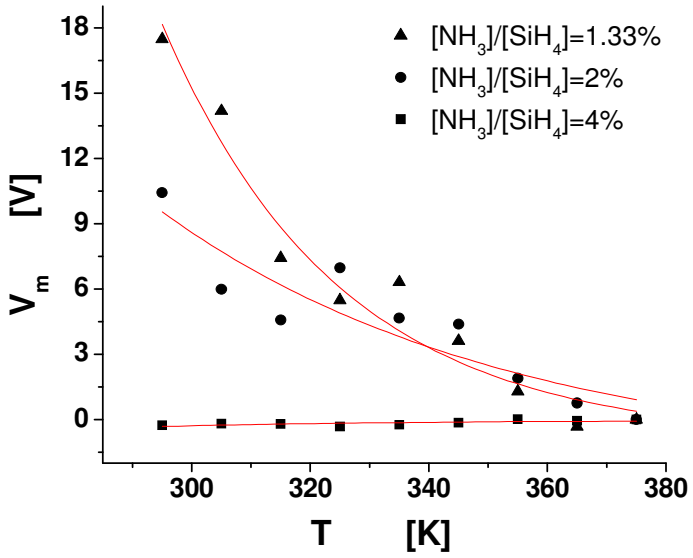

Figure 3.24. Temperature dependence of V_m for 150ºC silicon nitride MEMS switches. $[NH_3]/[SiH_4]$ flow ratios of 1.33%, 2%, and 4% are used.

The bias for minimum capacitance (V_m) corresponding to the sample with $[NH_3]/[SiH_4]$=1.33% was found to shift rapidly with temperature from +12.6 volts at 300K to -5 volts at 380K (Figure 3.24). On the other hand, V_m for the sample with $[NH_3]/[SiH_4]$=4% shifted only from -1.2 volts at 300K to -0.9 volts at 380K. These shifts correspond to induced/injected charges of $3.6\text{x}10^{-7}$ C/cm^2, $2.6\text{x}10^{-8}$ C/cm^2, and $6.6\text{x}10^{-9}$ C/cm^2 for samples with $[NH_3]/[SiH_4]$=1.33%, 2%, and 4% respectively. The presence of thermally activated mechanisms was further confirmed by fitting (3.14) to the experimental data of Figure 3.24. The calculated activation energies were found to be 0.31 eV, 0.22 eV, and 0.11 eV for samples with $[NH_3]/[SiH_4]$=1.33%, 2%, and 4%, respectively, being in reasonable agreement with the values obtained from TSDC assessments at lower temperatures. The absence of higher activation energies can be

attributed to the fact that the MEMS assessment was restricted to 380K, which is close to the onset of the contribution of deeper defects (Figure 3.21).

The temperature dependence of V_m for the 250ºC silicon nitride MEMS switches follow the same trend as the 150ºC ones (Figure 3.25). Larger V_m shifts are seen for samples with less nitrogen content, corresponding to higher levels of induced/injected charge.

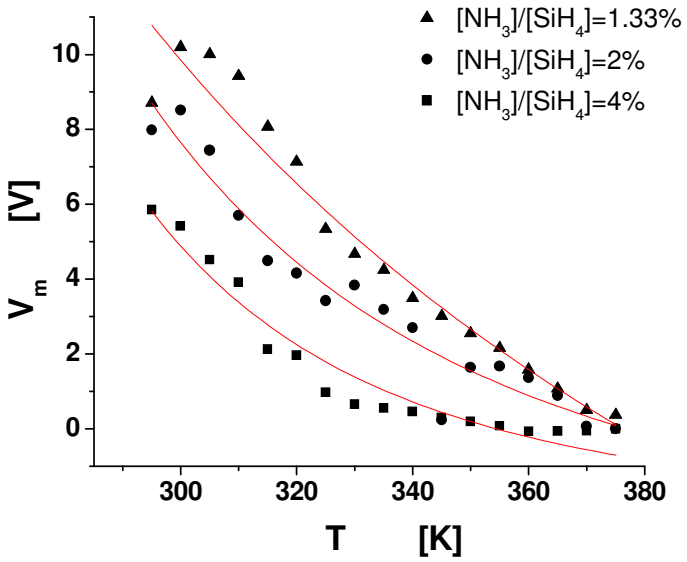

Figure 3.25. Temperature dependence of V_m for 250ºC silicon nitride MEMS switches. $[NH_3]/[SiH_4]$ flow ratios of 1.33%, 2%, and 4% are used.

3.3.4 Summary

In summary, a systematic investigation was performed to relate the electrical properties of the silicon nitride insulating film of MEMS capacitive switches with the monitored dielectric charging. The investigation was focused on silicon-rich PECVD silicon nitride, which deviates significantly from the ideal material stoichiometry. MIM

capacitors and MEMS switches with PECVD silicon nitride deposited at high temperatures (250ºC) as well as low temperatures (150ºC) were considered for this study. It was found that by increasing the amount of incorporated silicon, the leakage current increases as well due to percolation and hopping charge transport. Both assessment methods, the TSDC assessment in MIM capacitors and monitoring the shift of bias for capacitance minimum in MEMS switches revealed that charging increases when the silicon content increases in spite of the increasing leakage current. This is attributed to the formation of silicon nanoclusters, where potential barriers retain the trapped charges in the potential wells, as well as an increase in the concentration of already existing and the generation of new trapping sites by unsaturated bonds, etc. Taking all these into account, we are led to the conclusion that silicon nitride films that are closer to stoichiometry seem to be more promising materials for reliable switches. Since in such highly resistive materials the injected charges require a large time to be collected by the bottom electrode, further investigation is needed the determination of an optimum solution.

CHAPTER 4

DIELECTRIC CHARGING IN CAPACITIVE RF MEMS SWITCHES WITH SILICON DIOXIDE

4.1 The Effect of Actuation Mechanism

In this section, we investigate dielectric charging effects in capacitive RF MEMS switches with silicon dioxide as the dielectric material. Two different actuation schemes, each with different sweep rates are implemented to better understand the effect of charging history over time. An advanced 3D model for the switch is developed, and the complication caused by surface roughness is taken into account.

By monitoring the temperature evolution of the capacitance-voltage characteristic we obtain a better understanding of the charging induced in a single C-V cycle, as well as the presence of thermally activated mechanisms. Our investigation is based on the fact that temperature plays a key role in the injected charge redistribution. Several parameters, such as the charging time constant and its dependence on activation energy are determined. The importance of the determination of these parameters is in that thermally activated mechanisms are easily traced and can be directly related to the material deposition parameters.

4.1.1 Theory and Model

The elementary theory of dielectric materials states that the increase of temperature accelerates the thermally activated polarization–depolarization (charging-discharging) processes [103]. This effect is particularly exploited in the field of MOS

technology and precisely for the investigation of temperature effects on hot carrier stress [117, 118]. In MEMS switches however, the dielectric film is much thicker than the MOSFET gate oxide. This excludes the charging due to Fowler-Nordheim effect [96]. Moreover, the armature contact is not perfect due to surface roughness and asperities. The necessity to take these effects into account has led to the development of the device model presented in [119], which explains the shift of the actuation characteristics and the deformation of the C-V curves without assuming any trapping/detrapping.

In this section, we implement the device model and formulation proposed in [119] in order to take into account the complication caused by surface roughness in capacitive MEMS switches. We consider the setup in Figure 4.1, which includes a fixed non-flat metal plate of area A covered with a dielectric layer of uniform thickness d_ε, dielectric constant ε_r, and volume charge density $\psi\ (x, y, z)$. Above it, a rigid but non-flat movable metal plate is fastened with a linear spring k to a fixed wall above the dielectric layer at a rest position $d_0\ (x, y)$. A dc bias source of amplitude V is applied between the two plates. Following the procedure analyzed in [119] we find that the electrostatic force F_{el} can be written in a compact form of

$$F_{el}(\Delta) = \frac{A}{2\varepsilon_0}\left[(V\mu_\alpha - \mu_\beta)^2 + V^2\sigma_\alpha^2 + \sigma_\beta^2 - 2V\,\mathrm{cov}_{(\alpha,\beta)}\right] \tag{4.1}$$

where μ, σ^2, and cov denote the mean, variance, and covariance, respectively, of $\alpha(x, y, \Delta)$ and charge $\beta(x, y, \Delta)$ distributions and

$$\alpha(x, y, \Delta) = \frac{\varepsilon_0}{\left(d_0(x, y) - \Delta\right) - \dfrac{d_\varepsilon}{\varepsilon_r}} \tag{4.2}$$

is the distribution of capacitance per unit area and

$$\beta(x, y, \Delta) = \frac{d_\varepsilon}{\varepsilon_r \varepsilon_0} \cdot \psi_{eq}(x, y) \cdot \alpha(x, y) \tag{4.3}$$

is the charge distribution on the top electrode due to the charges trapped in the dielectric. $\psi_{eq}(x, y)$ is the equivalent surface charge distribution and Δ is the displacement from equilibrium. F_{el} is therefore a function of the displacement Δ through these mean, variance, and covariance functions.

In the approximation of an ideal spring of spring constant *k*, the magnitude of the spring force exerted on the movable electrode is proportional to the displacement from the rest position and given by

$$F_{spring}(\Delta) = k\,[d_0\,(x,\,y) - d\,(x,\,y)] = k\,\Delta \tag{4.4}$$

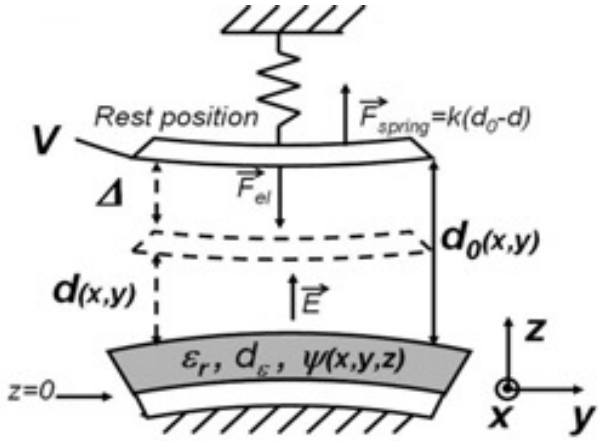

Figure 4.1. Model of a capacitive switch with non-uniform trapped charge and air gap distributions [119].

At equilibrium positions the system is determined by equating (4.1) and (4.4), which reduce to

$$\frac{2\varepsilon_0 k\Delta}{A} = \left(V\mu_\alpha - \mu_\beta\right)^2 + V^2\sigma_\alpha^2 + \sigma_\beta^2 - 2V\,\mathrm{cov}_{(\alpha,\beta)} \tag{4.5}$$

Depending on the adopted device model, the above equations can lead to different levels of complexity approximating the behavior of real MEMS switches. In the general case of distributed equivalent charge Ψ (x,y,z) and air gap d (x,y), (4.1) cannot be simplified. Then (4.5) can be transformed to get some insight into the profile of the actuation characteristic. By isolating V, the equilibrium positions are described by

$$V = \frac{\mu_\alpha\mu_\beta + \mathrm{cov}_{(\alpha,\beta)}}{\mu_\alpha^2 + \sigma_\alpha^2} \pm \sqrt{\frac{\mu_\alpha\mu_\beta + \mathrm{cov}_{(\alpha,\beta)}}{\mu_\alpha^2 + \sigma_\alpha^2} + \frac{\frac{2\varepsilon_0 k\Delta}{A} - \left(\mu_\beta^2 + \sigma_\beta^2\right)}{\mu_\alpha^2 + \sigma_\alpha^2}} \tag{4.6}$$

Equation (4.6) can numerically demonstrate the evolution of C-V characteristic under different geometrical and charge distribution conditions. In the present case, we need to provide concrete results related to dielectric material properties. Therefore, we change (4.6) to a more applicable form so as to introduce our experimental data to it. The experimental data that can be obtained from a C-V characteristic are the pull-in (V_{pi}) and pull-out (V_{po}) voltages as well as the bias at which the capacitance in the up state attains its minimum (V_m). Since the spring constant of a switch is affected by temperature, the interpretation of the temperature dependence of pull-in and pull-out voltages requires some knowledge of the variation of spring constant. On the other hand, the bias for minimum capacitance becomes minimized independently of the charge and air gap distributions. This can be achieved from (4.1) by setting the derivative of F_{el} with respect to V equal to zero. We therefore obtain:

$$V_m = \frac{\mu_\alpha \mu_\beta + \mathrm{cov}_{(\alpha,\beta)}}{\mu_\alpha^2 + \sigma_\alpha^2} \tag{4.7}$$

V_m is thus independent of the spring constant value, and depends only on the dielectric film charging state.

According to this, (4.6) can be significantly simplified to

$$V = V_m \pm \sqrt{V_m + \frac{\frac{2\varepsilon_0 k\Delta}{A} - \left(\mu_\beta^2 + \sigma_\beta^2\right)}{\mu_\alpha^2 + \sigma_\alpha^2}} \tag{4.8}$$

suggesting that in equilibrium positions, the dc voltage across the switch can be expressed in terms of the bias for capacitance minimum (V_m), mean and variance values of charge and capacitance distributions, and displacement (Δ).

Here, we must emphasize that (4.8) still cannot lead to analytical solutions of pull-in and pull-out voltages. To minimize this problem and obtain a better understanding of the charging mechanisms we can take for granted that we measure the pull-in and pull-out voltages very close to, but below the instability point. At such a close proximity to the instability point, (4.8) can be used to provide information on the temperature dependence of mean and variance values of the charge at the dielectric surface. It is important to notice that during C-V measurements, V_m will correspond to the last encountered capacitance minimum since it bears the charging history during the down state and discharging history during the up state, depending on the C-V characteristic sweep mechanism and speed .

4.1.2 Experimental Analysis

The switches used here are bridge-type capacitive switches fabricated at MEMtronics Corporation [120, 121]. The switches are fabricated on a pyrex glass substrate. The dielectric material used is a 280 nm thick SiO_2 layer (ε_r =5.5) sputtered on a chromium/gold bottom electrode. The top membrane is a thin layer of aluminum alloy (about 0.3 μm thick), which is attached to the DC and RF grounds. The switches are fully packaged, using a novel wafer-level micro-encapsulation process [16, 121]. This encapsulation method provides a low-loss package (less than 0.15 dB packaged switch loss at 35 GHz), and protects the switches from the adverse effects of humidity that can result in early switch failure. The packaging process creates an ultra-small (0.4 mm × 0.5 mm) protective shell around the switch, enabling a total die size of only 0.6 mm × 0.9 mm [121]. A top view of the switch geometry is shown in Figure 4.2.

The membrane is suspended about 2.2 μm above the dielectric in the un-actuated position. An applied voltage of about 36 V to the bottom electrode causes the membrane to collapse and contact the dielectric layer. This forms a 120 μm x 80 μm capacitor, which shunts the RF signal to ground. The switching time is less than 10 μsecs.

The capacitance-voltage (C-V) characteristics are obtained following the actuation schemes presented in Figure 4.3. The choice of the actuation scheme is described later. To control the charging time during each pull-down state we varied the voltage sweep speed. Three values were chosen, 57 mV/sec, 114 mV/sec, and 228 mV/sec. Finally, the C-V characteristic was recorded in the temperature range of 300K to 373K. A typical C-V curve obtained at room temperature for the silicon dioxide switches is shown in Figure 4.4.

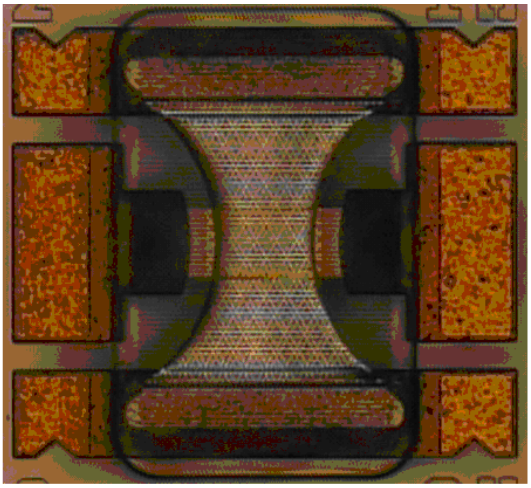

Figure 4.2. Top view of the shunt MEMS capacitive switch [121].

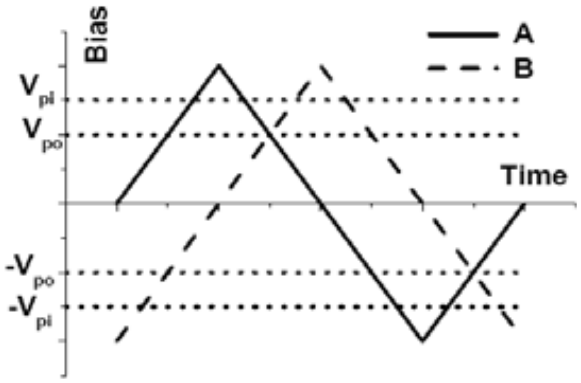

Figure 4.3. Employed actuation schemes.

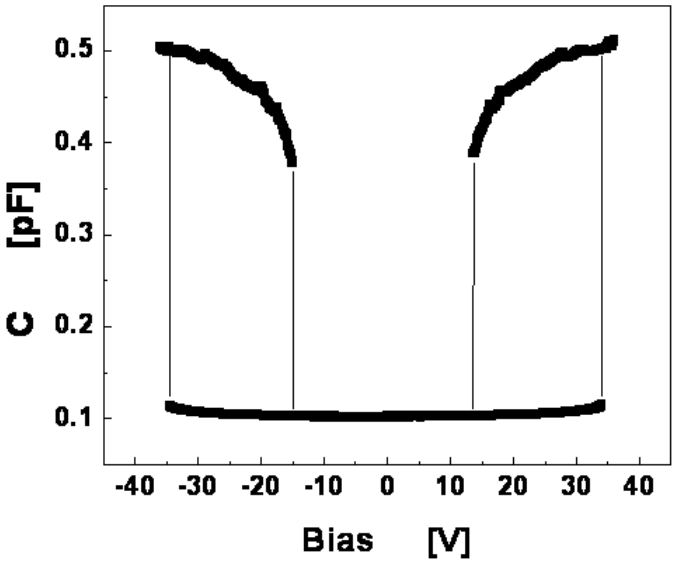

Figure 4.4. The capacitance-voltage characteristic of the capacitive RF MEMS switch with silicon dioxide as its dielectric layer.

4.1.3 Results and Discussion

The choice of the actuation scheme is based on performing two loops where the history of electrical stress before reaching the first and second pull-in voltages is different. In the case of scheme A (Figure 4.3), the first pull-in is attained without previous charging, while the second one is affected by the unipolar charging during positive actuation. In the case of scheme B (Figure 4.3), the first pull-in is attained after charging during negative actuation, while the second one is affected by the discharging and the simultaneous charging during positive actuation.

A typical C-V characteristic of a MEMS switch obtained under pull-up condition at room temperature is plotted in Figure 4.5 a. The characteristic was obtained under scheme B in order to show the effect of cumulative charging during successive pull-down states. The small shift of the capacitance at the rest position by about 0.27 fF (Figure 4.5

a) indicates, according to (4.1) and (4.3), the presence of a relatively small amount of mean and variance values of equivalent charge at the dielectric surface. This charge almost vanishes at elevated temperatures. Meanwhile, the effect of a full cycle on V_m was found to cause a shift of $\Delta V_m \cong$ -0.36 V, which also indicates that $\Delta(\mu_\alpha \mu_\beta + \mathrm{cov}_{(\alpha,\beta)})$ is small with respect to pull-in and pull-out voltages, which are practically determined by the switch mechanical characteristics.

Finally, to further simplify and take advantage of (4.8), we plotted V_m versus temperature (Figure 4.5 b). The temperature dependence of V_m indicates the presence of a residual charge and a thermally activated induced charging, reported also in silicon nitride switches. The activation energy of 0.56 eV is higher compared to silicon nitride switches, which suggests a slower charging process per C-V cycle. The same temperature dependence of V_m This activation energy is the same for both actuation schemes A and B.

Taking all these into account and in order to overcome the non-existent analytical solution of (4.8) and monitor the charging induced during a capacitance-voltage cycle, we assume that the charge density variance at the dielectric surface is low and define the sums $\Sigma V_{pi} = V_{pi}^{+} - V_{pi}^{-}$ and $\Sigma V_{po} = V_{po}^{+} - V_{po}^{-}$. Due to the small values of V_m and charge density mean and variance, the above sums are expected to be mainly affected by the charging history during the prior actuation if any, or the discharging and charging during preceding up-state or down-state, respectively. Figure 4.5 (a) better explains this.

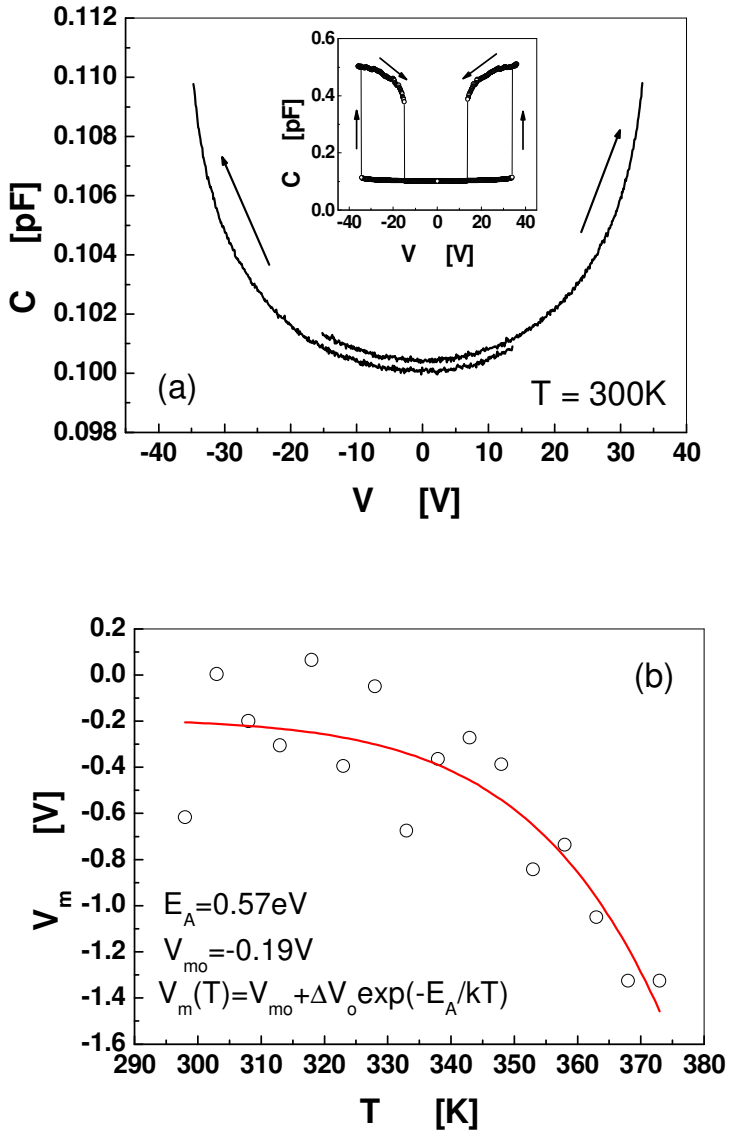

Figure 4.5. Typical capacitance-voltage characteristic obtained under pull-up (the inset shows the full characteristic) and (b): temperature dependence of V_m.

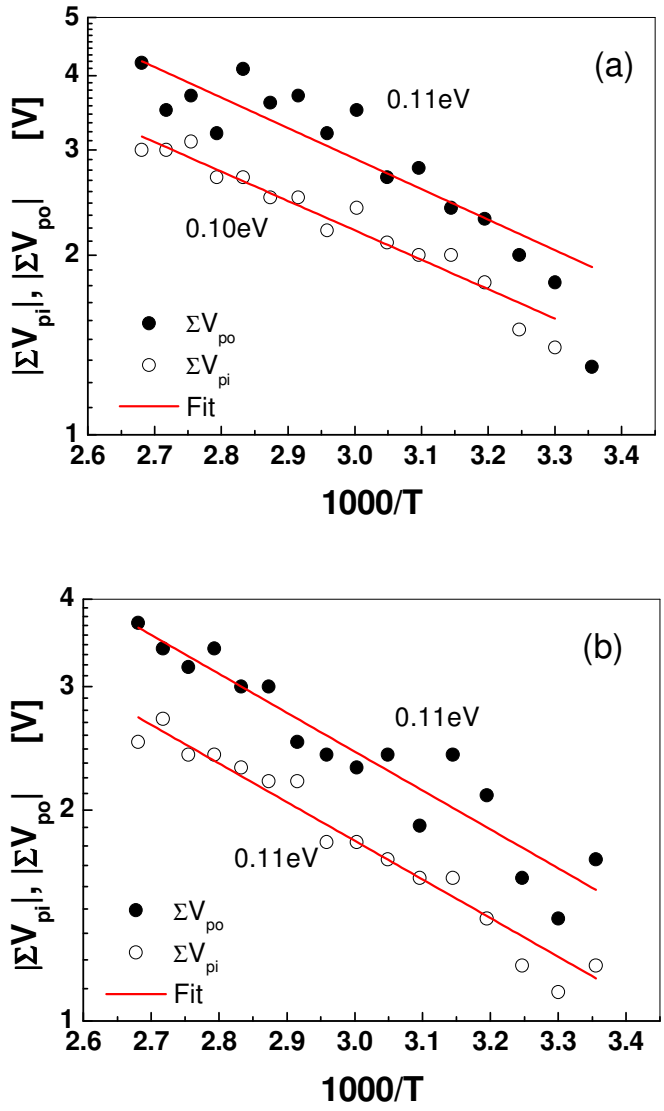

Figure 4.6. Arrhenius plots of the pull-in and pull-out voltage sums for (a) actuation scheme A and (b) actuation scheme B. Sweep rate for both is 57mV/sec.

The sums were found to be thermally activated. The activation energies obtained from the Arrhenius plots in Figure 4.6 (a) and (b) were found to be about 0.11 eV for a sweep rate of 57 mV/sec. This activation energy is found to be different than the one corresponding to V_m. Moreover, it is interesting to point out that for the same sweep rate,

the same activation energies were obtained independently of the capacitance-voltage cycle scheme.

Finally, the calculated activation energy was found to decrease with increasing the bias sweep rate (Figure 4.7). This was expected, because at higher sweep rates, the device remains in the down state for a shorter time and faster defects can respond. Nevertheless, because the pull-in and pull-out windows narrow when the temperature increases, the apparent dependence of the activation energy on the bias sweep rate is still under investigation.

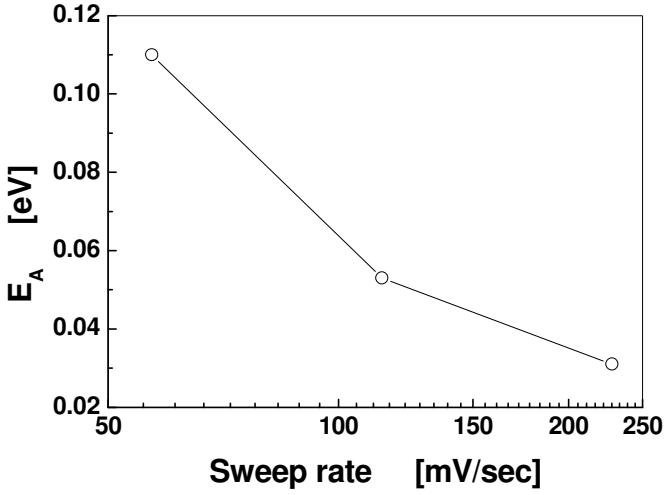

Figure 4.7. Dependence of the activation energy on the bias sweep rate.

4.1.4 Conclusion

Dielectric charging effects in capacitive RF MEMS switches with silicon dioxide were investigated using capacitance-voltage measurements. We developed a general switch model of distributed equivalent charge and air gap. Two actuation schemes were employed to study the dielectric charging effects in order to better understand the

sequence of preceding steps/processes. Taking into account the charging history, it was found that independently of the actuation scheme, charging is thermally activated. The algebraic sums of the pull-in and pull-out voltages ($|\Sigma V_{pi}|$ and $|\Sigma V_{po}|$) allow the determination of charges affecting the corresponding voltages. Different activation energies were found for V_m and $|\Sigma V_{pi}|$ and $|\Sigma V_{po}|$. The calculated activation energies were independent of the actuation scheme. However, the activation energies decreased when the sweep rate increased. Therefore, the C-V sweep rate seems to be related to the dielectric material properties. We can conclude from experimental results that for low charging levels in silicon dioxide, the dominant mechanism is charge injection. Finally, it was shown that the general model of distributed charge and air gap can provide valuable information on the dielectric charging of MEMS switches [122].

4.2 The Effect of Electric Stress

In this section, we investigate the dependence of dielectric charging on the down-state electric field and temperature in capacitive RF MEMS switches with silicon dioxide as the dielectric material. The advanced 3D model developed in section 4.1 will be used in this part as well, and the complication caused by surface roughness is taken into account. Electric field intensities determined by bias levels extending from 0% to 50% above pull-in voltage are employed, and the temperature evolution of the capacitance-voltage (C-V) characteristic of the switch under each level of electric stress is monitored. This investigation is based on the fact that temperature plays a major role on the injected charge redistribution.

It is confirmed that charging is thermally activated in MEMS switches with silicon dioxide. The dependence of the charging time constant and its corresponding activation energy on the magnitude of the stressing electric field intensity are determined.

These results provide a deeper insight into the trapping processes in dielectric materials under different levels of electric stress, and aid in better modeling of charging in capacitive RF MEMS switches. Since thermally activated mechanisms are easily traced and can be directly related to material deposition parameters, device degradation can more easily be predicted and related to material properties prior to device cycling tests.

4.2.1 Experimental Analysis

The same bridge-type capacitive switches used in section 4.1 are used for this part as well. In order to observe the effect of electric stress on charging of the switch, we performed three sets of measurements, each with a different maximum applied electric stress. In the first measurement set, the maximum applied voltage to the switch was equal to its pull-down voltage (V_{pi}). In the subsequent measurement sets, $1.3V_{pi}$ and $1.5V_{pi}$ were used as maximum applied voltages. The corresponding electric fields are calculated as 1.29×10^8 V/m, 1.67×10^8 V/m, and 1.93×10^8 V/m, respectively.

The capacitance-voltage (C-V) characteristic was obtained by actuating the switch starting from negative voltages, going up to positive, and then back again to negative voltages (actuation scheme B in Figure 4.3). This actuation scheme allows us to observe both the positive and negative branches of the C-V characteristic and obtain the biases

corresponding to capacitance minimums. A voltage sweep rate of 57 mV/sec was used. The measurements were performed in the temperature range of 295K to 375K.

4.2.2 Results and Discussion

The C-V characteristics of the switches used in this section are practically the same as the one observed in Figure 4.4. The pull-in voltage is 36 V at room temperature. The C-V characteristic of the MEMS switch under pull-up condition shows the presence of a relatively small amount of mean and variance values of equivalent charge at the dielectric surface. This charge almost vanishes at elevated temperatures.

The shifts of V_m versus temperature for different stressing bias levels, obtained by driving the C-V characteristic to V_{pi}, $1.3V_{pi}$, and $1.5V_{pi}$ are shown in Figure 4.8. The temperature dependence of V_m indicates the presence of a thermally activated process [122]. The Arrhenius fitting to the data in Figure 4.8 reveals activation energy values of 0.12 eV, 0.24 eV, and 0.42 eV for stress levels of V_{pi}, $1.3V_{pi}$, and $1.5V_{pi}$, respectively. This shows an increase in activation energy with the stress bias.

The increase of activation energy with increasing the stress bias is in good agreement with the observation of the increase of time constant in discharging MIM capacitors [123] with stress, and in Kelvin Probe Force Microscopy assessment of SiN_x films [124]. This increase in activation energy can be attributed to the effect of the time-dependent Poole-Frenkel current, which assists in charge redistribution. As the electric field increases, the Poole-Frenkel current becomes more pronounced for charges trapped in shallow states. This will decrease the density of trapped charges in shallow traps. Therefore, the effective time for charge collection is mainly determined by deeper traps

with higher time constants. This in turn leads to higher apparent (effective) activation energies.

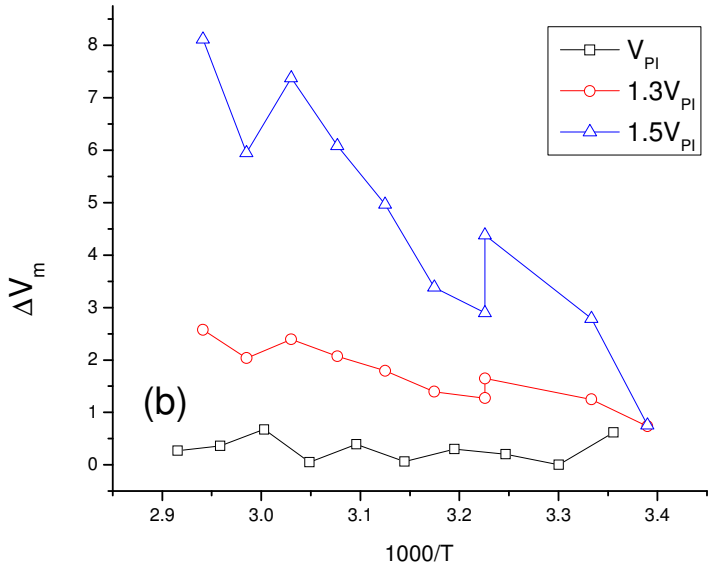

Figure 4.8. Dependence of ΔV_m for bias stress levels of V_{pi}, $1.3V_{pi}$, and $1.5V_{pi}$.

The dependence of the activation energy on electric stress becomes more evident if we calculate the total density of charge per unit area and energy width that is injected in the dielectric through the TAT mechanism for two electric fields of 1.67×10^8 V/m and 1.93×10^8 V/m (corresponding to $1.3V_{pi}$, and $1.5V_{pi}$). Figure 4.9 shows the total charge density per unit area and energy in the dielectric bandgap. Higher numbers on the x-axis exhibit deeper states in the dielectric.

The calculation for Figure 4.9 is done assuming a band gap of 9 eV and band tails in the form of $N_0 \exp\left[\frac{-(E_C - E)}{E_0}\right]$ where $E_0 = 0.25$ eV and $N_0 = 10^{19}$ cm^{-3} [125]. Figure 4.9 clearly shows that the distribution of charges deeper in the insulator gap increases

with increasing the electric field intensity. This will in turn lead to larger apparent (effective) activation energy of the charging process.

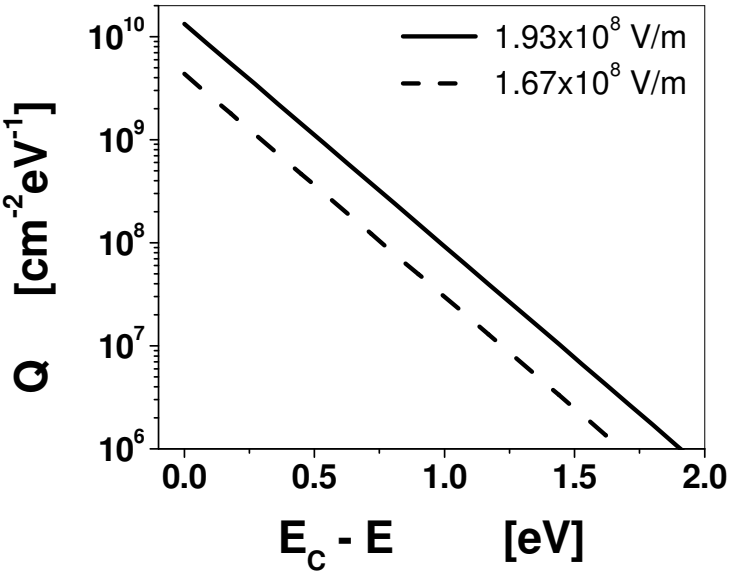

Figure 4.9. Distribution of resulting charge density after TAT injection.

Moreover, following the analysis presented in section 4.1, we define the sums of pull-in and pull-out voltages $\Sigma V_{pi} = V_{pi}^{+} - V_{pi}^{-}$ and $\Sigma V_{po} = V_{po}^{+} - V_{po}^{-}$. Due to small mean and variance values of charge density, the sums are expected to be mainly affected by charging history during the prior actuation, if any, or the discharging and charging during preceding up-state or down-state respectively [122]. Figure 4.10 shows the shift in the sum of the pull-in voltages with temperature for stressing bias levels of V_{pi} and $1.5V_p$. The sum of the pull-out voltages follows a very similar trend. The sums were found to be thermally activated, exhibiting a much faster change with temperature under stress of

$1.5V_{pi}$ compared to V_{pi}. The corresponding activation energies were found to be higher for the higher stress levels, in agreement with the activation energies corresponding to V_m.

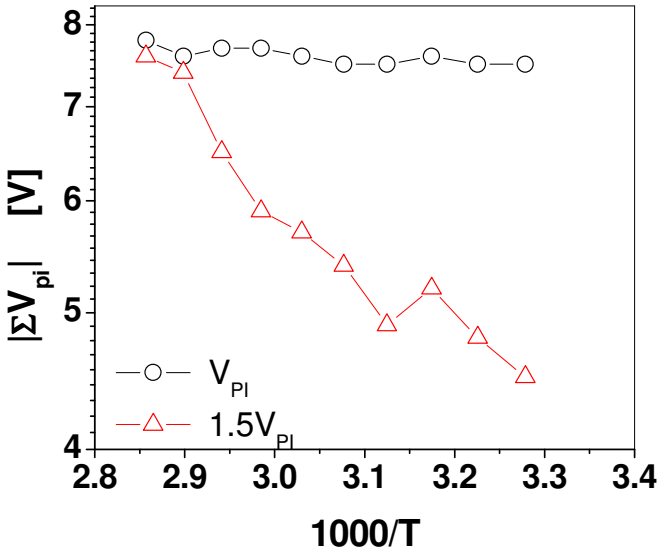

Figure 4.10. Pull-in windows for bias stress levels of V_{pi} and $1.5V_{pi}$.

4.2.3 Conclusion

The charging in capacitive RF MEMS switches with silicon dioxide has been investigated as a function of electric field intensity and temperature. The theory and model proposed in section 4.1 were applied to the switches to analyze the experimental data. The shifts of the pull-in and pull-out windows, and also the shift of the voltage corresponding to minimum capacitance of the switch (V_m) versus temperature were measured for different levels of electric stress, and corresponding activation energies were determined. Results revealed that charging is thermally activated and the apparent (effective) activation energy increases under higher levels of electric stress due to larger contribution from deeper traps. This conclusion is supported by the calculated

distribution of charge density in the insulator bandgap under different electric field intensities. This result provides a deeper insight into the trapping processes in dielectric materials and their corresponding time constants. This will in turn aid in better modeling of charging processes in capacitive RF MEMS switches.

4.3 The Effect of Increased-time Electric Stress

In this work, we aim to experimentally explore the effects of increased-time "constant" electric stress on the dielectric charging of MEMS capacitive switches. This may happen in reconfigurable antennas, where at some point we may be forced to keep the beam at a certain direction for an extended time, or in reconfigurable filters, where we may need to keep a certain state active for a relatively long time. In both these scenarios, the MEMS switch is kept at the on state for long periods of time ($\geq$10 min). A formulation is developed for MEMS switches under increased-time electric stress that explains the relationship between the sum of the pull-out voltages and the voltage at which the minimum capacitance occurs. The importance of this is in that the pull-out voltage can easily be correlated with switch failure. The theoretical model used for this part is also based on the general model developed in 4.1.

4.3.1 Theory and Model

The same device model in Figure 4.1 is used for this part as well. Following the formulation proposed in section 4.1, the equilibrium state of the system is determined by:

$$V = V_m \pm \sqrt{V_m + \frac{\frac{2\varepsilon_0 k\Delta}{A} - \left(\mu_\beta^2 + \sigma_\beta^2\right)}{\mu_\alpha^2 + \sigma_\alpha^2}} \tag{4.9}$$

where V_m is given by (4.7).

At pull-out, the system is still at equilibrium, and a maximum displacement occurs at the center of the bridge due to its symmetrical structure. The sum of the positive and negative pull-out voltages will be given by:

$$\sum V_{po} = V_{mp} + V_{mn} + \sqrt{V_{mp} + \frac{\frac{2\varepsilon_0 k\Delta}{A} - \left(\mu_{\beta p}^2 + \sigma_{\beta p}^2\right)}{\mu_{\alpha p}^2 + \sigma_{\alpha p}^2}} - \sqrt{V_{mn} + \frac{\frac{2\varepsilon_0 k\Delta}{A} - \left(\mu_{\beta n}^2 + \sigma_{\beta n}^2\right)}{\mu_{\alpha n}^2 + \sigma_{\alpha n}^2}} \tag{4.10}$$

where the additional indexes *n* and *p* refer to charge modifications during the positive and negative actuation branches of the C-V characteristic $\left(\psi_{eq} \pm \delta\psi_{eq}\right)$. In order to further investigate the effect of charging, we diminish the contribution of $\delta\psi_{eq}$ by applying an electric stress $\left(\psi_{eq} >> \delta\psi_{eq}\right)$. Under this condition, (4.10) simplifies to:

$$\sum V_{po} \cong V_{mp} + V_{mn} \propto V_m \tag{4.11}$$

and is therefore proportional to the shift of the bias for the capacitance-voltage minimum. The significance of this formulation for the sums of the pullout voltages is in that the pull-out voltages are directly related to switch failure. This was discussed in detail in chapter 2.1 (see Figure 2.3).

4.3.2 Experimental Analysis

The same bridge-type capacitive switches used in section 4.1 are used for this part of our work as well. The capacitance-voltage characteristics were obtained by actuating the switch starting from the negative pull-in, going up to the positive pull-in, and back again to the negative pull-in. All C-V measurements were performed with a bias sweep rate of 57 mV/sec. The switches were measured over a temperature range of 20°C to 100°C with incremental steps of 10°C. For each temperature, the C-V characteristic was measured according to the actuation scheme described above. Then a stress voltage equal to its positive pull-in voltage (37 V) was applied to the switch for 10 minutes. The C-V characteristic was measured again immediately after the stress was removed. The measurements were then repeated at the next temperature after allowing the switch to relax for 12 hours. Figure 4.11 shows the algebraic sums of the pull-in and pull-out voltages versus temperature before and after stress is applied. Corresponding activation energies are also shown in Figure 4.11. The sums of the pull-in and pull-out voltages are thermally activated and have the same activation energies before stress is applied. This is expected as was also seen in Figure 4.6.

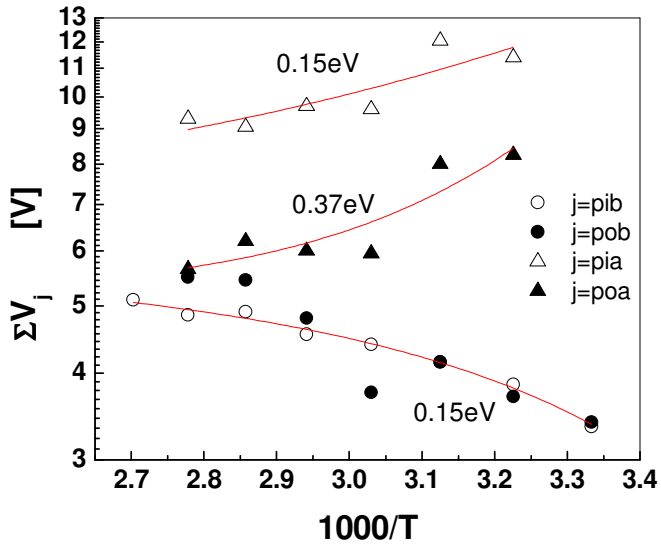

Figure 4.11. Sums of the pull-in and pull-out voltages before and after 10 minutes of "constant" positive electric stress versus temperature. The electric stress was fixed at +37V. pi=pull-in, po=pull-out, b= before stress, a=after stress.

Next, in order to determine the validity of (4.11), we calculated the shifts in V_m and ΣV_{po} after stress was applied (compared to before the stress was applied). The results are plotted in Figure 4.12, and show very good agreement with (4.11). Assuming that $\psi_{eq} >> \delta\psi_{eq}$ when the switch is under electric stress, (4.11) is proven a useful tool in determining charging effects from the well-defined sharp transitions of the pull-out voltage.

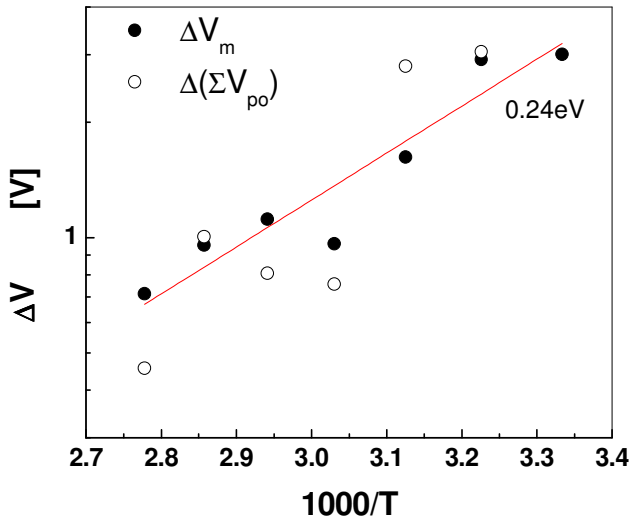

Figure 4.12. Arrhenius plots of $\Delta(V_m)$ and $\Delta(\Sigma V_{po})$.

Finally, we examine the effect of longer stress times on the switch performance. The switch was stressed for 1 hour at its pull-in voltage, and C-V curves were obtained every 12 minutes. Measurements were repeated at three temperatures, 22°C, 62°C, and 102°C. The switch was allowed to relax for 12 hours between each two temperature measurements. Figure 4.13 shows the shifts in the sums of the pull-in and pull-out voltages after stress is applied (compared to before the stress is applied) for the three temperatures mentioned above. The shifts of the pull-in and pull-out windows are found to follow the power law below:

$$\left[\Delta V(t) = \Delta V_0 \left(\frac{t}{\tau}\right)^{\gamma}\right] \tag{4.12}$$

The exponent parameter γ is also shown in Figure 4.13 for the three temperatures mentioned above. The exponent value γ obtained from experimental data increases with temperature. This behavior is also reported in dielectric-less devices [126].

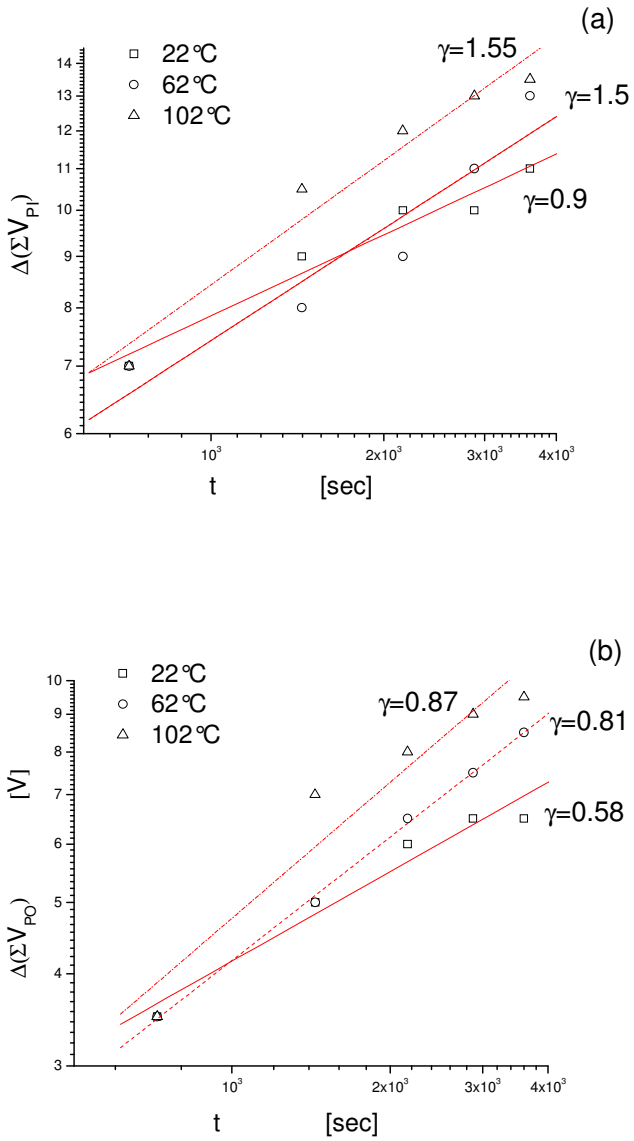

Figure 4.13. Shifts of the switch (a) pull-in and (b) pull-out windows versus stress time. Three different temperatures are examined, and the exponent parameter γ is calculated for each temperature.

4.3.3 Conclusion

The model of non-flat metal plate and arbitrary charge distribution at dielectric surface has been adapted to investigate the charging induced during increased-time electric stress. We show that for long stress periods, charging can be determined from the sharp pull-out transitions and the algebraic sum of pull-out voltages. The shift of the bias for capacitance minimum maintains the same trend as the sum of pull-out voltages, and thus provides an additional tool for investigating the charging effects in MEMS capacitive switches. Experimental results are in good agreement with our developed model. The sum of the pull-out voltages and the bias for capacitance minimum were found to be thermally activated with the same activation energies. The charging process was found to increase with time, obeying a power-law relation. Finally, the temperature dependence of the power-law process was found to be in agreement with results reported in dielectric-less devices.

CHAPTER 5

CONCLUSIONS AND FUTURE WORK

The theme of this thesis was to explore dielectric charging effects in capacitive RF MEMS switches with silicon nitride and silicon dioxide. In this chapter, we summarize the contributions of this dissertation, and provide suggestions for future research directions.

5.1 Contributions

The contributions of this work can be summarized as follows:

1. The mechanisms responsible for dielectric charging of capacitive RF MEMS switches were investigated using films of silicon nitride deposited under different substrate temperature conditions. A direct relationship was obtained between the deposition temperature and material properties (i.e., stress and stoichiometry). It was seen that lower-temperature silicon nitride has less stress and is richer in the silicon component, which results in an increase of the average band-gap with temperature increase. Results from both MEMS switches and MIM capacitors showed that lower-temperature PECVD silicon nitride is less prone to dielectric charging than the higher-temperature one. Different activation energies were obtained for MEMS switches with silicon nitride deposited at different temperatures. This difference may be attributed to different materials' band gaps and band potential fluctuations. Finally, it was seen that charging in silicon nitride is caused by the formation of a meta-stable defect band where carriers can move by hopping between charged states in a manner

similar to the PF effect. The formation of this band seems to contribute to the dielectric charging of silicon nitride.

2. The dependence of charging mechanisms on the dielectric film thickness was investigated. Both MIM capacitors and MEMS switches showed higher charging effects in thicker dielectrics. The activation energies obtained from the MIM capacitors and MEMS switches were independent of the dielectric film thickness. This suggests that we can include this behavior in modeling tools. Moreover, it was revealed that charges accumulate near the film surfaces in the case of the high-temperature (250°C) material. On the other hand, charges distribute across the material volume in the case of the low-temperature (150°C) material. Therefore, the decrease of deposition temperature increases the distribution of charges across the dielectric film, potentially increasing charge leakage across the film.
3. A systematic investigation was performed on silicon-rich PECVD silicon nitride, which deviates significantly from the ideal material stoichiometry. MIM capacitors and MEMS switches with PECVD silicon nitride deposited at high temperatures (250ºC) as well as low temperatures (150ºC) were considered. It was found that by increasing the amount of incorporated silicon, the leakage current increases as well due to percolation and hopping charge transport. TSDC assessment in MIM capacitors and monitoring the shift of bias for capacitance minimum in MEMS switches revealed that charging increases when the silicon content increases. This is attributed to the formation of silicon nanoclusters, where potential barriers retain the trapped charges in the potential wells, as well as an increase in the concentration of already existing and the generation of new trapping sites by unsaturated bonds, etc.

Therefore, silicon nitride films that are closer to stoichiometry seem to be more promising materials for reliable switches.

4. A general switch model of distributed equivalent charge and air gap was developed. Two actuation schemes were employed to study the dielectric charging effects of silicon dioxide switches in order to better understand the sequence of preceding steps/processes. It was found that independently of the actuation scheme, charging is thermally activated. The algebraic sums of the pull-in and pull-out voltages ($|\Sigma V_{pi}|$ and $|\Sigma V_{po}|$) allow the determination of charges affecting the corresponding voltages. Different activation energies were found for V_m and $|\Sigma V_{pi}|$ and $|\Sigma V_{po}|$. The calculated activation energies were independent of the actuation scheme. However, the activation energies decreased when the sweep rate increased. Therefore, the C-V sweep rate seems to be related to the dielectric material properties. Experimental results showed that for low charging levels in silicon dioxide, the dominant mechanism is charge injection.
5. The charging in capacitive RF MEMS switches with silicon dioxide was investigated as a function of electric field intensity and temperature. It was shown that the apparent (effective) activation energy increases under higher levels of electric stress due to larger contribution from deeper traps. This conclusion was supported by the calculated distribution of charge density in the insulator bandgap under different electric field intensities. This result provides a deeper insight into the trapping processes in dielectric materials and their corresponding time constants. This in turn aids in better modeling of charging processes in capacitive RF MEMS switches.

6. For the first time, dielectric charging effects of silicon dioxide capacitive MEMS switches under increased-time constant electric stress were investigated. We showed that for long stress periods (≥10 min), charging can be determined from the sharp pull-out transitions and the algebraic sum of pull-out voltages. The sum of the pull-out voltages and the bias for capacitance minimum were found to be thermally activated with the same activation energies. The charging process was found to increase with time, obeying a power-law relation. Finally, the temperature dependence of the power-law process in silicon dioxide switches was found to follow a similar pattern to the one observed in dielectric-less devices.

5.2 Future Direction

This work establishes several interesting research directions for future work:

1. **RF MEMS switch lifetime testing:** In Chapter 3, an extensive study was performed on silicon nitride capacitive MEMS switches with different dielectric stoichiometries. Favorable deposition conditions were determined in order to induce minimum dielectric charging in the switches. However, for these switches to be deemed appropriate for consumer and military applications, it is important to determine their lifetime. If a device only lasts two month in the field, it is not going to be well liked by its purchasers. Unfortunately, lifetime testing is a time consuming process. At a cycling rate of 1000 Hz, it would take almost 16 years to cycle 500 billion times. Commercial testing is usually performed between 10-20 kHz, which would still take up to 1.5 years to complete. In a university setting where equipment is shared between students, a more manageable goal of at least 100 million cycles can be

attempted. Moreover, the best place to test the lifetime of a switch would be in a clean, dry environment with little air circulation. This is also difficult to achieve in a university setting. Measurement labs are constantly air-conditioned to keep the measurement equipment cool. Packaging the devices in a hermetic enclosure is best, but any kind of covering would also help.

2. **The effects of radiation on charging of the switches:** An interesting extension of the current study would be to examine other factors that may affect the charging characteristics of the switches, such as radiation dose. This is important for space applications where little shielding can be afforded to the space radiation environment. A high radiation dose would certainly cause defect generation in the low-temperature deposited switch dielectric, thereby accelerate charging of the switch. However, to date, there are only a few radiation studies on RF MEMS capacitive switches.
3. **The effects of RF power level on charging of the switches:** Although it is expected that the incident RF power would accelerate charging by raising the temperature of the MEMS device [126], detailed reliability studies are required in order to quantify the exact acceleration factor.
4. **Dielectric charging in high-k dielectrics:** Silicon dioxide and silicon nitride are the most well-known dielectrics for MEMS applications and were investigated in this work. However, several other materials are currently under investigation as well. Crystalline Al_2O_3 and AlN are attractive materials for the switch dielectric because of their high dielectric constant, which makes the switch capacitance ratio high. Although they have shown promising results in initial reliability studies, their

charging behavior needs to be examined in detail before applying these materials to the real switch design.

5. **Innovative materials development:** An interesting line of work would be to tailor and optimize novel materials to diminish dielectric charging effects. Recently, ultra-nano-crystalline diamond (UNCD) thin films were incorporated into MEMS switches using microwave plasma chemical vapor deposition (MPCVD) and hot filament chemical vapor deposition (HFCVD) techniques [127]. These devices exhibited uniquely different charging characteristics, with charging and discharging time constants 5-6 orders of magnitude quicker than conventional materials. There is still significant development required to make this material manufacturable, and limited results have been reported on its charging performance. However, the knowledge gained can open a new path towards engineering novel materials for diminishing dielectric charging effects in capacitive MEMS switches.

CHAPTER 6

PUBLICATIONS TO DATE

6.1 Journal Publications

1. N. Tavassolian, M. Koutsoureli, E. Papandreou, G. Papaioannou, B. Lacroix, Z. Liu, J. Papapolymerou, "The Effect of Silicon Nitride Stoichiometry on Charging Mechanisms in RF MEMS Capacitive Switches," *IEEE Transactions on Microwave Theory and Techniques,* vol. 57, pp. 3518-3524, 2009.
2. S. Yeo, A. Polycarpou, S. Tseregounis, N. Tavassolian, J. Papapolymerou, "Characterization and Adhesion of Interacting Surfaces in Capacitive RF MEMS Switches Undergoing Cycling," *Journal of Adhesion Science and Technology,* vol. 24, pp. 2617–2639, 2010.
3. M. Koutsoureli, N. Tavassolian, G. Papaioannou, J. Papapolymerou, "Dielectric Charging in Capacitive MEMS Switches with Silicon Nitride: The Effect of Dielectric Film Leakage," *Submitted to Applied Physics Letters*, Sep. 2010.
4. N. Tavassolian, M. Koutsoureli, G. Papaioannou, J. Papapolymerou, "the Effects of Dielectric Film Leakage in Capacitive MEMS Switches with Silicon Nitride Deposited at High and Low Temperatures," *to be Submitted to the Journal of Applied Physics*, Nov. 2010.

6.2 Conference Publications

1. N. Tavassolian, G. Papaioannou, J. Papapolymerou, "The Effects of Increased-Time Electric Stress on the Dielectric Charging of Capacitive RF MEMS Switches with Silicon Dioxide", *to be Submitted to IEEE European Microwave Conference*, 2011.
2. N. Tavassolian, M. Koutsoureli, G. Papaioannou, and J. Papapolymerou, "Dielectric Charging in Capacitive RF MEMS Switches: The Effect of Electric Stress," *Proc. IEEE Asian-Pacific Microwave Conference*, pp. 1-4, 2010.
3. N. Tavassolian, M. Koutsoureli, G. Papaioannou, J. Papapolymerou, "The Effects of Dielectric Film Leakage in Capacitive MEMS Switches with Silicon Nitride Deposited at Low Temperatures," *Submitted to IEEE URSI Conference*, Sep. 2010.
4. H. Jiang, B. Lacroix, N. Tavassolian, J. Papapolymerou, "A Compact Tunable Filter using BST Thin film Varactors," *Submitted to IEEE URSI Conference,* 2010.
5. G. Papaioannou, N. Tavassolian, M. Koutsoureli, E. Papandreou, J. Papapolymerou, "Investigation of Charging Mechanisms in RF-MEMS Capacitive Switches with Silicon Nitride: The Effect of Material Stoichiometry," *proc. IEEE International Microwave Symposium*, pp. 1653-1656, 2009.
6. G. Papaioannou, N. Tavassolian, C. L. Goldsmith, and J. Papapolymerou, "Dielectric charging and thermally activated processes in MEMS capacitive switches," *Proc. IEEE European Microwave Conference,* pp. 1752-1755, 2009.

7. R. Daigler, E. Papandreou, N. Tavassolian, M. Koutsoureli, G. Papaioannou, J. Papapolymerou, "Dependence of dielectric charging on film thickness and deposition conditions," *Proc. IEEE Asian-Pacific Microwave Conference*, pp. 1-4, 2009.

8. N. Tavassolian, S. Bhattacharya, G. Ponchak, J. Papapolymerou, "A High-power Low-Actuation Voltage RF MEMS Switch on Silicon and Organic Substates," *Proc. IEEE URSI Conference*, 2009.

9. N. Tavassolian, G. Ponchak, J. Papapolymerou, "Compact Conformal Dipole Antenna on Organic Substrate for 2.4 GHz Applications," *Proc. IEEE Antennas and Propagation Society International Symposium*, 2008.

10. N. Tavassolian, S. Nikolaou, M. Tentzeris, "A Flexible UWB Elliptical Slot Antenna with a Tuning Uneven U-shape Stub on LCP for Microwave Tumor Detection," *Proc. IEEE Asian-Pacific Microwave Conference*, pp. 1-4, 2007.

11. N. Tavassolian, S. Nikolaou, M. Tentzeris, "Microwave Tumor Detection Using a Flexible UWB Elliptical Slot Antenna with a Tuning Uneven U-shape Stub on LCP," *Proc. IEEE Antennas and Propagation Society International Symposium*, pp. 257-260, 2007.

12. J. Jordan, G.E. Ponchak, N. Tavassolian, M. Tentzeris, "Characteristics of a Linearly Tapered Slot Antenna (LTSA) Conformed Longitudinally Around a Cylinder," *Proc. IEEE Antennas and Propagation Society International Symposium*, pp. 3848-3851, 2007.

APPENDIX

MEMS SWITCH FABRICATION RECIPE

This appendix provides a quick overview for MEMS switch fabrication. This recipe was first created by Dr. Nickolas Kingsley in 2005. However, it has gone through several revisions since then.

1) Silicon dioxide deposition (Optional)

-Use Unaxis PECVD to deposit about 3 microns of silicon dioxide.

-Measure with Nanospec profilometer to verify thickness.

2) Electrode deposition

-Use Ebeam1 or Ebeam2 to deposit Ti/Au (100A/2000A).

3) Photoresist 1827

- Spin 3000 RPM at 500 RPM/sec for 30 seconds.

- Put on hot plate at 110°C for 90 seconds.

4) Expose MA6

-Expose on channel 2, 20um gap, 12 sec, hard contact.

-Develop with 319.

5) Electrode wet etch

-etch Au.

-etch Ti.

-Check electrode under microscope.

-Remove photoresisit with acetone.

6) Silicon nitride deposition

-Use unaxis PECVD to deposit 100nm-400nm silicon nitride.

7) Photoresist 1827

- spin 3000 RPM at 500 RPM/sec for 30 seconds.

- Put on hot plate at 110°C for 90 seconds.

8) Expose MA6

-Expose on channel 2, 20um gap, 12 sec, hard contact.

-Develop with 319.

9) Silicon nitride wet etch

-Use 50% H_20 and 50% BOE.

-Check under microscope.

-Remove PR.

-If oxide has been deposited, this will etch it so remove the wafer once the nitride is completely etched.

10) Sacrificial layer (1827)

- Spin 4000 RPM at 500 RPM/sec for 40 seconds.

- Put on hot plate at 110°C for 90 seconds.

11) Expose MA6

-Expose on channel 2, 20um gap, 12 sec, hard contact.

-Develop with 319.

-Check under microscope.

12) Hard bake

- Put the wafer at 130°C on Hotplate for 5-6 minutes.

- Put the wafer at 130°C in oven for 6-8 minutes.

-Check under microscope for bubbling.

- Measure sacrificial thickness with profilometer.

13) Membrane seed layer

-100-200A Ti at 1 A/s

-2000A Au at 1.5 A/s

-100-200A Ti at 1 A/s

-Check under microscope for bubbling

14) Photoresist 1827

- Spin 2000 RPM at 500 RPM/sec for 40 seconds.

- Put in oven for 20-25 minutes at 75°C.

15) Expose MA6

-Channel 2, 20um gap, 12 sec, hard contact.

-Develop with 319.

16) Ti etch

- Etch Ti to open holes for electroplating.

- Measure 4 Sacrificial heights for 4 MEMS to keep track of electroplating thickness.

17) Electroplate

Setup

- Set hotplate probe to 55°C.

- Set stirrer to 200RPM.

- Electroplate at 3 mA for 4 minutes to stabilize electric field.

- Bump to whatever current will work without bubbling (usually 8mA).

- Plate to 1.9um-2um.

18) Expose MA6

-Channel 2, flood exposure, 20sec.

-Develop with 319.

19) Membrane etch

- Etch Ti.

- Etch Au (Gold tends to be hard to remove from around Meanders, use good microscope to zoom in and make sure its all gone before doing ti etch).

- Etch Ti.

-Check electrode under microscope.

20) Strip sacrificial

- Out the wafer in 1112A overnight at 50°C

-Turn off the heat in the morning.

-Leave in stripper till later in the day or the next morning.

21) Super critical dryer

-Dry MEMS

REFERENCES

[1] G. Wang, "RF MEMS Switches with Novel Materials and Micromachining Techniques for SOC/SOP RF Front Ends," Ph.D. Thesis, Georgia Institute of Technology, 2006.

[2] Y. Liu, "MEMS and BST Technologies for Microwave Applications," Ph.D. Thesis, University of California, Santa Barbara, 2002.

[3] G. Rebeiz, and J. Muldavin, "RF MEMS Switches and Switch Circuits," *IEEE Microwave Magzine,* vol. 12, pp. 59-71, 2001.

[4] Z. J. Yao, S. Chen, S. Eshelman, D. Denniston, and C. L. Goldsmith, "Micromachined low-loss microwave switches," *IEEE Journal of Microelectromechanical Systems,* vol. 8, pp. 129-134, 1999.

[5] G. Wang, D. Thompson, J. Papapolymerou, and E. M. Tentzeris, "Low Cost RF MEMS Switch Using LCP Substrate," *Proc. IEEE European Microwave Conference,* pp. 1441-1444, 2004.

[6] J. B. Muldavin, R. Boisvert, C. Bozler, S. Rabe, and C. Keast, "Power handling and linearity of MEMS capacitive series switches," *Proc. IEEE International Microwave Symposium,* pp. 1915-1918, 2003.

[7] (Accessed in September 2010). *Microwave Encyclopedia*. Available: http://www.microwaves101.com/encyclopedia/MEMS2.cfm

[8] C. L. Goldsmith, D. J. Foreland, Z. Peng, J. C. M. Hwang, and J. L. Ebel, "High-cycle life testing of RF MEMS switches," *Proc. IEEE International Microwave Symposium,* pp. 1805-1808, 2007.

[9] C. L. Goldsmith, J. Maciel, and J. McKillop, "Demonstrating Reliability," *IEEE Microwave Magazine,* vol. 8, pp. 56-60, 2007.

[10] J. Maciel, J. Lampen, and S. Majumder, "High-reliability MEMS Switches for Wireless Applications," *Advanced Microelectronics,* vol. 37, pp. 20-23, 2010.

[11] X. Yuan, "Charging and Modeling of Dielectric Charging Effects in RF MEMS Capacitive Switches," Ph.D. Thesis, Lehigh University, 2006.

[12] D. Hyman, and M. Mehregany, "Contact physics of gold micro-contact considerations," *IEEE Transactions on Components and Packaging Technologies,* vol. 22, pp. 357-364 1999.

[13] C. L. Goldsmith, D. Forehand, D. Scarbrough, Z. Peng, C. Palego, J. C. M. Hwang, and J. Clevenger, "Understanding and improving longevity in RF MEMS

capacitive switches," *Proc. International Society of Optical Engineering,* vol. 6884, 2008.

[14] K. D. Leedy, R. E. Strawser, R. Cortez, and J. L. Ebel, "Thin-Film encapsulated RF MEMS Switches," *Journal of Microelectromechanical Systems,* vol. 16, pp. 304-309, 2007.

[15] G. Rebeiz, K. Entesari, I. Reines, S. Park, M. El-tanani, A. Grichener, and A. Brown, "Tuning in to RF MEMS," *IEEE Microwave Magazine,* vol. 10, pp. 55-72, 2009.

[16] D. I. Forehand, and C. L. Goldsmith, "Wafer-level Micro-encapsulation," *Proc. Gov't Microcircuit Applications and Critical Tech Conference,* pp. 320-323, 2005.

[17] R. Tummala, and M. Swaminathan, *Introduction to System-on-Package (SOP)*: McGraw-Hill Professional, 2008.

[18] J. J. Maciel, J. F. Slocum, J. K. Smith, and J. Turtle, "MEMS Electronically steerable antennas for fire control radars," *Proc. IEEE Radar Conference,* pp. 677-682, 2007.

[19] J. Brank, J. Yao, M. Eberly, A. Malczewski, K. Varian, and C. L. Goldsmith, "RF MEMS-based tunable filters," *International Journal of RF and Microwave Computer- Aided Engineering,* vol. 11, pp. 276-284, 2001.

[20] C. D. Nordquist, A. Muyshondt, M. V. Pack, P. S. Finnegan, C. W. Dyck, I. C. Reines, G. M. Kraus, T. A. Plut, G. R. Solan, C. L. Goldsmith, and C. T. Sullivan, "An X-band to Ku-band RF MEMS switched coplanar strip filter," *IEEE Microwave and Wireless Components Letters,* vol. 14, pp. 425-427, 2004.

[21] D. Koester, K. Markus, and M. Walters, "MEMS: small machines for the microelectronics age," *IEEE Computer,* vol. 29, pp. 93-94, 1996.

[22] S. B. Brown, and E. Jansen, "Reliability and long term stability of MEMS," *Advanced Applications of Lasers in Materials Processing,* pp. 9-10, 1996.

[23] K. Markus, "Developing infrastructure to mass-produce MEMS," *IEEE Computational Science and Engineering,* vol. 4, pp. 49-54, 1997.

[24] (Accessed in September 2010). *Coventorware*. Available: http://www.coventor.com/coventorware.html

[25] (Accessed in September 2010). *IntelliSuite*. Available: http://www.intellisensesoftware.com/intellisuite/Isuite-Overview.html

[26] (Accessed in September 2010). *COMSOL*. Available: http://www.comsol.com/products/mems/

[27] E. Brown, "RF MEMS for digitally-controlled front-end components," *Proc. IEEE International Conference on Innovative Systems in Silicon,* p. 338, 1997.

[28] H. S. Newman, J. L. Ebel, D. Judy, and J. Maciel, "Lifetime Measurements on a High-Reliability RF-MEMS Contact Switch," *IEEE Microwave and Wireless Components Letters,* vol. 18, pp. 100-102, 2008.

[29] E. P. Popov, *Mechanics of Materials*. New Jersey: Prentice-Hall Inc., 1976.

[30] N. S. Barker, "Distributed MEMS transmission lines," PhD Thesis, University of Michigan, Ann Arbor, 1999.

[31] R. J. Roark, and W.C. Young, *Formulas for Stress and Strain*. NewYork, NY: McGraw Hill, 1989.

[32] G. Wang, S. B. G., A. Jeyakumar, J. Papapolymerou, and C. Henderson, "Low cost RF MEMS switches using photodefinable mixed oxide dielectrics," *Proc. IEEE International Microwave Symposium,* pp. 1633-1636, 2003.

[33] H. Gere, *Mechanics of Materials*: Thompson-Engineering, 2003.

[34] N. Kingsley, G. Wang, and J. Papapolymerou, "Comparative Study of Analytical and Simulated Doubly-Supported RF MEMS Switches for Mechanical and Electrical Performance," *The Applied Computation Electromagneics Society Journal,* vol. 21, pp. 9-15, 2006.

[35] S. Senturia, *Microsystem Design*: Kluwer Academic Publisher, 2001.

[36] J. B. Muldavin, and G. Rebeiz, "Nonlinear electro-mechanical modeling of MEMS switches," *Proc. IEEE International Microwave Symposium,* pp. 2119-2122, 2001.

[37] D. M. Pozar, "Microwave Engineering," ed. NewYork, NY: Wiley, 1998.

[38] J. Wibbeler, G. Pfeifer, and M. Hietschold, "Parasitic charging of dielectric surfaces in capacitive microelectromechanical systems (MEMS)," *Sensors and Actuators A,* vol. 71, pp. 74-80, 1998.

[39] X. Yuan, S. Cherepko, J. Hwang, C. L. Goldsmith, C. Nordquist, and C. Dyck, "Initial observation and analysis of dielectric-charging effects on RF MEMS capacitive switches," *Proc. IEEE International Microwave Symposium,* pp. 1943-1946, 2004.

[40] D. T. Krick, P. M. Lenahan, and J. Kanicki, "Electrically active point defects in amorphous silicon nitride: An illumination and charge injection study," *Journal of Applied Physics,* vol. 64, pp. 3558-3563, 1998.

[41] G. M. Rebeiz, *RF MEMS Theory, Design and Technology*. New Jersey, NY: J. Wiley and Sons, 2003.

[42] J. DeNatale, R. Mihailovich, and J.Waldrop, "Techniques for reliability analysis of RF MEMS switch," *Proc. IEEE International Reliability Physics Symposium,* pp. 116-117, 2002.

[43] W. M. van Spengen, R. Puers, R. Mertens, and I. D. Wolf, "Experimental characterization of stiction due to charging in RF MEMS," *IEEE International Electron Devices Meeting Digest,* pp. 901-904, 2002.

[44] W. M. van Spengen, R. Puers, R. Mertens, and I. d. Wolf, "A comprehensive model to predict the charging and reliability of capacitive RF MEMS switches," *Journal of Micromechanics and Microengineering,* vol. 14, pp. 514-521, 2004.

[45] J. R. Reid, and R. T.Webster, "Measurements of charging in capacitive microelectromechanical switches," *Electron. Letters,* vol. 38, pp. 1544-1545, 2002.

[46] S. Melle, F. Flourens, D. Dubuc, K. Grenier, P. Pons, F. Pressecq, J. Kuchenbecker, J. L. Muraro, L. Bary, and R. Plana, "Reliability overview of RF MEMS devices and circuits," *Proc. IEEE European Microwave Conference,* pp. 37-40, 2003.

[47] T. Lisec, C. Huth, and B. Wagner, "Dielectric material impact on capacitive RF MEMS reliability," *Proc. European Gallium Arsenide and Other Compound Semiconductor Applies Symposium,* pp. 471-474, 2004.

[48] R. W. Herfst, H. G. A. Huizing, P. G. Steeneken, and J. Schrnitz, "Characterization of dielectric charging in RF MEMS capacitive switches," *Proc. IEEE International Microelectronics Test Structures Conference,* pp. 133-136, 2006.

[49] J. F. Kcko, J. C. Petrosky, J. R. Reid, and K. Yung, "Non-charge related mechanism affecting capacitive MEMS switch lifetime," *IEEE Microwave Wireless Component Letters,* vol. 16, pp. 140-142, 2006.

[50] S. Patton, and J. Zabinski, "Effects of dielectric charging on fundamental forces and reliability in capacitive microelectromechanical systems radio frequency switch contacts," *Journal of Applied Physics,* vol. 99, pp. 1700-1710, 2006.

[51] C. L. Goldsmith, J. Ehmke, A. Malczewski, B. Pillans, S. Eshelman, Z. Yao, J. Brank, and M. Eberly, "Lifetime characterization of capacitive RF MEMS switches," *Proc. IEEE International Microwave Symposium,* pp. 227-230, 2001.

[52] Z. Peng, X. Yuan, J. C. M. Hwang, D. Forehand, and C. L. Goldsmith, "Dielectric charging of RF MEMS capacitive switches under bipolar control-voltage

waveforms," *Proc. IEEE International Microwave Symposium,* pp. 1817-1820, 2007.

[53] P. Czarnecki, X. Rottenberg, R. Puers, and I. D. Wolf, "Impact of biasing scheme and environment conditions on the lifetime of RF-MEMS capacitive switches," *Proc. MEMSWAVE,* pp. 133-136, 2005.

[54] X. Rottenberg, B. Nauwelaers, W. De Raedt, and H. A. C. Tilmans, "Distributed dielectric charging and its impact on RF MEMS devices," *Proc. GAAS Symposium,* pp. 475-478, 2004.

[55] R. Botsco, and R. McMaster, *Nondestructive Testing Handbook* vol. 4: ASNT, 1986.

[56] A. V. Hippel, *Dielectric Materials and Applications*: John Wiley & Sons, 1954.

[57] P. Harrop, *Dielectrics*: John Wiley & Sons, 1972.

[58] C. J. F. Böttcher, *Theory of electric polarization*. Amsterdam: Elsevier, 1952.

[59] K. C. Kao, *Dielectric Phenomena in Solids, With Emphasis on Physical Concepts of Electronic Processes*. Amsterdam: Elsevier, 2004.

[60] (Accessed in September 2010). *Electronic Materials*. Available: http://www.tf.uni-kiel.de/matwis/amat/elmat_en/index.html

[61] (Accessed in September 2010). *Wikipedia*. Available: http://en.wikipedia.org/wiki/Permittivity

[62] G. Papaioannou, "AMICOM Summer School," 2007.

[63] G. Papaioannou, "RF MEMS Reliability Workshop," 2009.

[64] Z. Peng, X. Yuan, J. C. M. Hwang, D. Forehand, and C. L. Goldsmith, "Top versus bottom charging of dielectric in RF MEMS capacitive switches," *Proc IEEE Asian Pacific Microwave Conference,* pp. 1535-1539, 2006.

[65] Z. Peng, D. Molinero, C. Palego, J. Hwang, C. Moody, A. Malczewski, and B. W. Pillans, "Effect of Surface Conduction on Dielectric Charging in RF MEMS Capacitive Switches," *Proc. IEEE International Microwave Symposium,* pp. 1250-1253 2010.

[66] Z. Peng, C. Palego, J. C. M. Hwang, D. I. Forehand, C. L. Goldsmith, C. Moody, A. Malczewski, B. W. Pillans, R. Daigler, and J. Papapolymerou, "Impact of humidity on dielectric charging in RF MEMS capacitive switches," *IEEE Microwave Wireless Components Letters,* vol. 19, pp. 299-30, 2009.

[67] (Accessed in September 2010). *Accuratus* Available: www.accuratus.com.

[68] M. N. Jones, Y. W. Kwon, and D. P. Norton, "Dielectric constant and current transport for HfO2 thin films on ITO," *Applied. Physics A,* vol. 81, pp. 285-288, 2005.

[69] X. Song, R. Fu, and H. He, "Frequency effects on the dielectric properties of AlN films deposited by radio frequency reactive magnetron sputtering," *Microelectronic Engineering,* vol. 86, pp. 2217-2221, 2009.

[70] K. Yoshida, I. Umezu, N. Sakamoto, M. Inada, and A. Sugimura, "Effect of structure on radiative recombination processes in amorphous silicon suboxide prepared by RF sputtering," *Journal of Applied Physics,* vol. 92, p. 5936, 2002.

[71] S. Bécu, S. Crémer, and J. L. Autran, "Capacitance non-linearity study in Al_2O_3 MIM capacitors using an ionic polarization model," *Microelectronic Engineering,* vol. 83, pp. 2422-2426, 2006.

[72] K. Karch, and F. Bechstedt, "Ab initio lattice dynamics of BN and AlN: Covalent versus ionic forces," *Phys. Rev. B,* vol. 56, pp. 7404-7415, 1997.

[73] C. R. Li, L. J. Ding, J. Z. Lv, Y. P. Tu, and Y. C. Cheng, "The relation of trap distribution of alumina with surface flashover performance in vacuum," *IEEE Transactions on Dielectrics and Electrical Insulation,* vol. 13, pp. 79-84, 2006.

[74] G. Papaioannou, and T. Lisec, "Dielectric charging process in AlN RF-MEMS capacitive switches," *Proc. IEEE European Microwave Conference,* pp. 540-543, 2007.

[75] E. Papandreou, G. Papaioannou, and T. Lisec, "A correlation of capacitive RF-M.EMS reliability to AlN dielectric film spontaneous polarization," *International Journal of Microwave and Wireless Technologies,* pp. 43-47, 2009.

[76] B. R. Sahu, and L. Kleinman, "Theoretical study of structural and electronic properties of β-Ta_2O_5 and δ-Ta_2O_5," *Physical Review B,* vol. 69, p. 165202.

[77] A. Toriumi, K. Tomida, H. Shimizu, K. Kita, and K. Kyono, "Far and Mid Infrared absorption study of $HfO_2/SiO_2/Si$ system," *Proc. Electrochemical Society,* pp. 471-481, 2005.

[78] P. Czarnecki, X. Rottenberg, P. Soussan, P. Ekkels, P. Muller, P. Nolmans, W. De Raedt, H.A.C. Tilmans, R. Puers, L. Marchand, and I. D. Wolf, "Influence of the substrate on the lifetime of capacitive RF MEMS switches," *Proc International Conference on Micro Electro Mechanical Systems,* pp. 172-175, 2008.

[79] E. Papandreou, M. Lamhamdi, C. Skoulikidou, P.Pons, G. Papaioannou, and R. Plana, "Structure dependent charging process in RF MEMS capacitive switches," *Microelectronics Reliability,* vol. 47, pp. 1822-1827, 2007.

[80] G. Papaioannou, E. Papandreou, J. Papapolymerou, and R. Daigler, "Dielectric Discharging processes in RF-MEMS Capacitive Switches," *Proc. IEEE Asian Pacific Microwave Conference,* pp. 437-440, 2007.

[81] X. Yuan, J. C. M. Hwang, D. Forehand, and C. L. Goldsmith, "Modeling and characterization of dielectric-charging effects in RF MEMS capacitive switches," *Proc. IEEE International Microwave Symposium,* pp. 753-756, 2005.

[82] S. Melle, D. De Conto, L. Mazenq, D. Dubuc, B. Poussard, C. Bordas, K. Grenier, L. Bary, O. Vendier, J. L. Muraro, J. L. Cazaux, and R. Plana, "Failure predictive model of capacitive RF-MEMS," *Microelectronics Reliability,* vol. 45, pp. 1770-1775, 2005.

[83] M. Lamhamdi, P. Pons, U. Zaghloul, L. Boudou, F. Coccetti, J. Guastavino, Y. Segui, G. Papaioannou, and R. Plana, "Voltage and temperature effect on dielectric charging for RF-MEMS capacitive switches reliability investigation," *Microelectronics Reliability,* vol. 48, pp. 1248-1252, 2008.

[84] X. Yuan, Z. Peng, J. C. M. Hwang, D. Forehand, and C. L. Goldsmith, "Temperature acceleration of dielectric charging in RF MEMS capacitive switches," *Proc. IEEE International Microwave Symposium,* pp. 47-50, 2006.

[85] M. Lamhamdi, J. Guastavino, L. Boudou, Y. Segui, P. Pons, L. Bouscayrol, and R. Plana, "Charging effects in RF capacitive switches influence of insulating layers composition," *Microelectronics Reliability,* vol. 46, pp. 1700-1704, 2006.

[86] G. J. Papaioannou, M. Exarchos, V. Theonas, G. Wang, and J. Papapolymerou, "Temperature study of the dielectric polarization effects of capacitive RF MEMS switches," *IEEE Transactions on Microwave Theory and Techniques,* vol. 53, pp. 3467-3473, 2005.

[87] G. J. Papaioannou, M. Exarchos, V. Theonas, J. Psychias, G. Konstantinidis, D. Vasilache, A. Muller, and D. Neculoiu, "Effect of space charge polarization in radio frequency microelectromechanical system capacitive switch dielectric charging," *Applied Physics Letters,* vol. 89, pp. 103512-103514, 2006.

[88] G. Papaioannou, J. Papapolymerou, P. Pons, and R. Plana, "Dielectric charging in radio frequency microelectromechanical system capacitive switches: A study of material properties and device performance," *Applied Physics Letters,* vol. 90, pp. 233507-233509, 2007.

[89] R. Daigler, G. Papaioannou, E. Papandreou, and J. Papapolymerou, "Effect of Dielectric Film Thickness on Dielectric Charging of RF MEMS Capacitive Switches," *Proc. IEEE International Microwave Symposium,* pp. 1275-1278, 2008.

[90] P. Czarnecki, X. Rottenberg, R. Puers, and I. D. Wolf, "Effect of gas pressure on the lifetime of capacitive RF MEMS switches," *Proc. International Conference on Micro Electro Mechanical Systems,* pp. 890-893, 2006.

[91] G. J. Papaioannou, G. Wang, D. Bessas, and J. Papapolymerou, "On the polarization mechanisms of RF MEMS capacitive switches," *Proc. IEEE European Microwave Integrated Circuits Conference,* pp. 513-516, 2006.

[92] S. Melle, D. De Conto, D. Dubuc, K. Grenier, O. Vendier, J. L. Muraro, J. L. Cazaux, and R. Plana, "Reliability modeling of capacitive RF MEMS," *IEEE Transactions on Microwave Theory and Techniques,* vol. 53, pp. 3482-3488, 2005.

[93] D. Molinero, R. Comulada, and L. Castañer, "Dielectric charge measurements in capacitive microelectromechanical switches," *Journal of Applied Physics,* vol. 89, pp. 901-903, 2006.

[94] X. Yuan, Z. Peng, J. C. M. Hwang, D. Forehand, and C. L. Goldsmith, "A transient SPICE model for dielectric-charging effects in RF MEMS capacitive switches," *IEEE Transactions on Electron Devices,* vol. 53, pp. 2640-2648, 2006.

[95] M. Exarchos, E. Papandreou, P. Pons, M. Lamhamdi, G. Papaioannou, and R. Plana, "Charging of radiation induced defects in RF MEMS dielectric films," *Microelectronics Reliability,* vol. 46, pp. 1695-1699, 2006.

[96] R. Ramprasad, "Phenomenological theory to model leakage currents in metal-insulator-metal capacitor systems," *Physica Status Solidi (b),* vol. 239, pp. 59-70, 2003.

[97] G. Papaioannou, N. Tavassolian, M. Koutsoureli, E. Papandreou, and J. Papapolymerou, "Investigation of Charging Mechanisms in RF-MEMS Capacitive Switches with Silicon Nitride: The Effect of Material Stoichiometry," *Proc. IEEE International Microwave Symposium,* pp. 1653-1656, 2009.

[98] N. Tavassolian, M. Koutsoureli, E. Papandreou, G. Papaioannou, B. Lacroix, Z. Liu, and J. Papapolymerou, "The Effect of Silicon Nitride Stoichiometry on Charging Mechanisms in RF-MEMS Capacitive Switches," *IEEE Transactions on Microwave Theory and Techniques,* pp. 3518-3524, 2009.

[99] G. Papaioannou, and J. Papapolymerou, "Dielectric charging mechanisms in RF-MEMS Capacitive switches," *Proc. IEEE European Microwave Integrated Circuits Conference,* pp. 540-543, 2007.

[100] A. Zerga, M. Carrada, M. Amann, and A. Slaoui, "Si-nanostructures formation in amorphous silicon nitride SiN_x:H deposited by remote PECVD," *Physica E,* vol. 38, pp. 21-26, 2007.

[101] M. Carrada, A. Zerga, M. Amann, J. J. Grob, J. P. Stoquert, A. Slaoui, C. Bonafos, and S. Scham, "Structural and optical properties of high density Si-ncs synthesized in SiNx:H by remote PECVD and annealing," *Materials Science and Engineering B.,* vol. 147, pp. 218-221, 2008.

[102] M. Martyniuk, J. Antoszewski, C. A. Musca, J. M. Dell, and L. Faraone, "Environmental stability and cryogenic thermal cycling of low-temperature plasma-deposited silicon nitride thin films," *Journal of Applied Physics,* vol. 99, pp. 053519-053528, 2006.

[103] J. Vandershueren, and J. Casiot, *Topics in Applied Physics: Thermally stimulated Relaxation in Solids*. Berlin, NY: Springer-Verlag, 1979.

[104] R. Daigler, E. Papandreou, N. Tavassolian, M. Koutsoureli, G. Papaioannou, and J. Papapolymerou, "Dependence of dielectric charging on film thickness and deposition conditions," *Proc. IEEE Asian and Pacific Microwave Conference,* pp. 1-4, 2008.

[105] S.P. Lau, and J. M. Shannon, "Generation and annealing kinetics of current induced metastable defects in amorphous silicon alloys," *Journal of Non-Crystalline Solids,* vol. 266- 269, pp. 432-436, 2000.

[106] J. Bisquert, and G. Garcia-Belmonte, "Analysis of the power-law response in the fractal dielectric model by thermally stimulated currents and frequency spectroscopy," *Journal of Applied Physics,* vol. 89, pp. 5657-5662, 2001.

[107] S. P. Lau, J. M. Shannon, and B. J. Sealy, "Changes in the Poole-Frenkel coefficient with current induced defect band conductivity of hydrogenated amorphous silicon nitride," *Journal of Non-Crystalline Solids,* vol. 227-230, pp. 533-537, 1998.

[108] J. M. Shannon, and B. A. Morgan, "Hole transport via dangling-bond states in amorphous hydrogenated silicon nitride," *Journal of Applied Physics,* vol. 86, pp. 1548-1550, 1999.

[109] M. Shannon, S. C. Deane, B. McGarvey, and J. N. Sandoe, "Current induced drift mechanism in amorphous SiNx:H thin film diodes," *Applied Physics Letters,* vol. 65, pp. 2978-2980, 1994.

[110] R. Daigler, G. Papaioannou, E. Papandreou, and J. Papapolymerou, "Dielectric charging in low temperature silicon nitride for RF-MEMS capacitive switches," *Proc. Materials Research Society Symposium J: Passive and Electromechanical Materials and Integration,* 2008.

[111] U. Z. Heiba, G. Papaioannou, A. Belarni, H. Wang, F. Coccetti, P. Pons, and R. Plana, "Effect of Humidity on Dielectric Charging Process in Capacitive RF MEMS Switches Based on Kelvin Force Microscopy Surface Potential

Measurements," *Proc. Materials Research Society Meeting DD: Microelectromechanical Systems--Materials and Devices III,* 2009.

[112] R. Daigler, E. Papandreou, M. Koutsoureli, G. Papaioannou, and J. Papapolymeroua, "Effect of deposition conditions on charging processes in SiNx: application to RF-MEMS capacitive switches," *Microelectronic Engineering,* vol. 86, pp. 404-407, 2009.

[113] M. H. W. M. v. Delden, and P. J. v. d. Wel, "Reliability and electric properties for PECVD a-SiNx:H films with an optical band-gap ranging from 2.5 to 5.38 eV," *Proc. IEEE Reliability Physics Symposium,* pp. 293-297, 2003.

[114] M. Petersen, and Y. Roizin, "Density functional theory study of deep traps in silicon nitride memories," *Applied Physics Letters* vol. 89, p. 053511, 2006.

[115] A. V. Vishnyakov, Y. N. Novikov, V. A. Gritsenko, and K. A. Nasyrov, "The charge transport mechanism in silicon nitride: Multi-phonon trap ionization," *Solid-State Electronics,* vol. 53, pp. 251-255, 2009.

[116] Z. H. Cen, T. P. Chen, L. Ding, Y. Liu, J. I. Wong, M. Yang, Z. Liu, W. P. Goh, Z. H. F. R. Zhu, and S. Fung, "Evolution of electroluminescence from multiple Si-implanted silicon nitride films with thermal annealing," *Journal of Applied Physics,* vol. 105, p. 12301, 2009.

[117] N. D. Young, "The formation and annealing of hot-carrier-induced degradation in poly-Si TFT's, MOSFET's, and SOI devices, and similarities to state-creation in αSi:H," *IEEE Transactions on Electron Devices,* vol. 43, pp. 450-456, 1996.

[118] A. Acovic, G. La Rosa, and Y. Sun, "A review of hot-carrier degradation mechanisms in MOSFETs," *Microelectronics Reliability,* vol. 36, pp. 845-869, 1996.

[119] X. Rottenberg, I. De Wolf, B. K. J. C. Nauwelaers, W. D. Raedt, and H. A. C. Tilmans, "Analytical Model of the DC Actuation of Electrostatic MEMS Devices With Distributed Dielectric Charging and Nonplanar Electrodes," *Journal of Microelectromechanical Systems,* vol. 16, pp. 1243-1253, 2007.

[120] C. L. Goldsmith, and D. I. Forehand, "Temperature Variation of Actuation Voltage in Capacitive MEMS Switches," *IEEE Microwave and Wireless Components Letters,* vol. 15, pp. 718-720, 2005.

[121] (Accessed in September 2010). *MEMtronics*. Available: http://www.memtronics.com/

[122] G. Papaioannou, N. Tavassolian, C. L. Goldsmith, and J. Papapolymerou, "Dielectric charging and thermally activated processes in MEMS capacitive switches," *Proc. IEEE European Microwave Conference,* pp. 1752-1755, 2009.

[123] U. Zaghloul, G. Papaioannou, F. Coccetti, P. Pons, and R. Plana, "Dielectric charging in silicon nitride films for MEMS capacitive switches: Effect of film thickness and deposition conditions," *Microelectronics Reliability,* vol. 49, pp. 1309-1314, 2009.

[124] U. Zaghloul, F. Coccetti, G. J. Papaioannou, P. Pons, and R. Plana, "A Novel Low Cost Failure Analysis Technique for Dielectric Charging Phenomenon in Electrostatically Actuated MEMS Devices," *International Reliability Physics Symposium (IRPS),* pp. 237-245, 2010.

[125] H. Kato, N. Kashio, and Y. Ohkib, "Band-tail photoluminescence in hydrogenated amorphous silicon oxynitride and silicon nitride films," *Journal of Applied Physics,* vol. 92, pp. 239-244, 2003.

[126] D. Mardivirin, A. Pothier, J. C. Orlianges, A. Crunteanu, and P. Blondy, "Charging Acceleration in Dielectric Less RF MEMS Switched Varactors under CW Microwave Power," *Proc. IEEE International Microwave Symposium,* pp. 1649-1652, 2009.

[127] C. Goldsmith, A. Sumant, O. Auciello, J. Carlisle, H. Zeng, J.C.M. Hwang, C. Palego, W. Wang, R. Carpick, V.P. Adiga, A. Datta, C. Gudeman, S. O'Brien, and S. Sampath, "Charging Characteristics of Ultra-Nano-Crystalline Diamond in RF MEMS Capacitive Switches," *Proc. IEEE International Microwave Symposium,* pp. 1246-1249, 2010.

VITA

Negar Tavassolian received the B.S. degree in Electrical Engineering from Sharif University of Technology, Tehran, Iran in 2003, and the M.S. degree in Electrical and Computer Engineering from McGill University, Montréal, Canada in 2006. Her Master's Thesis was on the simulation-based assessments of detection capabilities of a broadband antenna-sensor for cancer detection. From Aug. 2006 to July 2007, she was with the ATHENA research group at the Georgia Institute of Technology, working on ultra wideband (UWB) antennas for biomedical applications. She has been working in the MiRCTech research group since July 2007, focusing on dielectric charging effects in capacitive RF MEMS switches for her Ph.D. dissertation. She is receiving the M.S. degree in Industrial and Systems Engineering from the Georgia Institute of Technology.